

**INJECTION-LOCK AND RECONFIGURABLE
CHARGE-DOMAIN SAMPLING MIXERS/FILTERS FOR
DATA COMMUNICATIONS OVER WIRELESS CHANNELS**

by

Yushi Zhou

Bachelor of Engineering, University of Electronic Science and Technology of China, 2000

A dissertation

presented to Ryerson University

in partial fulfillment of the

requirements for the degree of

Doctor of Philosophy

in the Program of

Electrical and Computer Engineering

Toronto, Ontario, Canada, 2015

©Yushi Zhou 2015

AUTHOR'S DECLARATION FOR ELECTRONIC SUBMISSION OF A DISSERTATION

I hereby declare that I am the sole author of this dissertation. This is a true copy of the dissertation, including any required final revisions, as accepted by my examiners.

I authorize Ryerson University to lend this dissertation to other institutions or individuals for the purpose of scholarly research.

I further authorize Ryerson University to reproduce this dissertation by photocopying or by other means, in total or in part, at the request of other institutions or individuals for the purpose of scholarly research.

I understand that my dissertation may be made electronically available to the public.

ABSTRACT

Yushi Zhou

Injection-Lock and Reconfigurable Charge-Domain Sampling Mixers/Filters for Data Communications Over Wireless Channels

Doctor of Philosophy, Electrical and Computer Engineering, Ryerson University, 2015

This thesis provides a theoretical and experimental study of injection locking and reconfigurable charge-domain sampling mixers and filters for data communications over wireless channels.

On injection-locking, the intrinsic relation between the characteristics of injection signals such as sinusoidal or square, single-tone or multi-tone, the type of oscillators under injection such as harmonic oscillators (passive or active LC oscillators) or non-harmonic oscillators (ring or relaxation oscillators), and the lock range of the oscillators under injection was investigated. For the very first time, we discovered the intrinsic relation between the lock range and the phase of multiple injections of harmonic oscillators. In addition, we obtained the closed-form expression of the lock range of harmonic oscillators with square-wave injections. Moreover, we obtained the distinct characteristics of the lock range of harmonic and non-harmonic oscillators and that of different types of non-harmonic oscillators. These theoretical findings were not known before and were validated using simulation results.

On reconfigurable charge-domain sampling mixers and filters for software-defined radio, a novel quadrature charge-domain down-conversion sampling mixer with embedded finite-impulse-response (FIR), infinite-impulse-response (IIR), and 4-path bandpass filters was developed. An in-depth investigation of the principles of periodic impulse sampling, periodic windowed sampling, and periodic N-path windowed sampling was presented and a detailed mathematical treatment of charge-domain windowed samplers with built-in sinc, FIR and IIR filters was provided. The proposed quadrature charge-domain sampler with embedded FIR, IIR, and 4-path band-pass filters was implemented in IBM 130 nm 1.2V CMOS

technology and its performance was validated both using simulation results and on-wafer measurement.

ACKNOWLEDGMENTS

First and foremost, I would like to express my most sincere gratitude to my advisor, Professor Fei Yuan, for his kind guidance, helpful discussions and constructive suggestions throughout my study. I could not have completed this work without his support and enthusiasm.

I also thank the other committee members, Professor Andy Ye, Professor Vadim Geurkov, Professor GuangJun Liu and Professor Wai Tung Ng from University of Toronto for their invaluable feedback.

I wish to thank my fellow students in the Integrated Circuits and Systems Research Group, who were sitting around me and made the long journey of the study enjoyable. Special acknowledgements go to Young Jun Park, Alaa AL-Tae, Guangyu Zhu, Shaul Peker, Xiongliang Lai for their helpful discussions and suggestions for my research and career. I also would like to take the opportunity to thank the former members, Dr. Adrian Tang and Dr. Dominic DiClemente for their effort in establishing the test facilities, and Tarek Khan for creating the Cadence simulation environments. I am also indebted to staffs Jason Naughton, Dan Giannitelli and Bruce Derwin for their timely technical support.

Thanks to the Canadian Microelectronics Corporation (CMC) for making the fabrication of my chips. Also, I am grateful to the Natural Sciences and Engineering Research Council of Canada (NSERC), a significant funding source supporting my study (Canada Graduate Scholarships-CGS2) during 2013-2015.

Most importantly, I must thank my parents, brothers for providing me with much needed support and guidance over the years. Very special thanks to my wife, Zhaoying for her love and understanding throughout this endeavour. Finally, I wish to offer my gratitude to my lovely son, Alex, bringing joyfulness to me.

Table of Contents

Table of Contents	vi
List of Tables	ix
List of Figures	x
List of Symbols	xv
1 INTRODUCTION	1
1.1 Background	1
1.2 Motivation and Objectives for Injection-Locked Oscillators	7
1.2.1 Injection-Locked Active Inductor Oscillators	7
1.2.2 Injection-Locked Non-Harmonic Oscillators	8
1.3 Motivation and Objectives for Charge-Domain Sampling Circuits with Tunable Band-Pass Filter	10
1.4 Contributions	12
1.4.1 Injection-Locked Oscillators	12
1.4.2 Tunable Band-Pass Filter Embedded Charge-Domain Sampling Circuits	12
1.5 Thesis Organization	13
2 Injection-Locked Active Inductor Oscillators	15
2.1 Injection-Locked Oscillators	15
2.2 Active Inductor Oscillators	18

2.3	Lock Range of Generic LC Oscillators	20
2.4	Lock Range and Tank Impedance Variation	24
2.5	Comparison of Injection-Locked LC Oscillators and Active Inductor Oscillators	27
2.6	Summary	32
3	Multiple Multi-Tone Injection-Locked Oscillators	34
3.1	Representation of Non-Harmonic Oscillators	34
3.2	Representation of Injection-Locked Non-harmonic Oscillators	36
3.2.1	Single-Tone Injection	36
3.2.2	Multi-Tone Injection	37
3.3	Harmonic Oscillators with Multiple Injections	39
3.4	Non-Harmonic Oscillators with Multiple Injections	41
3.5	Lock Range of Non-Harmonic Oscillators with Multiple Single-Tone Injections	42
3.6	Simulations	48
3.7	Lock Range of Non-Harmonic Oscillators with Multiple Multi-Tone Injections	49
3.8	Simulations	58
3.9	Summary	62
4	A Quadrature Charge-Domain Sampling Mixer with Embedded FIR, IIR, and N-Path Filters	64
4.1	N-path Filters	65
4.1.1	Periodic Impulse Sampling	65
4.1.2	Periodic Windowed Sampling	66
4.1.3	Periodic N-Path Windowed Sampling	68
4.2	Charge-Domain Windowed Sampling	73
4.2.1	Sinc Low-Pass Filter	73

4.2.2	FIR Filter	78
4.2.3	IIR Filter	82
4.3	Circuit Design and Analysis	86
4.3.1	Performance	88
4.3.2	Noise	90
4.3.3	Effect of Nonidealities	94
4.4	Measurement Results	97
4.5	Summary	104
5	A Cascaded Charge-domain Sampling Mixer with Embedded sinc^3 FIR and N-Path Filters	106
5.1	Hight-Order FIR Filter	106
5.2	Circuit Design and Analysis	108
5.2.1	Performance	109
5.3	Simulation Results	111
5.4	Summary	112
6	Conclusions and Future Work	115
6.1	Conclusions	115
6.2	Future Work	116
	Bibliography	118

List of Tables

3.1	Lock Range Coefficient α_d	47
4.1	Noise Bandwidth of Sampling Mixer with 4-path Bandpass, sinc, FIR, and IIR Filters Considered Individually.	93
4.2	Performance Summary of Sampling Mixer	105
5.1	Performance Comparison	114

List of Figures

1.1	Three receiver architectures: (a) Super-heterodyne receiver, (b) Zero-IF receiver, and (c) SDR receiver.	5
1.2	Spectrum allocation for wireless communications.	7
2.1	A feedback system.	15
2.2	Injection locked procedure represented in simplified spectrum diagram. (a) Unlocked, (b) Fast beat, and (c) Locked.	17
2.3	Single-ended active inductor.	19
2.4	Examples of active inductors. (a) Wu current reuse active inductor , (b) Lin active inductor , and (c) Hara active inductor	20
2.5	(a) Injection-locked oscillators. (b) Block diagram of injection-locked oscillators.	21
2.6	Impedance of the LC tank of injection-locked LC oscillators.	22
2.7	(a) Injection-locked oscillators. (b) Equivalent circuit of injection-locked oscillators. The dotted line represents the real injection signal, which has been merged into the variation of the LC tank.	25
2.8	Injection-locked passive LC oscillator. C_1 and C_2 are accumulation MOS varactors. Circuit parameters : $W_{1,2} = 10\mu\text{m}$; $W_3 = 15\mu\text{m}$, $W_{4,5} = 1\mu\text{m}$, $V_c = 1.2\text{ V}$, $V_b = 0.66\text{ V}$, $I_{ds3} = 1.42\text{ mA}$	27
2.9	Schematic of injection-locked active-inductor VCO with Wu active inductors. Circuits parameters : $W_{1a,1b} = 40\mu\text{m}$, $W_{2a,2b} = 18.9\mu\text{m}$, $W_{3a,3b} = 4\mu\text{m}$, $W_{4,5} = 10\mu\text{m}$, $W_6 = 15\mu\text{m}$, $W_{7,8} = 1\mu\text{m}$, $V_{b1} = 0.34\text{ V}$, $V_{b2} = 0.48\text{ V}$, $V_{b3} = 0.7\text{ V}$, $I_{ds3} = 131\mu\text{A}$, $I_{ds6} = 1.42\text{ mA}$	29
2.10	Simulated phase noise of passive LC oscillator $I_{inj}/I_o = 0.05$	31
2.11	Simulated phase noise of active-inductor LC oscillator $I_{inj}/I_o = 0.05$	31
2.12	Simulated lock range.	32

2.13	Asymmetry of the lock range of injection-locked active-inductor oscillator.	33
3.1	Waveform and spectrum of non-harmonic oscillators.	35
3.2	Representation of injection-locked non-harmonic oscillators with a single-tone injection.	37
3.3	Injection-locked harmonic oscillators with multiple injections.	40
3.4	Representation of injection-locked non-harmonic oscillators with multiple single-tone injections.	42
3.5	Schematic of relaxation oscillator with injection-locking. Circuit parameters: $W_{1,2,6,7,10,11} = 0.5\mu\text{m}$, $W_{3,4} = 1.2\mu\text{m}$, $W_{8,9,12,13} = 1.25\mu\text{m}$, $W_5 = 2\mu\text{m}$, Supply voltage $V_{DD} = 0.9\text{V}$, $V_{ref} = 0.31\text{ V}$, $I_b = 253\text{ nA}$, $V_b = 0.62\text{ V}$	48
3.6	Simulated spectrum of relaxation oscillator without injection. Top - Fundamental. Middle : 3rd harmonic. Bottom : 5th harmonic.	50
3.7	Simulated spectrum of relaxation oscillator in fast beat. Top - Fundamental. Middle : 3rd harmonic. Bottom : 5th harmonic.	51
3.8	Simulated spectrum of relaxation oscillator in quasi-lock. Top - Fundamental. Middle : 3rd harmonic. Bottom : 5th harmonic.	52
3.9	Simulated spectrum of relaxation oscillator in lock state. Top - Fundamental. Middle : 3rd harmonic. Bottom : 5th harmonic.	53
3.10	Simulated dependence of the lock range of relaxation oscillator with a sinusoidal injection and double sinusoidal injections whose phase difference is 180 degree on injection strength.	54
3.11	Representation of injection-locked non-harmonic oscillators with multiple multi-tone injections.	55
3.12	Simulated dependence of the lock range of relaxation oscillator with a single square-wave injection and with double square-wave injections whose phase difference is 180 degree on injection strength.	59
3.13	Simulated dependence of the lock range of relaxation oscillator with differential square-wave injection on injection strength.	60
3.14	Simulated dependence of the lock range of relaxation oscillator with a single sinusoidal injection, a single square-wave injection, and a single dual-tone (two-sinusoids) injection on injection strength.	60

3.15	Simulated dependence of the lock range of relaxation oscillator with double square-wave injections on the phase difference of the injection signals. The injection ratio is 0.1.	61
3.16	Simulated dependence of the lock range of relaxation oscillator with a two-tone sinusoidal injection and double two-tone injections on injection strength. . .	61
3.17	Simulated dependence of the lock range of relaxation oscillator with double single-tone injections, double two-tone injections, and double square-wave injections on injection strength.	62
4.1	Periodic impulse sampling of band-limited signals.	65
4.2	(a) Periodic impulse sampling of band-limited signals. Baseband signal at ω is replicated to sidebands at $\omega + n\omega_s$. (b) Periodic impulse sampling of broadband signals. The sideband components of input at $\omega + n\omega_s$ are aliased back to the baseband at ω	66
4.3	Periodic windowed sampling of band-limited signals.	67
4.4	(a) Periodic windowed sampling of narrow-band signals without interferences. (b) Periodic windowed sampling of band-limited signals with interferences. Interferences at $\omega + n\omega_s$ are aliased back to the desired baseband.	68
4.5	N-path filter. Sampling mixers are implemented using switches driven by a sampling clock with N non-overlapping phases. Non-overlapping uniform sampling pulse width: $\tau = T_s/N$. $\sigma_k = \sigma_{k-1} + \tau$ and $\sigma_{k-1} = nT_s + (k-1)\tau$. . .	69
4.6	Single-ended 4-path filter.	72
4.7	Single-ended 4-path filter.	73
4.8	Frequency response of single-ended 4-path filter in Fig. 4.6.	74
4.9	Charge-domain sampling. Solid line : Small T_i . Dashed line : Large T_i	74
4.10	Gain-normalized transfer function of sinc.	75
4.11	Time interleaved charge-domain sampling.	77
4.12	Charge-domain sampler with built-in FIR filter.	78
4.13	Spectrum of charge-domain windowed sampler with FIR filtering. Parameters: $f_s=10$ MHz, $N=10$ and $T_f = T_s/N$	80
4.14	Spectrum of charge-domain windowed sampler with FIR filtering. Parameters: $f_s=20$ MHz, $N=5$ and $T_f = T_s/N$	81

4.15	Spectrum of charge-domain windowed sampler with CT sinc low-pass filter. $f_i=200$ MHz, $f_s=10$ MHz, $N=10$ and $T_f = T_s/N$	81
4.16	Charge-domain sampler with a build-in FIR and IIR filter and its timing scheme.	82
4.17	Time interleaved charge-domain sampler with a build-in FIR and IIR filter and its timing scheme.	83
4.18	Spectrum of charge-domain windowed sampler with first-order IIR filter. $f_s=10$ MHz.	85
4.19	Quadrature Charge-Domain Sampler with 4-path bandpass filter. Circuit Parameters: $W_{1,2} = 20\mu\text{m}$, $W_{3,4,5} = 15\mu\text{m}$, $W_{6,7} = 10\mu\text{m}$, $L = 0.36\mu\text{m}$, $I_b = 150\mu\text{A}$, $V_{b1}=0.67$ V, $V_{b2}=0.65$ V.	86
4.20	(a) Differential 4-path band-pass filter, (b) Clocking scheme.	87
4.21	Simulated differential 4-path band-pass filter with $T_s = T_{LO} = 100$ MHz. . .	87
4.22	(a) Differential charge-domain sampler (only half of the circuit is shown), (b) Clocking scheme.	88
4.23	Simulated transfer function (normalized) of quadrature charge-domain sampler. Ideal transconductor with $g_m = 0.5$ mS and ideal switches with $R_{on} = 1\Omega$ and $R_{off} = 1\text{T}\Omega$ are used. The input is a 100 MHz sinusoid. The sampling frequency is 100 MHz with 25% duty cycle. Voltage gain provided by the sampler is 15 dB.	89
4.24	Noise analysis of proposed charge-domain sampling mixer.	90
4.25	Noise analysis of N-path filter.	92
4.26	Simulated effect of ON-resistance of switches on 4-path bandpass filter. R_{on} is varied from 5Ω to 200Ω	94
4.27	Simulated frequency response (normalized) of quadrature charge-domain sampler with embedded 4-path bandpass filter at process corners. The input frequency is 100 MHz, the output baseband sampling frequency is 25 MHz (Two 12.5 MHz interleaved clocks with 50% duty-cycle). Legends: TT (typical nMOS/typical pMOS), SS (slow nMOS/slow pMOS), FS (fast nMOS/slow pMOS), SF (slow nMOS/fast pMOS), and FF (fast nMOS/fast pMOS). . . .	95
4.28	Simulated frequency tuning range. The input frequency is varied from 50 MHz to 250 MHz. The sampling frequency is also varied accordingly such that the output frequency remains unchanged.	97

4.29	Die microphotograph of quadrature charge-domain sampler(1x2 mm ²). . . .	98
4.30	(a) Active balun. (b) Output buffer. Circuit parameters of active balun: $W_{1,2} = 300\mu\text{m}$, $R_{s1}, R_{D1}, R_{D2} = 200\Omega$. Circuit parameters of source follower : $W = 300\mu\text{m}$. $R_s=1\text{k}\Omega$. Length of all transistors is $0.13\mu\text{m}$	99
4.31	Die photo-micrograph of charge-domain sampler with embedded 4-path band-pass filter with probes in place for on-wafer measurement.	99
4.32	Measurement set-up.	100
4.33	Measured quadrature output voltage of mixing sampler with input at 100.1 MHz.	102
4.34	Measured and simulated normalized transfer function of mixing sampler. . .	102
4.35	Measured tuning range of mixing sampler.	103
4.36	Post-layout simulated IIP3.	103
4.37	Simulated P_{1dB}	104
4.38	Post-layout simulated IMR.	104
5.1	Frequency response of sinc, sinc ² and sinc ³ . $f_{s,fir}=10\text{ MHz}$, decimation ratio is 2.	107
5.2	Advanced charge-domain sampler with embedded N-path band-pass filter.Circuit Parameters: $gm_1 = 2\text{mS}$, $gm_4 = 1.5\text{mS}$, $gm_6 = 4.5\text{mS}$, $I_{b1} = 150\mu\text{A}$, $I_{b3} = 235\mu\text{A}$, $I_{b5} = 700\mu\text{A}$, $V_b = 335\text{mV}$	108
5.3	Response of 4-path band-pass filter in Fig. 5.2 (v_{o1} excluding M3-M6 and CDS).109	
5.4	High-order windowed charge-domain sampler. Circuit Parameters: $g_m=1.5\text{ mS}$, $C_{S1}=10\text{ pF}$, $C_{S2}=1\text{ pF}$	110
5.5	Simulated gain-normalized transfer function of proposed charge-domain windowed sampler with 100 MHz input.	111
5.6	Simulated time response of the output signal with $V_{in} = 50\text{mV}$, $f_{in} = 100.2\text{ MHz}$, $V_{out} = 170\text{ mV}$, $f_{out} = 200\text{ KHz}$, $f_{s,out}= 25\text{ MHz}$	112
5.7	Simulated time response of the output signal with $V_{in}=50\text{ mV}$, $f_{in} = 100.2\text{ MHz}$, $V_{out} = 170\text{ mV}$, $f_{out} = 200\text{ KHz}$, $f_{s,out}= 25\text{ MHz}$	113
5.8	Post-simulated time response of the output signal with $V_{in}=40\text{ mV}$, $f_{in} = 100.2\text{ MHz}$, $V_{out} = 140\text{ mV}$, $f_{out} = 200\text{ KHz}$, $f_{s,out}= 25\text{ MHz}$	113

List of Symbols

<i>ADS</i>	Advanced Design Systems
<i>AI</i>	Active Inductor
<i>AM</i>	Amplitude Modulation
<i>BP</i>	Band-Pass
<i>CAD</i>	Computer-Aided Design
<i>CDS</i>	Charge-Domain-Sampler
<i>CHF</i>	Channel Selection Filter
<i>CMOS</i>	Complementary Metal-Oxide Semiconductor
<i>dBm</i>	Decibel power with respect to 1 Milliwatt
<i>EM</i>	Electromagnetic
<i>EPC</i>	Gen2 Electronic Product Code Generation 2
<i>FF</i>	(nMOS)Fast-(pMOS)Fast
<i>FM</i>	Frequency Modulation
<i>FS</i>	(nMOS)Fast-(pMOS)Slow
<i>FSK</i>	Frequency-Shift Keying
<i>IMF</i>	Image Rejection Filter
<i>ILAIO</i>	Injection-Locked Active Inductor Oscillator
<i>ILO</i>	Injection-Locked Oscillator

<i>ILFD</i>	Injection-Locked Frequency Divider
<i>ISM</i>	Industrial Scientific Medical (radio bands)
<i>ISO</i>	International Organization for Standardization
<i>LC</i>	Inductor-Capacitor
<i>LNA</i>	Low Noise Amplifier
<i>LO</i>	Local Oscillator
<i>LP</i>	Low-Pass
<i>MIM</i> (<i>-cap</i>)	Metal-Insulator-Metal (Capacitor)
<i>nMOS</i>	n-channel Metal-Oxide Semiconductor
<i>PLL</i>	Phase-Locked Loop
<i>pMOS</i>	p-channel Metal-Oxide Semiconductor
<i>POR</i>	Power-ON Reset
<i>PVT</i>	Process (supply-)Voltage Temperature
<i>RF</i>	Radio Frequency
<i>RFID</i>	Radio Frequency Identification system
<i>RLC</i>	Resistor-Inductor-Capacitor
<i>SAW</i>	Surface Acoustic Wave
<i>SDR</i>	Software Defined Radio
<i>SF</i>	(nMOS)Slow-(pMOS)Fast
<i>SS</i>	(nMOS)Slow-(pMOS)Slow
<i>TT</i>	(nMOS)Typical-(pMOS)Typical
<i>UHF</i>	Ultra High Frequency
<i>VCO</i>	Voltage-Controlled Oscillator

Chapter 1

INTRODUCTION

1.1 Background

Communication systems are the foundation of information transfer. Based on the transmission media, communication systems are generally categorized into wireless and wireline communications. Wireline communications is often referring to high speed signaling through cables, or micro-strip, which is used in a wide variety of digital systems, i.e. the computer, digital television, sensor networks and data storage center, to name a few. It is now the dominant method for long distance telecommunications and extremely high speed data transmission in short range, e.g. field programmable gate arrays (FPGA) to memory, graphics processing unit (GPU) to memory and Gigabit Ethernet. Oscillators are widely used as local clock generators in phase-lock loop and clock distributions network. Unlike wireline communications, wireless communications is usually making use of radio to transfer information between two or more points which are not physically connected via any electrical conductors. The dramatically increased demand from cell phones and portable mobile products is a drive force to make wireless communications to be the fastest growing segment of the communications industry in the past two decades [1]. The design of low-power, low-cost and high performance radio frequency (RF) transceivers becomes a challenge. Most of the transceivers extensively use filters and oscillators as local oscillators, RF filters, intermediate frequency (IF) filters and channel selection filters, which cover the frequencies from 200 KHz to multi-GHz, depending on their locations in the transceivers [2].

One of the key components in transceivers is the frequency synthesizer, synthesizing various RF frequency according to the architecture of transceivers and communication standards. In the integer-N frequency synthesizer, the pre-scalar is the first stage to lower the frequency by integer division. In general, pre-scalars are implemented in a digital form by two static latches connected in a negative feedback loop. It can also be implemented by dynamic latches, e.g. true single-phase clock (TSPC) based divider. The popularity of these two types of digital dividers in RF transceivers is because it is widely believed that the simple structure, the larger bandwidth, and the better robustness of digital dividers over process variations outperform their analog counterparts, e.g. Miller frequency divider [3, 4] and parametric frequency divider [5]. For both static and dynamic pre-scalars, however, a trade-off between the speed and power consumption becomes more critical as the speed increases. The solution to balance the performance and power dissipation is to use injection-locked oscillators to substitute the conventional digital divider.

When an incident signal is applied to the oscillator, it is changed from a free-running oscillator to a forced oscillator. The free-running frequency shifts towards the frequency of the incident signal under a certain condition. The detailed description will be given in Chapter 2.1. A simple injection-locked frequency divider (ILFD), so called super-harmonic injection-locked oscillator, is an negative resistor pair LC tank oscillator. The incident signal with higher frequency is injected into the tail transistor. The output of the differential pair shows that the frequency is divided by 2, which fulfils the function of pre-scalar. This structure was analyzed in terms of phase limited and amplitude limited locking range and the noise characteristics in [6]. It achieved locking range by 12.3% at 3 GHz, and later it was used as a pre-scalar to construct a PLL in [7]. Instead of injecting the signal to the tail transistor, the injection signal can be directly injected into the LC tank. [8] proposed a low power quadrature generation circuit by injecting signals to two identical ILFDs. A hard switching model was conceived to give rise to simple expressions for the lock range and output amplitude. [9] presented a wider lock-range high-speed pre-scalar at 50 GHz with a combination of injection-locked oscillators. Except for divide-by-2, odd number super-harmonic ILFD was reported [10, 11, 12, 13, 14, 15]. In [14] and [15], the author presented a divided-by-3 pre-scalar, running at higher than 100 GHz frequency. For these designs,

one extra inductor or even more inductors were required to create high impedance at $3\omega_o$ (ω_o is the fundamental frequency). A current-mode logic frequency divider was described in [16], which showed 4.1 GHz lock range at 24 GHz frequency. The divide-by-4 was obtained through two divider stages with 0.8 V power supply. It overcame the constrain that the low power supply limits the highest achievable frequency of current mode logic. Apart from injection-locked frequency divider, quadrature injection-locked oscillators are exceptional candidates that can be employed in the low-power high-performance quadrature clock generators [17, 18, 19, 20, 21, 22]. Injection-locked oscillators can also be found in the wire-line communications, e.g. reducing timing jitter and clock skew [23, 24, 25, 26, 27, 28]. Among these applications, the majority is the LC tank based oscillators due to their better noise performance and lower power dissipation. Moreover, there are some other kinds of oscillators for different applications, such as ring oscillators and relaxation oscillators.

Owing to their sensitivity to temperature variation and supply voltage fluctuation, non-harmonic oscillators such as relaxation oscillators are widely used in passive wireless microsystems (PWMs) such as implanted medical devices, embedded sensors, and radio-frequency identification tags to generate system clocks that control both the operation of PWMs and their communications with base stations. A stringent frequency requirement for the system clock exists. For example, EPC radio-frequency identity protocols class-1 generation-2 UHF RFID protocols require that the accuracy of the frequency of the backscattered data be bounded by $\pm 4\%$ [29]. Arising from the effect of process spread, supply voltage fluctuation, and temperature variation (PVT), the frequency of these oscillators exhibits a large degree of uncertainty. For example, the variation of the frequency of a free-running oscillator can be as large as $\pm 20\%$ [30]. The uncertainty of the frequency of the system clock of PWMs is further escalated due to the fact that these systems are usually fabricated using low-cost CMOS technologies, which typically have a high degree of process spread. Calibrating the system clock of PWMs prior to their operation is required to ensure the proper operation of PWMs. The effect of supply voltage fluctuation and temperature variation can be compensated using bang-gap circuits [31, 32], their effectiveness is largely hindered by the limited power resources of PWMs, which severely limits the degree of the complexity of compensation circuitry subsequently their performance. Although a number of techniques

such as digital trimming [33] and phase-locked loops [34] were used to perform the remote calibration of system clocks, both suffer from a long calibration time and high power consumption. Injection-locking that offers the intrinsic advantage of fast-locking, high frequency accuracy, small fluctuation in power flow, and improved phase noise performance emerged as a power-efficient method to calibrate the system clock of PWMs. Both the carrier [35] and envelope [36] of the signal from the base station were used as injection-locking signals. Injection-locking was also used in calibration of power oscillators for inductive power links [37], the fine frequency tuning of quadrature oscillators [38], self-cascade body-coupled oscillators for biomedical telemetry [39], wake-up receivers for wireless body area networks [40], and FSK transceivers for body sensor networks [41], to name a few. Because the maximum emission power from the base station is regulated, for example, in both EPC and ISO 18000-4, it is 4 watts EIRP (Equivalent Isotropically Radiated Power) and RF power drops quadratically with the distance between transmitters and receivers, the voltage generated by the antenna of PWMs for injection-locking is rather low. As a result, the success of injection-lock based remote frequency calibration is critically determined by the lock range of oscillators. Oscillators with a large lock range are highly desirable.

The other part that determines the performance of the transceivers is the architecture of the RF transceivers. Fig. 1.1 shows three possible architectures of the receivers. The most widely used architecture in RF world that has been for many decades is the super-heterodyne receiver, invented by Armstrong in 1917 [42]. It needs two analog mixers to complete two stages frequency translation, in which, at the first stage RF is translated to IF, and then in the second stage it is from IF to baseband signal. The diagram of this receiver is illustrated in Fig. 1.1(a).

In the super-heterodyne receiver, the incoming signal is selected by the high-Q band-selected filter and then amplified by the low-noise amplifier (LNA). To reject the strong signals in order to avoid blocking of the receiver, such a filter must be designed to have very high Q-factor, e.g. Q is larger than 100 for digital TV broadcasting. The discrete components, Surface Acoustic Wave (SAW) filters, are more common to be employed to meet the stringent requirements. An image rejection filter (IMF) is indispensable to be

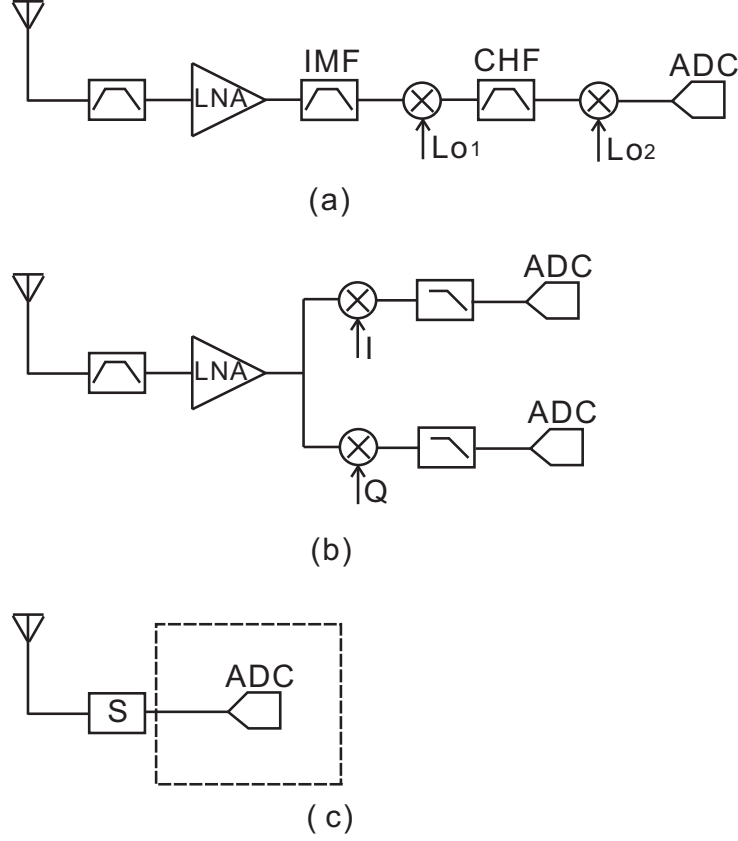


Figure 1.1: Three receiver architectures: (a) Super-heterodyne receiver, (b) Zero-IF receiver, and (c) SDR receiver.

inserted between LNA and Mixer to filter out the image signal. The signal at the output of the mixer is translated to a lower frequency, where analog or digital processing is easier to perform. A channel selection filter (CHF) performs channel selection at the IF. The last stage is to ensure that the desired signal is in baseband following by an analog-to-digital converter (ADC) to eventually quantize analog signal [43, 44, 45, 46]. Although the super-heterodyne receivers are quite successful because of their simple structure and high selectivity, they suffer from several drawbacks, e.g. less attractive for highly integrated receiver because of external filters, extra rejections for image signals and impedance matching network in the intermediate stage requiring more design effort.

To eliminate the extra image rejection filters, zero-IF receivers is then proposed in Fig. 1.1(b). The key concept of this type receiver is to make LO's frequency same as RF signal, converting modulated RF signal to DC directly, thereby resolving image signal

problem. The selected RF signal is multiplied by I/Q clock, generated from quadrature LO, to allow the receiver to choose high-side or low-side injection [47, 48, 49]. In [49], an ultra wide band receiver to cover frequency, 3 - 10 GHz, was presented. A LNA with embedded notch filter, providing average -25 dB gain over wide frequency band, with tuning capability to attenuate other interferences was introduced. One step frequency translation and unnecessary image rejection filters are the major benefits of zero-IF receivers. However, the unavoidable drawbacks, e.g. DC offset errors because of LO-self mixing, LO leakage due to parasitic paths, intrinsic flicker noise of MOSFET transistors adding on top of the desired signal and I/Q mismatch [2, 50], existing in this architecture are still concerns.

The rapid advance of CMOS technologies has reached the level that analog RF systems can be implemented in such a way that sampled-data and digital signal processing techniques that traditionally championed in low-frequency applications can be utilized in design of RF front-end to reduce cost, improve performance, and enhance reconfigurability. Therefore, the optimal receiver with maximum flexibility and lowest cost for a receiver can be realized by pushing ADC towards antenna, Fig. 1.1(c). The RF signal will be directly sampled and quantized through ADC, introducing baseband digital signal processing into RF. The ADC must be very linear and is capable to deal with large variation of signal range. Unlike analog mixers, the frequency translation can be done in digital domain, minimizing phase and gain error over wideband, which is the inherent obstacle in analog mixers. Such a concept, defined as software-defined radio (SDR) and was first proposed by Mitola in 1995 [51], and become more important recently. The importance of this architecture also stems from more complex spectrum planning, which was specified by different organizations (ITU, IEEE, 3GPP and etc.). Fig. 1.2 shows a couple of examples in the spectrum of 50 MHz to 4 GHz, including short-range communication standards RFID, mobile digital TV standard DVB-T, cellular standards GSM, UMTS, and LTE, and the wireless networking standards Wi-Fi and WiMAX.

However, design such an ADC, meeting all the requirements, become more challenge. For example, ADC, applying to SDR receiver directly, must have sufficient dynamic range and handle both low and high power signals without any high-Q filtering [52]. As a result,

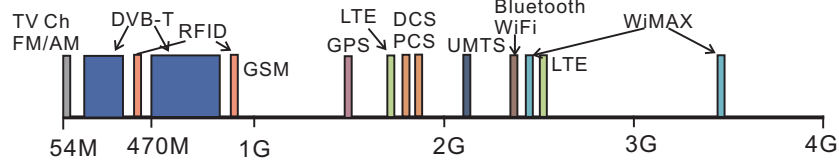


Figure 1.2: Spectrum allocation for wireless communications.

unacceptable power dissipation, usually in Watts, overwhelms benefits of the architecture. In comparison with pushing ADC towards antenna, as transceivers can be loosely partitioned into RF analog front-end and digital back-end with the digital back-end fully programmable, to have reconfigurable RF analog front-ends is more attractive.

1.2 Motivation and Objectives for Injection-Locked Oscillators

1.2.1 Injection-Locked Active Inductor Oscillators

The oscillators that are employed in data communications over wireless systems are typically LC oscillators with spiral inductors or transformers, owing to the stringent phase noise requirements. On the other hand, LC oscillators suffer from small lock range without paralleling a number of varactors due to the passive components, e.g. passive inductors and capacitors, which also lead to large silicon consumption. One way to combat these problems is to use active devices, which provide a large tuning range of impedance, to substitute the passive devices, especially the large inductors are replaced with active inductors (AI), and varactors are removed thereby saving a large amount of silicon area. Active-inductor-based oscillators, however, exhibit poor noise performance attributed to the more noisy devices being used. [53] showed that phase noise of an injection-locked oscillator can be reduced to the level comparable to that of the injecting signal in the lock state. The ability to lower the phase noise of injection-locked active inductor oscillators (ILAIO) to the level of the external "clean" signal and the large frequency tuning range make active inductor oscillators particularly attractive for injection-locked frequency dividers [54, 55, 13, 56, 57, 58]. Also

the relative poor phase noise of injection-locked active inductor oscillators is not of a critical concern for some applications, e.g. phase shifters [59] and limiting amplifiers [60].

The analytical study of phenomenon of injection locked oscillators was first presented by Adler [61]. Later Razavi derived the well-known equations of lock range for CMOS oscillators in [53] by making use of a phasor domain approach. Recent published papers [62, 63, 64], using different approaches to explain the locking process, continue to disclose new findings. None of them, however, can be applied to the injection-locked active inductor oscillators thereby deeply exploring the lock range. The mechanism of why ILAIOs provide large lock range is still unclear although it has been reported in many publications. Therefore, there is no doubt that the need to explore the relation between the lock range and the active inductor oscillator is of interest.

In this dissertation these issues will be resolved by exploiting 1) the intrinsic relation between the lock range and the injection-induced variation of the impedance of LC tank, 2) the lock range of injection-locked active inductor oscillators attributed to both the low quality factor and the large injection-induced variation of impedance. In addition, a simple but effective approach to derive the expression of the lock range will be presented.

1.2.2 Injection-Locked Non-Harmonic Oscillators

The preceding introduction for different applications of injection-locked oscillators will eventually come to the most widely studied subject: How to increase the lock range of injection-locked oscillators. A number of novel design techniques emerged to increase the lock range of injection-locked LC frequency dividers. Chang *et al.* showed that the lock range can be increased if the dc component of the voltage of the output of the oscillator is used to tune the varactor of the oscillator [65]. This is essentially a varactor-tracking technique that automatically forces the varactor voltage to track the control voltage of the oscillator so as to achieve an effective large lock range even though the absolute lock range of the oscillator is not increased. Since the lock range of injection-locked LC oscillators is inversely proportional to the quality factor of the oscillators, lowering the quality factor of the oscillators will effectively increase the lock range. Both series resistance [66] and shunt

resistance [67] methods emerged to achieve this. To increase the lock range, the strength of internal locking signals that actually mixes with the output of the LC tank and determines the lock range must be maximized. Wu and Hajimiri showed that although the strength of an external injection signal is high, its strength is severely attenuated by the parasitic capacitances of the path over which the actual locking signal is generated. As a result, only a small lock range can be achieved in spite of a strong external injection signal [68]. To combat this, the internal locking signal must be maximized prior to mixing. Inductive series-peaking [69], sub-threshold mixing [10], and transformer positive feedback [70] have been proposed for this purpose. To determine the lock range of ring oscillators, a time-domain approach was given in [71]. Although a ring oscillator can lock to a locking signal injected to only one node of the oscillator, a larger lock range can be obtained if the locking signal is injected into the multiple stages of the oscillator simultaneously [72, 73]. The lock range can be further increased if the phase of each of the multiple injections is properly chosen [69, 74]. Jin *et al.* showed that the lock range of injection-locked ring oscillators can be improved by employing a feedback resistor between the input and output of the oscillators [75]. The inserted resistance effectively lowers the quality factor of the oscillators so as to boost the lock range. Injection-locked relaxation oscillators were also studied in [76, 77, 78]. Soltani and Yuan showed that integrating feedback that integrates the difference between the frequency of the injection-locking signal and that of relaxation oscillators improves lock range [36].

The preceding narrow-band techniques for lock range enhancement of LC oscillators are not applicable to non-harmonic oscillators due to the fact that an infinite number of frequency components exist at the output of non-harmonic oscillators whereas only a single-frequency component exists at the output of LC oscillators. The latter permits the use of impedance peaking techniques at a selected frequency and location to maximize the effective internal locking signal so as to achieve a large lock range. Although ring oscillators in several designs have been demonstrated to be able to yield a larger lock range, an in-depth study of the mechanism and factors that determine the lock range of non-harmonic oscillators and methods that increase the lock range of these oscillators are critically needed but not available yet.

In this dissertation, the missing points will be added in the following chapters, including 1) an analytical treatment of the intrinsic relation between the phases of the multiple injection signals, which is essential in design of non-harmonic oscillators with multiple injections in order to yield a large lock range, 2) the intrinsic relation between the lock range of non-harmonic oscillators with single injection and that with multiple injections, though fundamentally important in understanding why non-harmonic oscillators with multiple injections can yield a large lock range, and 3) a comprehensive study of lock range for single-tone and multi-tone injections for non-harmonic oscillators, which was not appeared in any publications.

1.3 Motivation and Objectives for Charge-Domain Sampling Circuits with Tunable Band-Pass Filter

To handle different requirements for signal bandwidths and data rates, the most of commercial transceivers are often realized either by integrating multiple silicon component cores optimized for individual wireless standard on the same substrate or by packaging multiple silicon chip sets. Both approaches are costly. In addition, they provide inflexibility in coping with new standards in wireless communications. To overcome it, a number of design techniques have emerged for silicon implementation of SDR. Among them, charge-domain windowed sampling that provides an inherent sinc low-pass characteristic with FIR filtering to attenuate unwanted channels, suppresses the fold-over of broadband noise to the desired baseband, and nulling out aliasing interferences while exhibiting a low sensitivity to clock jitter and consuming less power is a promising technique [79]. Muhammad and Staszewski showed that IIR filtering from the recursive operation of a history capacitor(charge residual) and rotating capacitors(charge shared) provide an additional 20 dB stop-band attenuation [80, 81]. However, it can only be applied to the bluetooth frequency band. By changing the sampling frequency, the ratio of the capacitance of the history capacitor to that of the rotating capacitors, and the number of the rotating capacitors, the characteristics of built-in low-pass and anti-aliasing filter can be made programmable [82, 83]. Unfortunately, these

designs are less attractive because of the necessary of the external pre-selection for the suppression of out-of-band interferences. The active integrators employed in the designs also degrade the noise figure and linearity. Because a channel typically occupies a frequency band rather than a single frequency, the suppression of unwanted tones provided by these filters in the neighbor of the nulls is often insufficient [84, 85]. Increasing the sampling frequency, though improving the suppression of unwanted tones in the vicinity of the nulls to a certain extent, increases power consumption. Mrizaei *et al.* showed that anti-aliasing and low-pass filtering from charge-domain windowed sampling can be improved simultaneously by employing sinc^2 filtering [52, 74, 86]. Yoshizawa and Iida proposed a wide-band charge-domain baseband filter [87]. However, fixed-centre-frequency band-pass filter is still required in those receivers, making charge-domain sampling circuits less attractive for the increasing complexity of frequency bands. Recently, N-path filters widely popular in switched-capacitor band-pass filters have attracted a great interest to realize programmable high-Q band-pass filters [88, 89, 90]. The tunable center frequency and bandwidth, low cost, and full compatibility with digital CMOS make these filters particularly attractive for SDR. The common issue for the presented design is the lack of sufficient attenuation for the undesired signal accompanying with wanted signal deteriorates signal-to-noise ratio(SNR). In particular if the aliasing signal is on top of the desired signal, there is no doubt that the sensitivity of the receiver is lowered. The worst case is a large out of band or in band interference will block the receiver, severely degrading the performance of the overall RF communication system.

In this dissertation, the lack of filtering functions will be tackled by proposing new architectures, including 1) a new charge-domain quadrature downconversion circuit with a tunable band pass filter, 2) a new charge-domain sampling circuit with high-order FIR filter embedded. The sufficient study of principles of periodic impulse sampling, periodic windowed sampling, and periodic N-path windowed sampling will also be provided. Detailed mathematical treatments of charge-domain windowed samplers will be given.

1.4 Contributions

The original contributions of the dissertation are summarized in this section.

1.4.1 Injection-Locked Oscillators

In this dissertation, the indispensable mathematical treatments for enlarging the lock-range of the ILAIOs are given, exploring the mechanism of how ILAOs are able to offer large lock range thereby providing a clear guidance of deigning ILAIOs. In addition, a systematic and in-depth investigation for the injection-locked non-harmonic oscillators are completed. Several approaches are proposed to widen the lock range of non-harmonic oscillators, making them particularly attractive for applications such as PWMs where the accuracy of the frequency generated from the local oscillator is heavily affected by PVT. The contributions are listed as below:

1. Formalized the intrinsic relation between the lock range and the injection-induced variation of the impedance of LC tank.
2. Explored the mechanism of enlarging the ILAIOs.
3. Proposed a simple but effective approach to analyze the injection-locked oscillators.
4. Proposed a new approach to widen the lock range of the injection-locked non-harmonic oscillators.
5. Formalized the impacts on the lock range from different phase and tones of injections.

Extensive simulation results associated with the injection-locked active inductors and non-harmonic oscillators are presented.

1.4.2 Tunable Band-Pass Filter Embedded Charge-Domain Sampling Circuits

A novel sampling mixer with programmable centre frequency of the band-selection filter and -3 dB frequency of the anti-aliasing filters are proposed, providing a large freedom

of selection of any frequency band signals without using discrete components. The time-interleaved structure are utilized to achieve the optimal aliasing rejection. And the -3 dB frequency is controlled by the sampling clock. The contributions include:

1. Proposed a novel architecture for software-defined radio.
2. Proposed a high-order embedded FIR filter in the sampling circuit.
3. Completed a in-depth study of periodical N-path sampling and charge-domain sampling.
4. Provided a unique noise analysis for the new architecture.

The detailed mathematical analysis and circuit simulation results of the proposed circuits are given. The layout and on-chip wafer measurement results of the circuits are provided.

1.5 Thesis Organization

The rest of the thesis is organized as follows:

- Chapter 2 presents a systematic study for the injection-locked active inductor oscillators. In the mean time, an novel approach to analyze the lock range of the injection-locked oscillators is also provided. The relation between the lock range and the impedance variation of active inductor oscillators is given.
- Chapter 3 presents a detailed investigations on injection-locked non-harmonic oscillators. The lock range of multiple multi-tone injection-locked oscillators is formalized. An example, relaxation oscillator, is used to verify the findings.
- Chapter 4 presents a low-power tunable band-pass filter embedded quadrature down-conversion sampling circuit for SDR. In this chapter, mathematical derivation for the sampling network is provided and circuit implementation is shown.

- Chapter 5 presents an alternative charge-domain sampling circuit with high-order sinc filter embedded. The circuit implementation is given, accompanied with simulations and measurements.
- Chapter 6 draws conclusions and brings some future research directions.

Chapter 2

Injection-Locked Active Inductor Oscillators

In this chapter, the lock range of injection-locked active inductor oscillators is derived in analogous to the analysis of oscillators in a linear feedback system. Making use of this novel approach, the relation between injection ratio and impedance variation of injection-locked oscillators and lock range is analyzed analytically. The remaining of the chapter is organized as the follows: This chapter starts from introduction of injection-locked oscillators in Section 2.1. It is followed by a brief description of active inductor oscillators in Section 2.2. A study of lock range for LC tank oscillators is given in Section 2.3. Section 2.4 explores the intrinsic relation between lock range and impedance variation of injection-locked oscillators. A case study is presented in Section 2.5. A summary is provided in Section 2.6.

2.1 Injection-Locked Oscillators

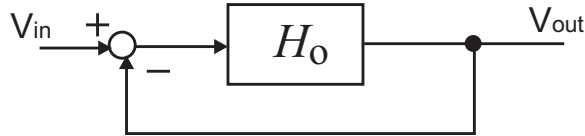


Figure 2.1: A feedback system.

A typical feedback system with unity loop gain is illustrated in 2.1, the transfer function is given as

$$\frac{V_{out}}{V_{in}}(j\omega) = \frac{H_o(j\omega)}{1 + H_o(j\omega)} \quad (2.1)$$

Unlike an amplifier with negative feedback, which is often to set enough phase margin at the unity-gain frequency to make the feedback stable, in the self-sustaining autonomous system, a unstable negative feedback is desired. From 2.1, if $H_o(j\omega_o)=-1$, the loop gain approaches infinity. A noise component at ω_o experiences a total gain of unity and a phase shift of 180° , returning to the subtractor as a reversed input signal. The output of subtractor becomes larger and continuous to grow. As a result, an oscillating signal is obtained. In general, if a negative-feedback system with loop gain satisfies "Barkhausen criteria".

$$\begin{aligned} |H_o(j\omega_o)| &\geq 1 \\ \angle H_o(j\omega_o) &= 180^\circ \end{aligned} \quad (2.2)$$

the feedback system may oscillate at ω_o .

In an ideal "LC tank" circuit, a charged capacitor is connected to an inductor, this charge will flow back and forth between the inductor and capacitor, causing voltage across the capacitor to oscillate at the frequency of $\omega_o=1/\sqrt{LC}$. In other words, the impedance of the inductor and the capacitor are equal and opposite, resulting open-circuit at ω_o ideally. In reality, real inductor and capacitor are always associated with parasitic resistances in which partial energy is absorbed, yielding a decayed waveform. To maintain oscillation, negative resistances are placed in the tank to compensate the parasitic resistances. Such a circuit configuration is given a name as cross-coupled LC oscillator [91]. If an incident signal, I_{inj} , operating at ω_{inj} , is injected into the tank, the tank is under perturbation, which is so called injection process, as shown in Fig. 2.2.

As the injection signal is increased from weak to relatively strong, and the frequency of the injection signal is close enough to ω_0 , the output of the oscillator is starting to be

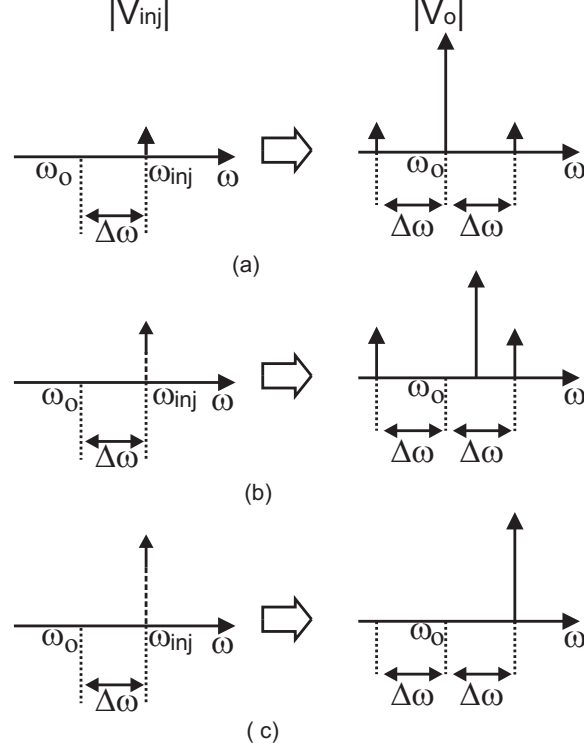


Figure 2.2: Injection locked procedure represented in simplified spectrum diagram. (a) Unlocked, (b) Fast beat, and (c) Locked.

pulled towards the injection signal and eventually is synchronized with it. The condition for the synchronization was first examined by Alder [61] in 1946.

$$\frac{E_1}{E} = 2Q \frac{\Delta\omega}{\omega_0}. \quad (2.3)$$

Where E_1 and E are the impressed voltage and the oscillating voltage respectively. Q denotes the quality factor of the tank. ω_0 and $\Delta\omega$ are free-running frequency and the maximum difference between the frequency of the injection signal and the free-running frequency of the oscillator over which a lock state can be established. Although the pioneering work of Adler on injection-locking in oscillators has been widely accredited, the phasor domain treatment of the injection-locking and pulling of oscillators by Razavi provides the much

needed insight of the locking and pulling processes of oscillators under injection [53].

$$\Delta\omega = \frac{\omega_o}{2Q} \frac{I_{inj}}{I_o} \frac{1}{\sqrt{1 - \left(\frac{I_{inj}}{I_o}\right)^2}} \quad (2.4)$$

where I_{inj} is the amplitude of the injection current, and I_o is the amplitude of the current of the LC tank. If $I_{inj} \ll I_o$, i.e. weak injection, (2.4) is simplified to

$$\Delta\omega \approx \frac{\omega_o}{2Q} \frac{I_{inj}}{I_o}. \quad (2.5)$$

It is seen from (2.5) that the lock range of the oscillator is directly proportional to the strength of the injection signal and inversely proportional to the current and quality factor of the LC tank.

2.2 Active Inductor Oscillators

CMOS active inductors are active networks that consist mainly of MOS transistors. As compared with their spiral counterparts, CMOS active inductors offer many advantages, e.g. a large amount of silicon area saving, large and tunable inductance and more compatibility with digital CMOS technologies [92]. Passive capacitors may be added in the circuits to change frequency. Sometimes resistors are used as feedback elements to improve performance of active inductors. When the active networks are biased properly, the networks exhibit an inductive characteristic at a specific frequency range. Fig. 2.3 shows an active inductor network, where C_1 and G_{o1} , C_2 and G_{o2} denote the total capacitances and conductances at nodes 1 and 2 respectively.

The admittance looking into port 2 of the network is shown as:

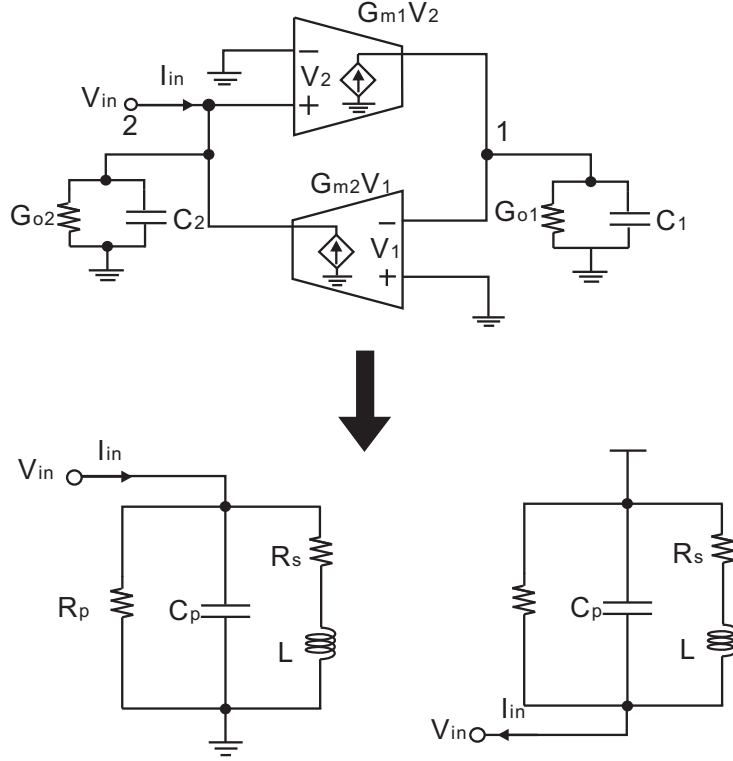


Figure 2.3: Single-ended active inductor.

$$\begin{aligned}
 Y &= \frac{I_{in}}{V_2} \\
 &= sC_2 + G_{o2} + \frac{1}{s \left(\frac{C_1}{G_{m1}G_{m2}} \right) + \frac{G_{o1}}{G_{m1}G_{m2}}}.
 \end{aligned} \tag{2.6}$$

(2.6) can be represented by equivalent RCL circuit in Fig. 2.3 with its parameters given by

$$\begin{aligned}
 R_p &= \frac{1}{G_{o2}} \\
 C_p &= C_2 \\
 R_s &= \frac{G_{o1}}{G_{m1}G_{m2}} \\
 L &= \frac{C_1}{G_{m1}G_{m2}}.
 \end{aligned} \tag{2.7}$$

It can see from (2.7), the resonant frequency is $\omega_0 = \sqrt{(G_{m1}/C_1)(G_{m2}/C_2)}$. And also the tuning range of the inductance is determined by C_1 , G_{m1} and G_{m2} , which in general $G_{m1,2}$ is controlled by DC biasing voltage. Fig. 2.4 lists some of examples. In Fig. 2.4(a), Wu current reuse active inductor will be used to construct an oscillator for the rest of study [93]. Fig. 2.4(b) use NMOS and PMOS to form an inductor [94]. The simplest active inductor [95] is illustrated in Fig. 2.4(c).

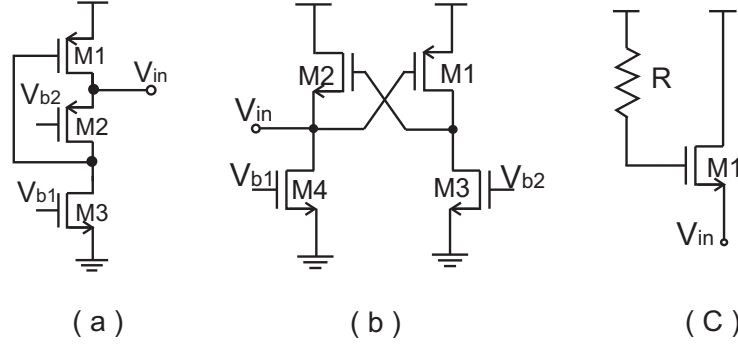


Figure 2.4: Examples of active inductors. (a) Wu current reuse active inductor , (b) Lin active inductor , and (c) Hara active inductor

2.3 Lock Range of Generic LC Oscillators

Consider the simplified schematic of an injection-locked LC oscillator shown in Fig. 2.5(a). The inverting buffer is needed in order to satisfy Barkhausen criteria. Let I_{inj} denote the injection signal and Z_T denote the impedance looking into the LC tank. Since $I_o + I_T = I_{inj}$ and $I_o = -g_m Z_T I_T$ where g_m is the transconductance of the transistor, the injection-locked oscillator can be represented by the familiar block diagram used in control systems shown in Fig. 2.5(b) with I_{inj} the input, I_T the output. Note that Fig. 2.5(b) is a linear system when locked. When the injection signal is absent, the oscillator is an autonomous system that oscillates at ω_o , the self-resonance frequency of the LC tank.

When a sinusoidal signal of frequency $\omega_{inj} = \omega_o + \Delta\omega$ is injected and the oscillator is locked to the injection signal, it will oscillate at $\omega_o + \Delta\omega$. Since $\omega_{inj} \neq \omega_o$, the impedance of

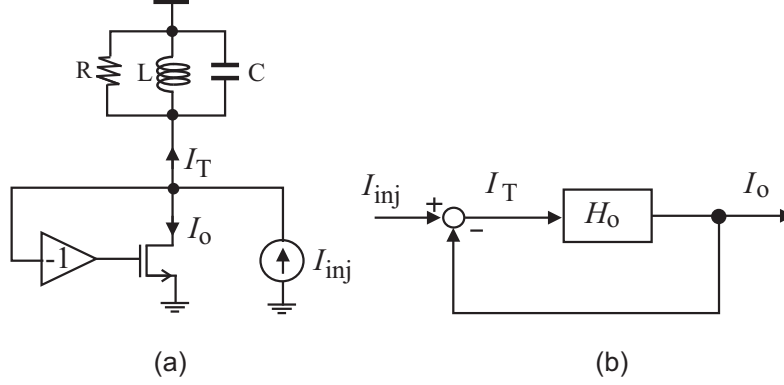


Figure 2.5: (a) Injection-locked oscillators. (b) Block diagram of injection-locked oscillators.

the LC tank at $\omega_o + \Delta\omega$ will deviate from its value at ω_o , as illustrated graphically in Fig. 2.6. Clearly

$$Z_T(\omega_o + \Delta\omega) = Z_T(\omega_o) - \Delta Z_T \quad (2.8)$$

where ΔZ_T is the injection-induced impedance variation of the LC tank. Since $\Delta\omega$ is caused by I_{inj} , ΔZ_T is also a function of I_{inj} . Further, since $\Delta\phi$ and ΔZ_T are determined by Barkhausen criteria for oscillation, the same amount of phase and impedance variation is required to satisfy Barkhausen criteria regardless whether the quality factor of the LC tank is high or low. As a result, for the same injection signal, the high the quality factor of the LC tank, the smaller the frequency variation $\Delta\omega$, as illustrated graphically in Fig. 2.6.

Now let us consider the control system of Fig. 2.5(b). When the oscillator is locked to the injection signal, it will oscillate at $\omega_o + \Delta\omega$ and

$$I_o(\omega_o + \Delta\omega) = \frac{H_o(\omega_o + \Delta\omega)}{1 + H_o(\omega_o + \Delta\omega)} I_{inj}(\omega_o + \Delta\omega). \quad (2.9)$$

Note that in (2.9) the oscillating frequency is explicitly stated as we are only interested in the behavior of the oscillator in the lock state. Assume that $\Delta\omega \ll \omega_o$, which is often the

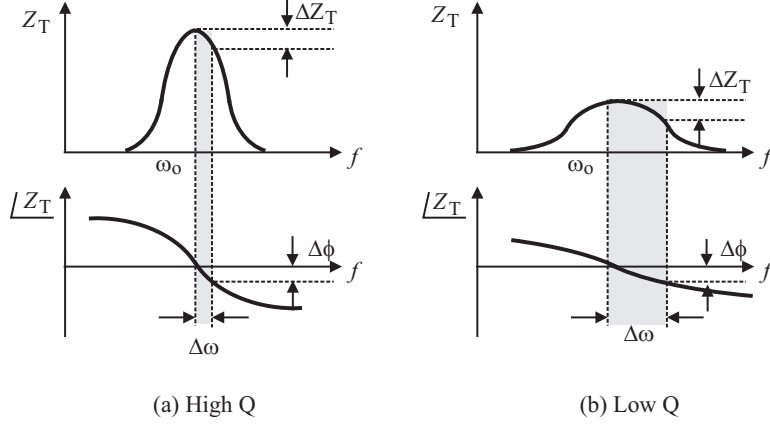


Figure 2.6: Impedance of the LC tank of injection-locked LC oscillators.

case, the first-order approximation

$$H_o(\omega_o + \Delta\omega) \approx H_o(\omega_o) + \left[\frac{\partial H_o(\omega)}{\partial \omega} \right]_{\omega_o} \Delta\omega \quad (2.10)$$

can be utilized to simplify (2.9)

$$I_o(\omega_o + \Delta\omega) \approx \frac{H_o(\omega_o + \Delta\omega)}{1 + H_o(\omega_o) + \left[\frac{\partial H_o(\omega)}{\partial \omega} \right]_{\omega_o} \Delta\omega} I_{inj}(\omega_o + \Delta\omega). \quad (2.11)$$

The first-order approximation is only valid if the injection is weak. Since the injection signal is absent, $1 + H_o(\omega_o) = 0$, i.e. Barkhausen criteria, (2.11) is simplified to

$$I_o(\omega_o + \Delta\omega) \approx \frac{H_o(\omega_o + \Delta\omega)}{\left[\frac{\partial H_o(\omega)}{\partial \omega} \right]_{\omega_o} \Delta\omega} I_{inj}(\omega_o + \Delta\omega). \quad (2.12)$$

Focusing on the amplitude only

$$|I_o(\omega_o + \Delta\omega)| \approx \frac{|H_o(\omega_o + \Delta\omega)|}{\left| \frac{\partial H_o(\omega)}{\partial \omega} \right|_{\omega_o} |\Delta\omega|} |I_{inj}(\omega_o + \Delta\omega)|. \quad (2.13)$$

Given $H_o(\omega) = Ae^{j\phi}$, we have

$$\frac{\partial H_o(\omega)}{\partial \omega} = \left(\frac{\partial A}{\partial \omega} + Aj \frac{\partial \phi}{\partial \omega} \right) e^{j\phi} \quad (2.14)$$

As $|A(\omega_o)| = 1$ because of $1 + H_o(\omega_o) = 0$,

$$\left| \frac{\partial H_o(\omega)}{\partial \omega} \right|_{\omega_o} = \sqrt{\left(\frac{\partial A}{\partial \omega} \right)_{\omega_o}^2 + \left(\frac{\partial \phi}{\partial \omega} \right)_{\omega_o}^2} \quad (2.15)$$

Making use of the definition of the quality factor [96]

$$Q = \frac{\omega_o}{2} \sqrt{\left(\frac{\partial A}{\partial \omega} \right)_{\omega_o}^2 + \left(\frac{\partial \phi}{\partial \omega} \right)_{\omega_o}^2} \quad (2.16)$$

We arrive at

$$\left| \frac{\partial H_o(\omega)}{\partial \omega} \right|_{\omega_o} = \frac{2Q}{\omega_o}. \quad (2.17)$$

Substituting (2.17) into (2.13)

$$|I_o(\omega_o + \Delta\omega)| \approx \frac{|H_o(\omega_o + \Delta\omega)|}{\frac{2Q}{\omega_o} |\Delta\omega|} |I_{inj}(\omega_o + \Delta\omega)|. \quad (2.18)$$

Further from Fig. 2.5,

$$|I_o(\omega_o + \Delta\omega)| = |H_o(\omega_o + \Delta\omega)| |I_T(\omega_o + \Delta\omega)| \quad (2.19)$$

equating (2.18) and (2.19) yields

$$|\Delta\omega| = \frac{\omega_o}{2Q} \left| \frac{I_{inj}(\omega_o + \Delta\omega)}{I_T(\omega_o + \Delta\omega)} \right|. \quad (2.20)$$

It is of interest to comment above results :

1. When the injection is weak, i.e., $I_{inj} \ll I_o$, $I_o \approx I_T$ follows. As a result, (2.20) is the same as (2.5). Note that the latter was derived in a simple but efficient way in comparison with the approaches used in the previous published papers.
2. The preceding results are derived on the condition that the oscillator is locked to the injection signal. $|\Delta\omega|$ quantifies the maximum frequency deviation from ω_o upon which lock holds. It is therefore the lock range of the oscillator for given I_{inj} .
3. (2.20) is only valid when (2.10) holds. This typically occurs when the amplitude of the injection signal is small with respect to the I_o . This agrees well with the condition upon which (2.5) was derived.
4. Since $|\Delta\omega| = |\omega_{inj} - \omega_o|$, the lock range is only symmetrical if $I_T(\omega_o + \Delta\omega) = I_T(\omega_o - \Delta\omega)$, otherwise, asymmetric lock ranges exist. As the ratio of injection current to oscillator current increases, this condition will no longer be valid. This is especially true for low-Q oscillators, such as active-inductor oscillators [97]
5. A small Q will result in a large lock range. This echoes early findings on the relation between the impedance variation and Q of the LC tank in Fig. 2.6.

2.4 Lock Range and Tank Impedance Variation

It was pointed out earlier that the injection signal causes the variation of the impedance of the tank. This observation reveals that an intrinsic relation between the injection signal and the variation of the impedance of the resonant tank exists. To quantify the relation between the injection signal and the variation of the impedance of the tank, consider Fig. 2.7. In Fig. 2.7(a), a current I_{inj} of frequency $\omega_o + \Delta\omega$ is injected to node 2 of the oscillator. The oscillator is locked to the injection signal and oscillates at $\omega_o + \Delta\omega$. In Fig. 2.7(b), the effect of the injection signal on the oscillator is represented by the variation of the impedance of the LC tank (assume g_m -cell is constant). Note that Fig. 2.7(a) is a forced oscillator while

Fig. 2.7(b) is a free-running oscillator, in which the impact of the injection signal has been merged into the LC tank, denoting by δZ .

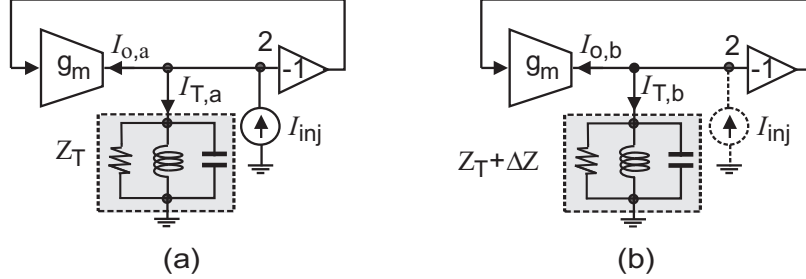


Figure 2.7: (a) Injection-locked oscillators. (b) Equivalent circuit of injection-locked oscillators. The dotted line represents the real injection signal, which has been merged into the variation of the LC tank.

Fig. 2.7(a) and Fig. 2.7(b) are said to be equivalent only if the voltages at node 2 of the two systems are identical. Since $V_{2,a} = Z_T(I_{inj} - I_{o,a})$ and $V_{2,b} = (Z_T + \Delta Z_T)(-I_{o,b})$ where Z_T is evaluated at $\omega_o + \Delta\omega$, from $V_{2,a} = V_{2,b}$, we have $I_{o,a} = I_{o,b} = I_o$. As a result,

$$\left| \frac{\Delta Z_T}{Z_T} \right| = \left| \frac{I_{inj}(\omega_o + \Delta\omega)}{I_T(\omega_o + \Delta\omega)} \right|. \quad (2.21)$$

(2.21) reveals that the effect of the injection signal can be quantified by the variation of the impedance of the tank. Substituting (2.21) into (2.20) yields

$$|\Delta\omega| = \frac{\omega_o}{2Q} \left| \frac{\Delta Z_T}{Z_T} \right|. \quad (2.22)$$

The preceding results are commented as :

1. For passive LC oscillators, since the quality factor of varactors is typically much higher(minimum Q is 80 in IBM CMRF8SF 130 nm technology) as compared with that of spiral inductors(maximum Q of differential inductor is 25 in IBM CMRF8SF 130 nm technology), the quality factor of passive LC tanks is dominated by that of the spiral inductors. Since passive LC tanks exhibit a large quality factor as compared

with that of active inductors, injection-locked passive LC oscillators have a small lock range while that of active-inductor oscillators have a large lock range.

2. The larger the normalized variation of the tank impedance induced by the injection signal, the larger the lock range. For spiral LC oscillators, since the effect of the injection signal on the capacitance of the varactors of these oscillators is small, $\Delta Z_T/Z_T$ is small as well. As a result, the lock range of these oscillators is small. This is in addition to the effect of the high quality factor of passive LC tanks, which also gives rise to a small lock range.
3. The inductance of active inductors varies with the injection signal especially when the injection signal is strong, $\Delta Z_T/Z_T$ of active inductors is large. As a result, active-inductor oscillators exhibit a large lock range. This is on top of the effect of the low quality factor of active inductors, which contributes to the large lock range of these oscillators.
4. The symmetry of the lock range is clearly determined by the symmetry of $|\Delta Z_T|$. Since active inductors are gyrator-based whose operating points are bias-dependent and injection signals affect the bias conditions, active-inductor oscillators will exhibit more asymmetrical lock ranges.
5. For passive LC oscillators, an injection signal will cause the capacitor of the varactors to change. For active-inductor oscillators, it is the inductance of the active inductors that will change with the injection signal.

Consider an LC tank with its C changed to $C + \Delta C$. Let $Z_{RL} = R||sL$, where "||" denotes parallel connection. Since $\hat{X}_c = 1/s(C + \Delta C) = X_c - \Delta X_c$, where $\Delta X_c = X_c(\Delta C/C)$ and $X_c = 1/sC$. The impedance of the tank is obtained from

$$\hat{Z}_T \approx Z_T \left[1 + \frac{Z_{RL}}{(Z_{RL} + X_c)X_c} \Delta X_c \right] \quad (2.23)$$

from which we arrive at

$$\Delta Z_T \approx \frac{Z_{RL} Z_T}{(Z_{RL} + X_c) X_c} \Delta X_c. \quad (2.24)$$

Note that first-order approximation was utilized in derivation of (2.23). In a similar manner, one can show that when L is changed to $L + \Delta L$, we have

$$\Delta Z_T \approx \frac{Z_{RC} Z_T}{(Z_{RC} + X_L) X_L} \Delta X_L \quad (2.25)$$

where $Z_{RC} = R || (1/sC)$, $X_L = sL$, and $\Delta X_L = X_L (\Delta L/L)$. The preceding results demonstrate that ΔZ_T is directly related to ΔC or ΔL .

2.5 Comparison of Injection-Locked LC Oscillators and Active Inductor Oscillators

In this section, it will be given that ΔC of injection-locked passive LC oscillators or ΔL of injection-locked active-inductor LC oscillators are indeed caused by the injection signal. Two oscillators are designed running at 2.4 GHz for the comparison purpose.

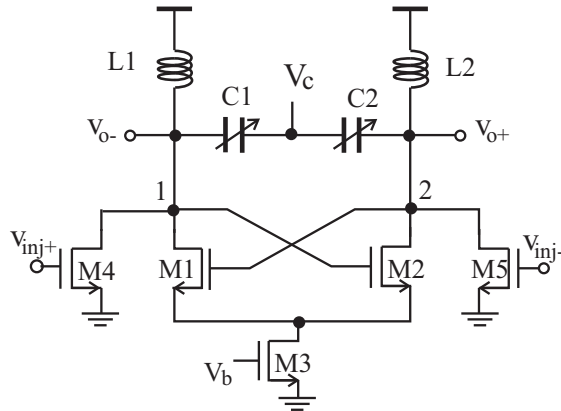


Figure 2.8: Injection-locked passive LC oscillator. C_1 and C_2 are accumulation MOS varactors. Circuit parameters : $W_{1,2} = 10\mu\text{m}$; $W_3 = 15\mu\text{m}$, $W_{4,5} = 1\mu\text{m}$, $V_c = 1.2\text{ V}$, $V_b = 0.66\text{ V}$, $I_{ds3} = 1.42\text{ mA}$.

Passive LC Oscillators

Consider the injection-locked passive LC oscillator in Fig. 2.8. Assume that the variation of the capacitance at nodes 1 and 2 is dominated by change of the capacitance of the varactors. Let the voltage across varactor C_1 be $V_{c1} = V - V_c + \Delta V$, where V is the dc voltage of node 1, and ΔV is the variation of the voltage across C_1 due to both injection and oscillation. Similarly, the voltage across C_2 is given by $V_{c2} = V - V_c - \Delta V$. The corresponding capacitances of varactors 1 and 2 are given by $C_1 = C + \Delta C_{osc} + \Delta C_{inj}$ and $C_2 = C - \Delta C_{osc} - \Delta C_{inj}$, where C is the capacitance of the varactors in the dc steady state, ΔC_{osc} is the oscillation-induced capacitance variation and ΔC_{inj} is the injection-induced capacitance variation. Assume $\Delta C_{osc}, \Delta C_{inj} \ll C$. The capacitance between nodes 1 and 2, denoted by C_{12} , is obtained from

$$C_{12} = \frac{C}{2} \left[1 - \frac{(\Delta C_{osc} + \Delta C_{inj})^2}{C^2} \right]. \quad (2.26)$$

From (2.26), it can be seen that the parentheses term indicates the variation of the overall capacitance due to the injection signal and oscillation. Since the capacitance looking into the negative resistor network and the capacitance of the injection transistors are rather constant, the total capacitance variation at nodes 1 and 2 is largely reduced, resulting in a narrow lock range.

Active Inductor Oscillators

Consider the injection-locked active inductor oscillator in Fig. 2.9 that employs Wu current-reuse active inductors reported and shown in the shade area. Wu active inductor can be represented by an RLC equivalent circuit with $C_p = C_{gs2}$, $R_p = 1/g_{m2}$, $R_s = (g_{o2} + g_{o3})/(g_{m1}g_{m2})$, and $L = C_{gs1}/(g_{m1}g_{m2})$, where g_m and g_o are the transconductance and output conductance of M1, respectively [92]. It is evident that L , R_p , and R_s of the active inductor can be varied by adjusting the current of M1 and M2.

Since the current of M2 is constant, it is reasonable to assume that g_{m2} is constant. As a result, $V_{g,2} = V_{s,1}$ are also constant. g_{m1} , however, varies with both oscillation and the

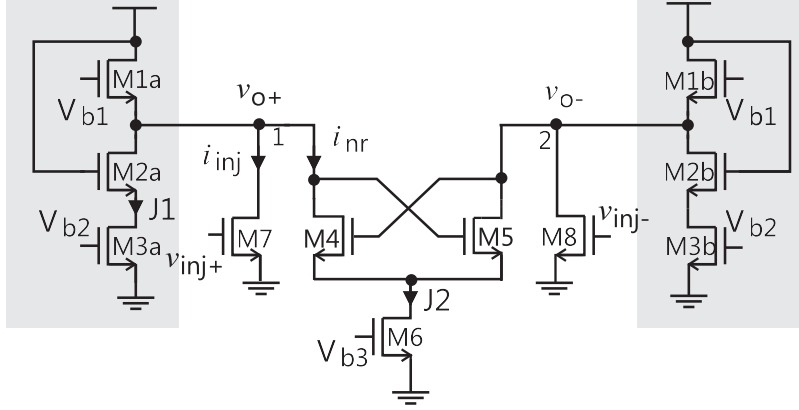


Figure 2.9: Schematic of injection-locked active-inductor VCO with Wu active inductors. Circuits parameters : $W_{1a,1b} = 40\mu\text{m}$, $W_{2a,2b} = 18.9\mu\text{m}$, $W_{3a,3b} = 4\mu\text{m}$, $W_{4,5} = 10\mu\text{m}$, $W_6 = 15\mu\text{m}$, $W_{7,8} = 1\mu\text{m}$, $V_{b1} = 0.34\text{ V}$, $V_{b2} = 0.48\text{ V}$, $V_{b3} = 0.7\text{ V}$, $I_{ds3} = 131\mu\text{A}$, $I_{ds6} = 1.42\text{ mA}$.

injection signal. Because $I_{D1} = J_1 + i_{inj} + i_{nr}$, where i_{nr} is the current of the negative resistor and i_{inj} is the injection current. Let $V_T = V_{TN} = |V_{TP}|$, we have

$$g_{m1} = g_{m1,DC} \left(1 + \frac{i_{inj}}{J_1} + \frac{i_{nr}}{J_1} \right) \quad (2.27)$$

where $g_{m1,DC} = 2J_1/(V_{SG1} - V_T)$ is the transconductance of M1 in the dc steady state. Let $i_{nr}^+ = I + \Delta I$ and $i_{nr}^- = I - \Delta I$ where $I = J_2/2$. The inductance of the active inductor is given by

$$L_1 = \frac{L_{DC}}{1 + \frac{I}{J_1}} \left(\frac{1}{1 + \frac{i_{inj} + \Delta I}{J_1 + I}} \right) \quad (2.28)$$

where $L_{DC} = C_{gs1}/(g_{m1,DC}g_{m2,DC})$. Similarly,

$$L_2 = \frac{L_{DC}}{1 + \frac{I}{J_1}} \left(\frac{1}{1 - \frac{i_{inj} + \Delta I}{J_1 + I}} \right) \quad (2.29)$$

Since active inductors L_1 and L_2 are connected in series, the inductance looking into nodes 1 and 2 is given by

$$L_{12} = \frac{2L_{DC}}{1 + \frac{I}{J_1}} \left[1 + \left(\frac{\Delta I + i_{inj}}{J_1 + I} \right)^2 \right]. \quad (2.30)$$

The variation of the overall inductance is due to the injection signal and the oscillation. Since i_{inj} directly affect L_{12} while in the injection-locked passive LC oscillator, the injection current impacts the capacitance of the varactors through the voltage of nodes 1 and 2, the injection signal will have a large impact on the inductance of the injection-locked active-inductor oscillator subsequently a large lock range.

The passive LC tank oscillator shown in Fig. 2.8 and the active-inductor LC oscillator shown in Fig. 2.9 are utilized to validate the results derived earlier. Simulations are done in Cadence SpectreRF. The incident power of injection signal for both oscillators is a -18 dBm, the ratio of $I_{inj}/I_o = 0.05$ 2.40205 GHz sinusoid with phase noise -126 dBc/Hz at 1 MHz frequency offset.

Fig. 2.10 plots the phase noise of the passive LC oscillator. The phase noise of the oscillator without injection-locking is -102 dBc/Hz at 1 MHz frequency offset and -124 dBc/Hz when locked.

Fig. 2.11 plots the phase noise of the active-inductor oscillator, simulated in Cadence Spectre. The phase noise of the oscillator without the injection-locking reference is -70 dBc/Hz at 1 MHz frequency offset and is reduced to -118 dBc/Hz when locked.

To provide a fair comparison of the lock range, the negative resistors of the oscillators are biased at the same level. The swing of the output voltage of the oscillators is also made identical. Fig. 2.12 is dependence of the lock range on the injection signal. It is observed that the lock range is directly proportional to the injection signal. This agrees well with the theoretical results. Also observed is that the lock range of injection-locked active inductor oscillator is much larger as compared with that of the injection-locked passive LC oscillator. To demonstrate the larger lock range of the active inductor oscillator is not only due to the

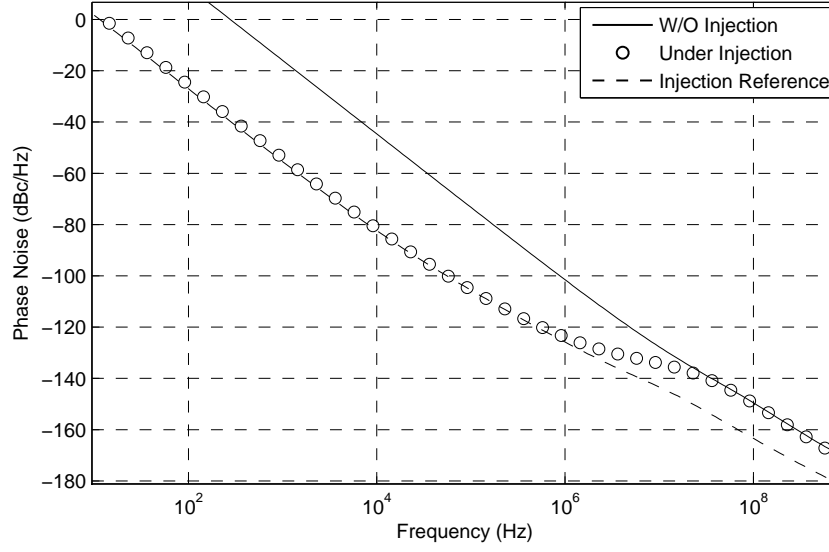


Figure 2.10: Simulated phase noise of passive LC oscillator $I_{inj}/I_o = 0.05$.

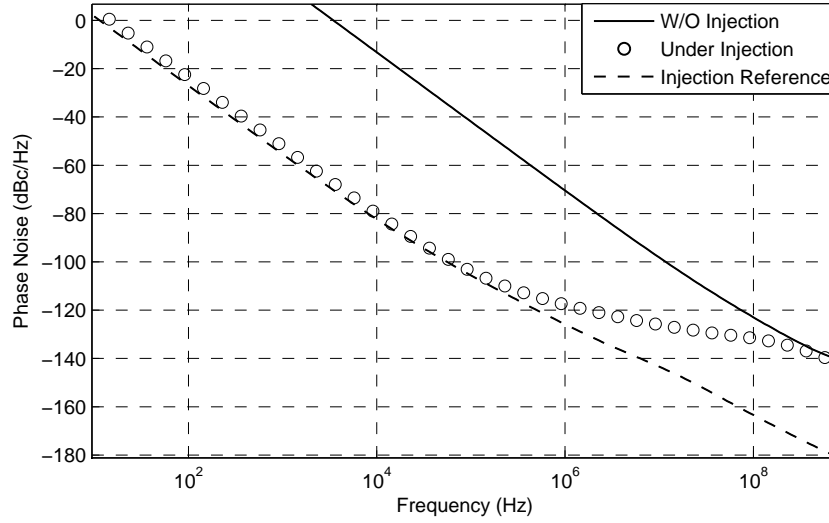


Figure 2.11: Simulated phase noise of active-inductor LC oscillator $I_{inj}/I_o = 0.05$.

low quality factor but injection-induced impedance variation, the re-sized passive oscillator by inserting series resistors to lower Q-factor, which is in the comparable level to the active inductor oscillator, is simulated. The lock range of passive one is still less than the active one.

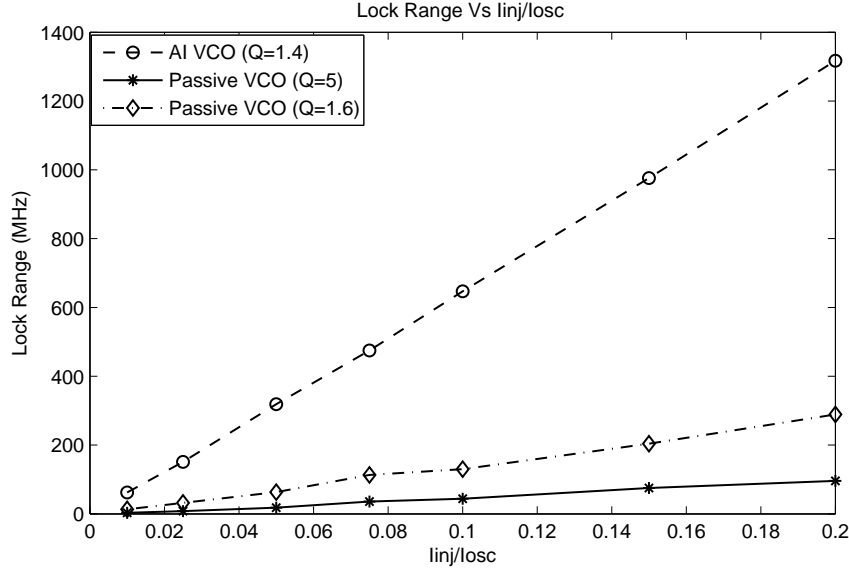


Figure 2.12: Simulated lock range.

Active inductor oscillators are low- Q systems. When injection ratio increases, not only lock range will increase, the asymmetry of the lock range of these oscillators will also becomes more prominent. This is evident in Fig. 2.13 where the positive and negative lock ranges of the active inductor oscillator investigated in this paper are plotted. The asymmetry of the lock range is evident.

2.6 Summary

In this chapter, an in-depth investigation of the lock range of injection-locked LC oscillators using a control system approach has been presented. The intrinsic relation between the lock range of these oscillators and the injection-induced variation of the impedance of the LC tank of these oscillators has been explored. The large lock range of injection-locked active-inductor oscillators is attributed to both the low quality factor and the large injection-induced variation of the inductance of active inductors.

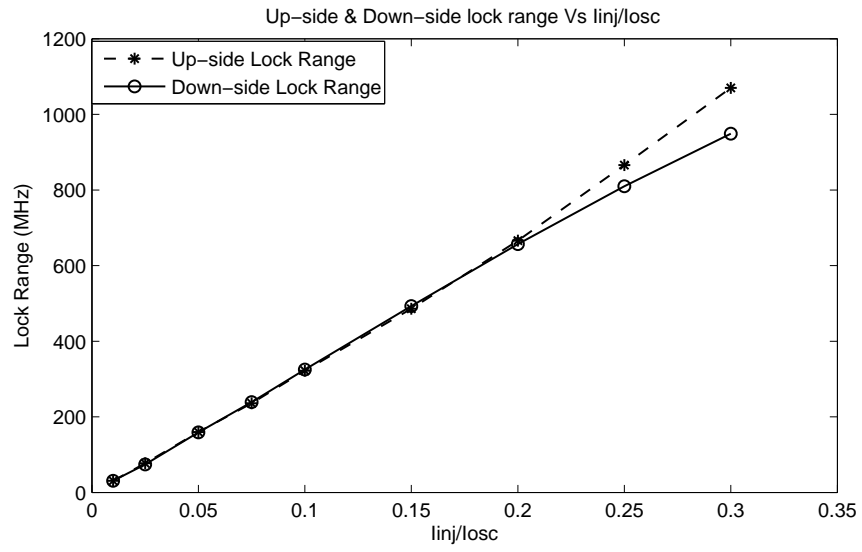


Figure 2.13: Asymmetry of the lock range of injection-locked active-inductor oscillator.

Chapter 3

Multiple Multi-Tone Injection-Locked Oscillators

In general, Volterra series can be used to analyze a non-linear behaviour. In this chapter, an approach similar to Volterra series is employed to explore the non-harmonic injection-locked oscillators. The oscillators can be analyzed by applying a set of linear circuits, having the same topology and element values but different inputs. The analytical study of the lock range is also given in detail. The remaining of the chapter is organized as the follows: Section 3.1 presents a simplified mode of injection-locked non-harmonic oscillators. Section 3.2 investigates the single-tone and multi-tone injections for non-harmonic oscillators. Section 3.3 gives an analysis for harmonic injection-locked oscillators with multiple injections. Section 3.4 examines the non-harmonic injection-locked oscillators with multiple injections. Section 3.5 shows the study of lock range of non-harmonic oscillators with multiple single-tone injections. A relaxation oscillator is given as an example in Section 3.6. A study of lock range of non-harmonic oscillators with multiple multi-tone injections is presented in Section 3.7, followed by simulations in Section 3.8. A summary is provided in Section 3.9.

3.1 Representation of Non-Harmonic Oscillators

The waveform of the output voltage of LC oscillators is sinusoidal whereas that of non-harmonic oscillators is typically square-like. To capture the essence of non-harmonic oscillators, assume that the output of these oscillators is a purely square wave such that it

can be represented by a Fourier series with the fundamental frequency $\omega_o = 2\pi/T_o$ where T_o is the frequency of the oscillator. If the waveform of the output of the oscillator is shown in Fig.3.1(a), then its spectrum will only contain the fundamental and odd harmonics. Since the spectrum of the output of the oscillator only consists of a train of impulses at $\omega_o, 3\omega_o, 5\omega_o, \dots$, the oscillator can be considered as the assembly of ideal harmonic oscillators whose frequency spectrum only contains single tones at $\omega_o, 3\omega_o, 5\omega_o, \dots$. When the noise and loss of the non-harmonic oscillator are considered, the square waveform of the non-harmonic oscillator is replaced with those shown in Fig.3.1(b). In this case, the impulses are replaced with skirts.

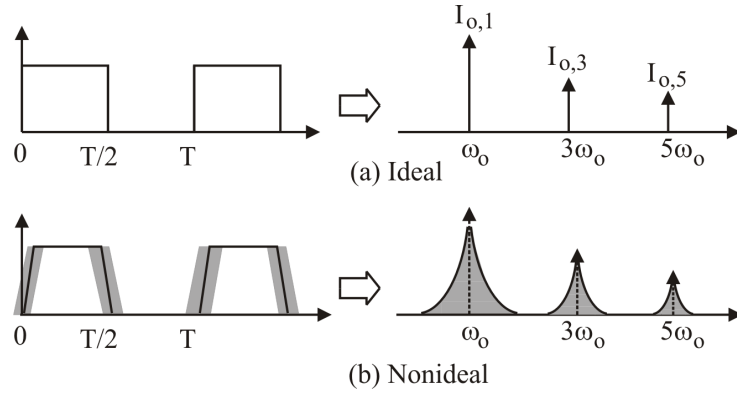


Figure 3.1: Waveform and spectrum of non-harmonic oscillators.

Neglect the loss and noise of the oscillator, the output of the non-harmonic oscillator can be represented by

$$I_o = \sum_{n=1,3,\dots}^{\infty} I_{o,n}(n\omega_o)\delta(\omega - n\omega_o) \quad (3.1)$$

where $\delta(\cdot)$ is the discrete-time impulse also known as the unit impulse [98]. Note that $\delta(\omega - \omega_o) = 1$ if $\omega = \omega_o$ and 0 otherwise. The use of the discrete-time impulse enables us to conveniently capture the multi-tone characteristics of the spectrum of $I_o(t)$.

3.2 Representation of Injection-Locked Non-harmonic Oscillators

3.2.1 Single-Tone Injection

When a single-tone signal $I_{inj}(t)$, such as a sinusoid, is injected to a non-harmonic oscillator with its frequency within the lock range of the non-harmonic oscillator for the given injection strength, the frequency of the oscillator will be shifted from its free-running frequency ω_o to that of $I_{inj}(t)$ and the oscillator is locked to I_{inj} . If $I_{inj}(t)$ is a single-tone at ω_{inj} , it can be represented by

$$I_{inj}(t) = I_{inj}e^{j\omega_{inj}t}. \quad (3.2)$$

When the non-harmonic oscillator is locked to $I_{inj}(t)$, the frequency of the harmonic oscillators representing the non-harmonic oscillator are changed to ω_{inj} , $3\omega_{inj}$, ..., accordingly. This observation reveals that the single-tone input of the non-harmonic oscillator $I_{inj}(t)$ will affect the input of the representing harmonic oscillators. The injection-locked non-harmonic oscillator with a single-tone injection at ω_{inj} can therefore be equivalent to a set of injection-locked harmonic oscillators with injections at ω_{inj} , $3\omega_{inj}$, ..., as shown in Fig. 3.2.

The preceding representation of an injection-locked non-harmonic oscillator with a set of injection-locked harmonic oscillators bears a strong resemblance to Volterra series analysis of nonlinear circuits. It is well understood that a nonlinear time-invariant circuit can be represented by a set of linear time-invariant circuits called Volterra circuits that have the same topology but distinct inputs determined by the nonlinearities of the circuits [99, 100]. Similarly, it was demonstrated in [101, 102, 103] that a periodically nonlinear time-varying circuit can be represented by a set of periodically linear time-varying circuits of the same topology but different inputs set by the nonlinearities of the circuits. In both cases, methods for analysis of linear systems such as Fourier transform can be applied to

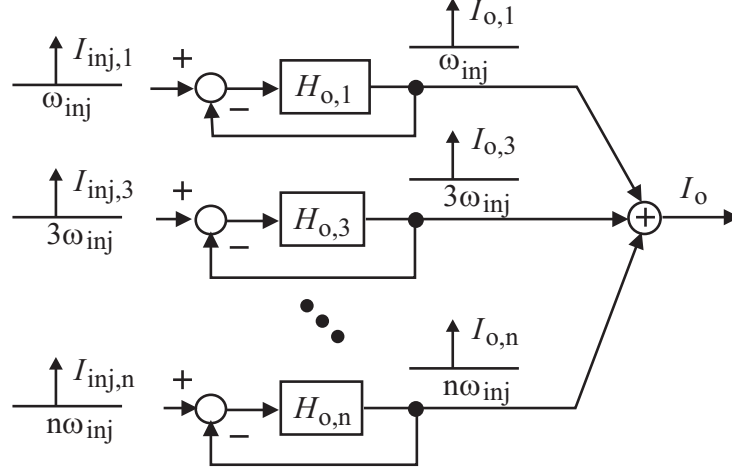


Figure 3.2: Representation of injection-locked non-harmonic oscillators with a single-tone injection.

analyze nonlinear circuits. As a result, non-harmonic oscillators fall into the category of periodically linear time-varying circuits.

3.2.2 Multi-Tone Injection

If the injection signal $I_{inj}(t)$ is a multi-tone signal, such as a square wave of frequency ω_{inj} , it will contain multiple frequency components at frequencies $n\omega_{inj}$, $n = 1, 3, \dots$ (Assume $I_{inj}(t)$ has the waveform shown in Fig. 3.1). In this case, $I_{inj}(t)$ can be represented by

$$I_{inj}(t) = \sum_{n=1,3,\dots}^{\infty} I_{inj,n} e^{jn\omega_{inj}t}. \quad (3.3)$$

The impact of $I_{inj}(t)$ on the oscillator can be analyzed by evaluating the effect of each frequency component of $I_{inj}(t)$ individually in a similar way as that with a single-tone injection. This approach clearly is valid because although injection-locking is a nonlinear process, in the vicinity of the lock state the injection-locked non-harmonic oscillator can well be represented by a linear system.

A short discussion associated with new definition of quality factor of harmonic oscillators and some of related equations, which will be used for the lock range study of multiple multi-tone injection-locked oscillators, are given as below. The definition of the quality factor of harmonic oscillators, (2.16), is extended to n th-order harmonic oscillators representing the non-harmonic oscillator.

$$Q_n = \frac{n\omega_o}{2} \sqrt{\left(\frac{\partial A_n}{\partial \omega}\right)_{n\omega_o}^2 + \left(\frac{\partial \phi_n}{\partial \omega}\right)_{n\omega_o}^2}. \quad (3.4)$$

Assume that the injection signal $I_{inj}(t)$ causes the frequency of a non-harmonic oscillator to shift from its natural frequency ω_o to $\omega_o + \Delta\omega$ in the lock state with $\Delta\omega_o \ll \omega_o$ typically. If the injection is a single-tone at ω_{inj} , we will have $\omega_{inj} = \omega_o + \Delta\omega$ in the lock state. If the injection signal is a multi-tone, such as a square wave, with its fundamental frequency ω_{inj} , $\omega_{inj} = \omega_o + \Delta\omega$ will hold in the lock state. Using the first-order Taylor series approximation, we obtain the loop gain of n th harmonic oscillator

$$H_{o,n}[n(\omega_o + \Delta\omega_o)] \approx H_{o,n}(n\omega_o) + \left(\frac{\partial H_{o,n}}{\partial \omega}\right)_{n\omega_o} (n\Delta\omega). \quad (3.5)$$

Let $H_{o,n} = A_n e^{j\phi_n}$. Because

$$\begin{aligned} \frac{\partial H_{o,n}}{\partial \omega} &= e^{j\phi_n} \left[\frac{\partial A_n}{\partial \omega} + jA_n \frac{\partial \phi_n}{\partial \omega} \right] \\ \frac{\partial H_{o,n}^*}{\partial \omega} &= e^{-j\phi_n} \left[\frac{\partial A_n}{\partial \omega} - jA_n \frac{\partial \phi_n}{\partial \omega} \right] \end{aligned} \quad (3.6)$$

where the superscript $*$ denotes the complex conjugate operator, we have

$$\frac{\partial H_{o,n}}{\partial \omega} \frac{\partial H_{o,n}^*}{\partial \omega} = \left(\frac{\partial A_n}{\partial \omega}\right)^2 + A_n^2 \left(\frac{\partial \phi_n}{\partial \omega}\right)^2. \quad (3.7)$$

Evaluating (3.7) at $\omega = n\omega_o$ and noting that each harmonic oscillator satisfies Barhausen criteria

$$1 + H_{o,n}(n\omega_o) = 0 \quad n = 1, 3, 5, \dots \quad (3.8)$$

where $H_{o,n}(n\omega_o)$ is the loop gain of n th harmonic oscillator, we arrive at

$$\left(\frac{\partial H_{o,n}}{\partial \omega} \frac{\partial H_{o,n}^*}{\partial \omega} \right)_{n\omega_o} = \left(\frac{\partial A_n}{\partial \omega} \right)_{n\omega_o}^2 + \left(\frac{\partial \phi_n}{\partial \omega} \right)_{n\omega_o}^2 \quad (3.9)$$

Making use of (3.4), (3.9) can be written as

$$\left(\frac{\partial H_{o,n}}{\partial \omega} \frac{\partial H_{o,n}^*}{\partial \omega} \right)_{n\omega_o} = \left(\frac{2Q_n}{n\omega_o} \right)^2. \quad (3.10)$$

(3.10) will be utilized in analysis of the lock range of non-harmonic oscillators.

3.3 Harmonic Oscillators with Multiple Injections

Consider the LC oscillator in Fig. 3.3 where I_{inj1} and I_{inj2} represent the two currents injected at two different nodes of the oscillator.

The injection-locked oscillator in the vicinity of the lock state is represented by the block diagram shown in Fig. 3.3 with g_{m1} and g_{m2} the transconductance of M1 and M2, respectively. Write KCL at the output nodes of the transconductors

$$\begin{aligned} I_{o2} &= [(I_{o1} - I_{inj1}) Z_{L1}] g_{m2} \\ I_{o1} &= -[(I_{o2} - I_{inj2}) Z_{L2}] g_{m1} \end{aligned} \quad (3.11)$$

where $Z_{L1} = sL_1 || \frac{1}{sC_1}$ and $Z_{L2} = sL_2 || \frac{1}{sC_2}$. Let $H_{o1} = g_{m2}Z_{L1}$ and $H_{o2} = g_{m1}Z_{L2}$, (3.11) can be written as

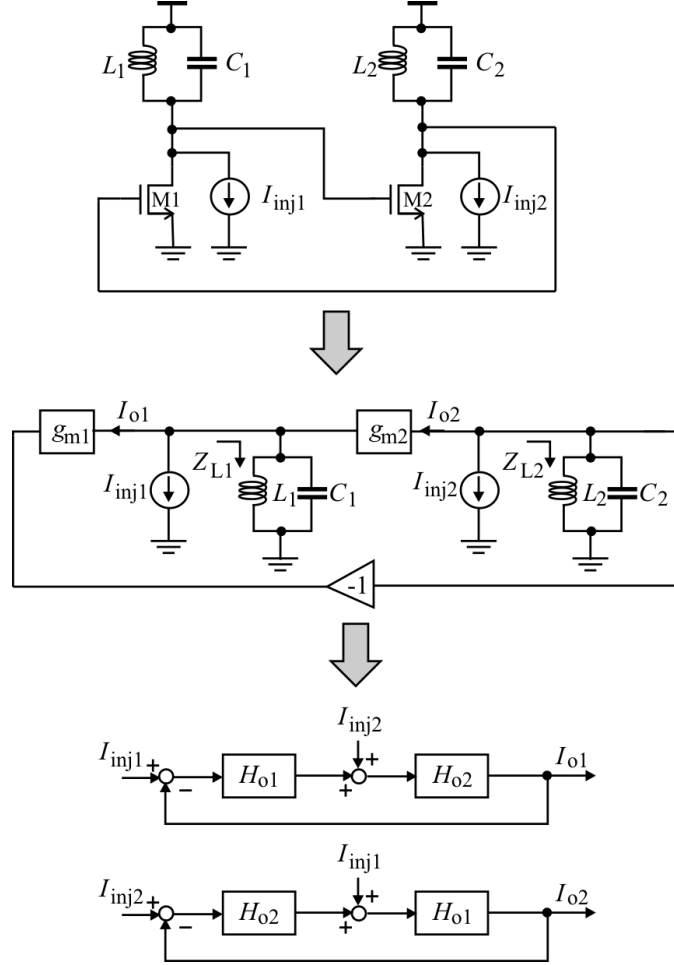


Figure 3.3: Injection-locked harmonic oscillators with multiple injections.

$$\begin{aligned}
 I_{o1} &= \left(\frac{H_{o1}H_{o2}}{1 + H_{o1}H_{o2}} \right) I_{inj1} + \left(\frac{H_{o2}}{1 + H_{o1}H_{o2}} \right) I_{inj2}. \\
 I_{o2} &= \left(\frac{H_{o1}H_{o2}}{1 + H_{o1}H_{o2}} \right) I_{inj2} + \left(\frac{H_{o1}}{1 + H_{o1}H_{o2}} \right) I_{inj1}.
 \end{aligned} \tag{3.12}$$

It is evident from (3.12) that the injection-locked oscillator can be represented by the linear control system shown in Fig. 3.3. Eq.(3.11) can also be written as

$$\begin{aligned}
I_{o2} &= H_{o1}I_{o1} - H_{o1}I_{inj1}, \\
I_{o1} &= -H_{o2}I_{o2} + H_{o2}I_{inj2}.
\end{aligned}
\tag{3.13}$$

When the injection signals are absent, we have $I_{o1} = -H_{o2}I_{o2}$ and $I_{o2} = H_{o1}I_{o1}$. Since I_{o1} and I_{o2} are out of phase with the same magnitude, we conclude

$$\begin{aligned}
H_{o1} &= e^{j\pi} \\
H_{o2} &= -e^{j\pi}.
\end{aligned}
\tag{3.14}$$

The results given in (3.14) are important as they will be used to quantify the contribution of the double injections to the lock range of the non-harmonic oscillators.

3.4 Non-Harmonic Oscillators with Multiple Injections

Let us extend the control system presentation of harmonic oscillators with multiple injections presented earlier to non-harmonic oscillators with multiple injections. Consider a non-harmonic oscillator with injections I_{inj1} and I_{inj2} . In the vicinity of the lock state, the injection-locked oscillator is represented by the block diagram shown in Fig. 3.4.

$I_{inj1}(t)$ affects the oscillator through $I_{inj1,1}$ at ω_{inj} , $I_{inj1,3}$ at $3\omega_{inj}$... and $I_{inj2}(t)$ affects the oscillator through $I_{inj2,1}$ at ω_{inj} , $I_{inj2,3}$ at $3\omega_{inj}$, ... The output of the non-harmonic oscillator in the lock state is obtained from

$$\begin{aligned}
I_o &= \left[\frac{H_{o1}I_{inj1,1}}{1 + H_{o1}} + \frac{H_{o1}I_{inj2,1}}{H_{o1,1}(1 + H_{o1})} \right] \delta(\omega - \omega_{inj}) \\
&+ \left[\frac{H_{o3}I_{inj1,3}}{1 + H_{o3}} + \frac{H_{o3}I_{inj2,3}}{H_{o1,3}(1 + H_{o3})} \right] \delta(\omega - 3\omega_{inj}) \\
&+ \dots
\end{aligned}
\tag{3.15}$$

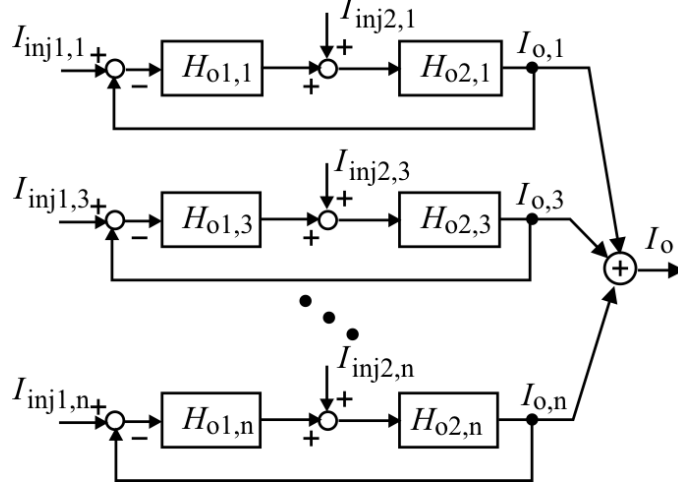


Figure 3.4: Representation of injection-locked non-harmonic oscillators with multiple single-tone injections.

where $H_{o1} = H_{o1,1}H_{o2,1}$ and $H_{o3} = H_{o1,3}H_{o2,3}$ are the loop gain of the first-order and 3rd-order harmonic oscillators, respectively.

3.5 Lock Range of Non-Harmonic Oscillators with Multiple Single-Tone Injections

Assume that single-tone injection signals $I_{inj1}(t)$ and $I_{inj2}(t)$ of the same frequency ω_{inj} cause the frequency of a non-harmonic oscillator to shift from its natural frequency ω_o to $\omega_{inj} = \omega_o + \Delta\omega$ in the lock state with $\Delta\omega_o \ll \omega_o$. Using the first-order Taylor series approximation given in (3.5) and noting that $H_{o,n}(n\omega_o) = -1$, $H_{o,n}(n\omega_o) \gg \left[\frac{\partial H_{o,n}}{\partial \omega} \right]_{n\omega_o} (n\Delta\omega)$, and $1 + H_{o,n}(\omega_o + n\Delta\omega) \approx 0$, the output of the oscillator in the lock state can be obtained from (3.15)

$$\begin{aligned}
I_o \approx & \left[\frac{-I_{inj1,1}}{\left(\frac{\partial H_{o1}}{\partial \omega}\right)_{\omega_o} \Delta \omega} + \frac{1}{H_{o1,1}} \frac{-I_{inj2,1}}{\left(\frac{\partial H_{o1}}{\partial \omega}\right)_{\omega_o} \Delta \omega} \right] \delta(\omega - \omega_{inj}) \\
& + \left[\frac{-I_{inj1,3}}{\left(\frac{\partial H_{o3}}{\partial \omega}\right)_{3\omega_o} 3\Delta \omega} + \frac{1}{H_{o1,3}} \frac{-I_{inj2,3}}{\left(\frac{\partial H_{o3}}{\partial \omega}\right)_{3\omega_o} 3\Delta \omega} \right] \delta(\omega - 3\omega_{inj}) \\
& + \dots
\end{aligned} \tag{3.16}$$

It follows from (3.16) that

$$\begin{aligned}
I_o^* \approx & \left[\frac{-I_{inj1,1}^*}{\left(\frac{\partial H_{o1}^*}{\partial \omega}\right)_{\omega_o} \Delta \omega} + \frac{1}{H_{o1,1}^*} \frac{-I_{inj2,1}^*}{\left(\frac{\partial H_{o1}^*}{\partial \omega}\right)_{\omega_o} \Delta \omega} \right] \delta(\omega - \omega_{inj}) \\
& + \left[\frac{-I_{inj1,3}^*}{\left(\frac{\partial H_{o3}^*}{\partial \omega}\right)_{3\omega_o} (3\Delta \omega)} + \frac{1}{H_{o1,3}^*} \frac{-I_{inj2,3}^*}{\left(\frac{\partial H_{o3}^*}{\partial \omega}\right)_{3\omega_o} (3\Delta \omega)} \right] \delta(\omega - 3\omega_{inj}) \\
& + \dots
\end{aligned} \tag{3.17}$$

Because $\delta(\omega - \omega_m)\delta(\omega - \omega_n) = 1$ if $m = n$ and 0 otherwise, we have

$$\begin{aligned}
I_{o1} I_{o1}^* \approx & \left[\frac{|I_{inj1,1}|^2}{\left(\frac{\partial H_{o1}}{\partial \omega} \frac{\partial H_{o1}^*}{\partial \omega}\right)_{\omega_o} (\Delta \omega)^2} + \frac{1}{|H_{o1,1}|^2} \frac{|I_{inj2,1}|^2}{\left(\frac{\partial H_{o1}}{\partial \omega} \frac{\partial H_{o1}^*}{\partial \omega}\right)_{\omega_o} (\Delta \omega)^2} \right. \\
& + \frac{I_{inj1,1} I_{inj2,1}^*}{H_{o1,1}^* \left(\frac{\partial H_{o1}}{\partial \omega} \frac{\partial H_{o1}^*}{\partial \omega}\right)_{\omega_o} (\Delta \omega)^2} + \frac{1}{H_{o1,1}} \frac{I_{inj1,1}^* I_{inj2,1}}{\left(\frac{\partial H_{o1}}{\partial \omega} \frac{\partial H_{o1}^*}{\partial \omega}\right)_{\omega_o} (\Delta \omega)^2} \left. \right] \delta(\omega - \omega_{inj}) \\
& + \left[\frac{|I_{inj1,3}|^2}{\left(\frac{\partial H_{o3}}{\partial \omega} \frac{\partial H_{o3}^*}{\partial \omega}\right)_{3\omega_o} (3\Delta \omega)^2} + \frac{1}{|H_{o1,3}|^2} \frac{|I_{inj2,3}|^2}{\left(\frac{\partial H_{o3}}{\partial \omega} \frac{\partial H_{o3}^*}{\partial \omega}\right)_{3\omega_o} (3\Delta \omega)^2} \right. \\
& + \frac{I_{inj1,3} I_{inj2,3}^*}{H_{o1,3}^* \left(\frac{\partial H_{o3}}{\partial \omega} \frac{\partial H_{o3}^*}{\partial \omega}\right)_{3\omega_o} (3\Delta \omega)^2} + \frac{1}{H_{o1,3}} \frac{I_{inj1,3}^* I_{inj2,3}}{\left(\frac{\partial H_{o3}}{\partial \omega} \frac{\partial H_{o3}^*}{\partial \omega}\right)_{3\omega_o} (3\Delta \omega)^2} \left. \right] \delta(\omega - 3\omega_{inj}) \\
& + \dots
\end{aligned} \tag{3.18}$$

Utilizing (3.10), we can write (3.18) as

$$\begin{aligned}
I_o I_o^* &= \left(\frac{\omega_o}{2Q_1} \right)^2 \frac{1}{(\Delta\omega)^2} \left[|I_{inj1,1}|^2 + \frac{|I_{inj2,1}|^2}{|H_{o1,1}|^2} + \frac{I_{inj1,1} I_{inj2,1}^*}{H_{o1,1}^*} + \frac{I_{inj1,1}^* I_{inj2,1}}{H_{o1,1}} \right] \delta(\omega - \omega_{inj}) \\
&+ \left(\frac{\omega_o}{2Q_3} \right)^2 \frac{1}{(\Delta\omega)^2} \left[|I_{inj1,3}|^2 + \frac{|I_{inj2,3}|^2}{|H_{o1,3}|^2} + \frac{I_{inj1,3} I_{inj2,3}^*}{H_{o1,3}^*} + \frac{I_{inj1,3}^* I_{inj2,3}}{H_{o1,3}} \right] \delta(\omega - 3\omega_{inj}) \\
&+ \dots
\end{aligned} \tag{3.19}$$

Matching the terms in (3.19) that have the same frequency yields

$$\begin{aligned}
I_{o,1}^2 &= \left(\frac{\omega_o}{2Q_1} \right)^2 \frac{1}{(\Delta\omega)^2} \left[|I_{inj1,1}|^2 + \frac{|I_{inj2,1}|^2}{|H_{o1,1}|^2} + \frac{I_{inj1,1} I_{inj2,1}^*}{H_{o1,1}^*} + \frac{I_{inj1,1}^* I_{inj2,1}}{H_{o1,1}} \right] \\
I_{o,3}^2 &= \left(\frac{\omega_o}{2Q_3} \right)^2 \frac{1}{(\Delta\omega)^2} \left[|I_{inj1,3}|^2 + \frac{|I_{inj2,3}|^2}{|H_{o1,3}|^2} + \frac{I_{inj1,3} I_{inj2,3}^*}{H_{o1,3}^*} + \frac{I_{inj1,3}^* I_{inj2,3}}{H_{o1,3}} \right] \\
&\dots
\end{aligned} \tag{3.20}$$

Let $I_{inj1}(t)$ and $I_{inj2}(t)$ have the same amplitude I_{inj} but different phases

$$I_{inj1}(t) = I_{inj} e^{j(\omega_{inj}t + \phi_1)}, \tag{3.21}$$

$$I_{inj2}(t) = I_{inj} e^{j(\omega_{inj}t + \phi_2)}. \tag{3.22}$$

Also, let the magnitude of the injection signals of first-order, 3rd-order, and n th-order harmonic oscillators due to $I_{inj1}(t)$ be denoted by $I_{inj,1}$, $I_{inj,3}$, ..., $I_{inj,n}$, respectively. Similar notations apply to $I_{inj2}(t)$ as well. Further, let $\Delta\phi = \phi_1 - \phi_2$ be the phase difference between $I_{inj1}(t)$ and $I_{inj2}(t)$. Since (3.14) holds for harmonic oscillators with double injections, it will also hold for n th-order harmonic oscillator

$$\begin{aligned}
H_{o1,n} &= e^{j\pi} \\
H_{o2,n} &= -e^{j\pi}
\end{aligned} \tag{3.23}$$

$n = 1, 3, 5, \dots$ (3.20) becomes

$$\begin{aligned}
I_{o,1}^2 &= \left(\frac{\omega_o}{2Q_1} \right)^2 \frac{I_{inj,1}^2}{(\Delta\omega)^2} [2 + e^{j(\pi+\Delta\phi)} + e^{-j(\pi+\Delta\phi)}] \\
I_{o,3}^2 &= \left(\frac{\omega_o}{2Q_3} \right)^2 \frac{I_{inj,3}^2}{(\Delta\omega)^2} [2 + e^{j(\pi+\Delta\phi)} + e^{-j(\pi+\Delta\phi)}] \\
&\dots
\end{aligned} \tag{3.24}$$

Since $I_{o,1}, I_{o,3}, \dots$ are the magnitude of the fundamental and harmonics of $I_o(t)$, respectively.

As

$$I_o^2 = I_{o,1}^2 + I_{o,3}^2 + I_{o,5}^2 + \dots \tag{3.25}$$

is the output power of the oscillator. The summation of the expressions in (3.24) yields

$$(\Delta\omega)^2 = \frac{\left[\left(\frac{\omega_o}{2Q_1} \right)^2 \frac{I_{inj,1}^2}{I_o^2} + \left(\frac{\omega_o}{2Q_3} \right)^2 \frac{I_{inj,3}^2}{I_o^2} + \dots \right]}{[2 + e^{j(\pi+\Delta\phi)} + e^{-j(\pi+\Delta\phi)}]}. \tag{3.26}$$

Define

$$|\Delta\omega_n| = \left(\frac{\omega_o}{2Q_n} \right) \frac{I_{inj,n}}{I_o}. \tag{3.27}$$

The denominator of (3.27) is the total output current of the oscillator. (3.27) thus quantifies the contribution of n th-order harmonic oscillator $I_{inj,n}$ to the overall lock range of the non-harmonic oscillator. (3.26) can be written as

$$|\Delta\omega| = \alpha_d \sqrt{\sum_{n=1,3,\dots}^{\infty} (\Delta\omega_n)^2} \tag{3.28}$$

where

$$\alpha_d = \sqrt{2 + e^{j(\pi+\Delta\phi)} + e^{-j(\pi+\Delta\phi)}}. \quad (3.29)$$

Since

$$|\Delta\omega_s| = \sqrt{\sum_{n=1,3,\dots}^{\infty} (\Delta\omega_n)^2} \quad (3.30)$$

is the lock range of the non-harmonic oscillator with a single injection, the lock range of the oscillator with double injections given by (3.28) can be written as

$$|\Delta\omega_d| = \alpha_d |\Delta\omega_s|. \quad (3.31)$$

The preceding developments are summarised as:

1. (3.25) quantifies the output power of the non-harmonic oscillator (assume 1 Ω load).

This can be best explained using Fourier series representation of periodic functions.

Consider a periodic function $i(t)$ and represent it with the Fourier series $i(t) = \sum_{n=1,3,\dots}^{\infty} I_n \cos(n\omega t)$

where $\omega = 2\pi/T$ and T is the period of $i(t)$. The average power of $i(t)$, denoted P_{avg} , is obtained from [104]

$$P_{avg} = \sqrt{\frac{1}{T} \int_0^T i^2(t) dt} = \sqrt{\sum_{n=1,3,\dots}^{\infty} \left(\frac{I_n}{\sqrt{2}} \right)^2} \quad (3.32)$$

Clearly the average power of $i(t)$ is the sum of that of each harmonic of $i(t)$. Since $i(t)$ contains an infinite number of frequency components, its power is distributed across the entire frequency spectrum. The actual profile of the distribution of the power of $i(t)$ is determined by the characteristics of $i(t)$. For example, if $i(t)$ is a sinusoid of

frequency ω_o , its power will only be concentrated at ω_o . If $i(t)$ is a square wave, its power will mainly be concentrated at the fundamental and low-order harmonics.

2. $\Delta\omega_n$ is the lock range of n th-harmonic oscillator with a single injection. (3.30) thus quantifies the relation between the lock range of the harmonic oscillators and that of the non-harmonic oscillators. For example, if the harmonic oscillator is injection-locked to an external signal, only fundamental frequency will be taken into account. And therefore (3.30) is simplified to (3.33)

$$|\Delta\omega_s| = \left(\frac{\omega_o}{2Q} \right) \left| \frac{I_{inj}}{I_o} \right| \quad (3.33)$$

same as (2.5).

3. α_d quantifies the effect of the phase relation between the two injection signals on the lock range of the non-harmonic oscillator. Table 3.1 tabulates α_d for several special cases. It is evident that the lock range of non-harmonic oscillators with multiple single-tone injections will be large than that with a single-tone injection, if the phases of these injection signals are properly chosen. This finding can also be applied to injection-locked harmonic oscillators.

Table 3.1: Lock Range Coefficient α_d

Phase difference ($\Delta\phi$)	Lock range coeff. (α_d)
$\Delta\phi = 0$	$\alpha_d = 0$
$\Delta\phi = \pi/4$	$\alpha_d = \sqrt{2(1 - \cos\frac{\pi}{4})}$
$\Delta\phi = \pi/2$	$\alpha_d = \sqrt{2}$
$\Delta\phi = 3\pi/4$	$\alpha_d = \sqrt{2(1 + \cos\frac{\pi}{4})}$
$\Delta\phi = \pi$	$\alpha_d = 2$

3.6 Simulations

Relaxation oscillators are widely encountered in passive wireless microsystems owing to their low sensitivity to supply voltage fluctuation as the charging and discharging currents are well defined by the current references, and their low sensitivity to temperature variation as its performance is largely determined by passive components and digital components. The harsh nonlinear elements of relaxation oscillators are comparators and the switching instants of the comparator are known a priori in the steady state, the comparators, therefore, can be modelled as periodically-operated switches that connect the output of the comparators to either V_{DD} or ground. If no other nonlinearities are considered, relaxation oscillators can be modelled as periodically time-varying linear circuits. If nonlinearities other than comparators are also considered, relaxation oscillators are periodically time-varying nonlinear circuits. An injection-locked dual-comparator relaxation oscillator shown in Fig. 3.5, operating in the sub-threshold mode with 13 MHz frequency for power saving, to verify all the findings presented earlier and later. The oscillator is designed in IBM 130 nm 1.2V CMOS technology and analyzed using Cadence Spectre.

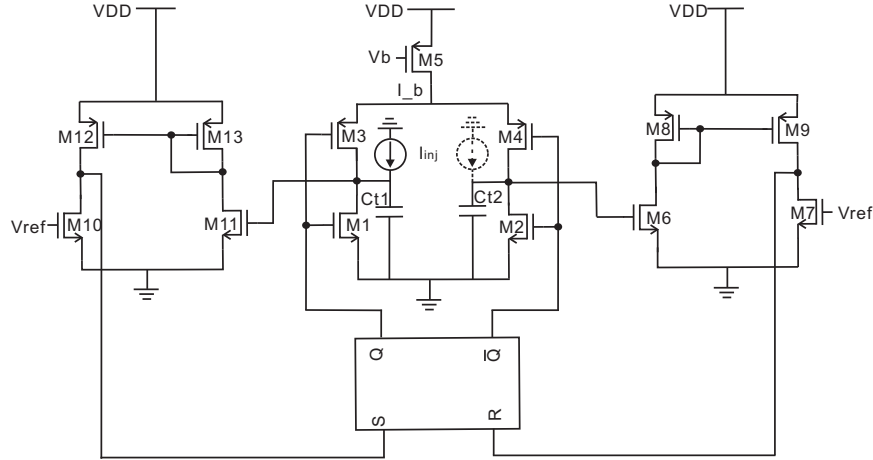


Figure 3.5: Schematic of relaxation oscillator with injection-locking. Circuit parameters: $W_{1,2,6,7,10,11} = 0.5\mu\text{m}$, $W_{3,4} = 1.2\mu\text{m}$, $W_{8,9,12,13} = 1.25\mu\text{m}$, $W_5 = 2\mu\text{m}$, Supply voltage $V_{DD} = 0.9\text{V}$, $V_{ref} = 0.31\text{ V}$, $I_b = 253\text{ nA}$, $V_b = 0.62\text{ V}$

Fig. 3.6 shows free-running frequency of the relaxation oscillator without disturbance of the injecting signal.

The spectrum of the oscillator is used to determine whether the oscillator is locked or not. The locking of an oscillator could be *fast beat* (ω_{inj} is far away from ω_o and outside the lock range), *quasi lock* (ω_{inj} is very close to ω_o but outside the lock range), and *lock* (ω_{inj} is in the lock range) [53]. The spectrum of the oscillator in fast beat consists of a train of tones separated with a large frequency spacing while that of the oscillator in quasi lock is made of a train of tones separated with a small frequency spacing. When the oscillator is locked to the injection signal, only tones at the frequencies of the injection signal will exist [105, 106, 107, 108]. One therefore can determine whether a lock state is established or not by examining the spectrum of the oscillator. Figs.3.7, 3.8, and 3.9 show the spectrum of the relaxation oscillator (taken at the output of the comparators) in fast beat, quasi-lock, and lock states with a square-wave injection of injection ratio 0.1. Injection ratio is defined as the ratio of the injection current I_{inj} to the tail current I_b .

Double injection is obtained by injecting a current source from the drain of M1 to the drain of M2. In this case, the two injection currents have the same frequency and amplitude but a 180 degree phase difference. Fig. 3.10 presents the dependence of the lock range on the strength of the injection signal with a sinusoidal injection and double sinusoidal injections whose phase difference is 180 phase. It is seen that increasing injection signal strength yields a larger lock range. Also observed is that for the same injection strength, the lock range of the oscillator with double sinusoidal injections is twice that with a single sinusoidal injection. This agrees well with the theoretical findings presented in Table 3.1.

3.7 Lock Range of Non-Harmonic Oscillators with Multiple Multi-Tone Injections

If injection signals are multi-tones, the output of the oscillator can be obtained by considering the effect of each of the harmonic components of the injection signals. Consider a non-harmonic oscillator with two multi-tone injection signals $I_{inj1}(t)$ and $I_{inj2}(t)$, such as

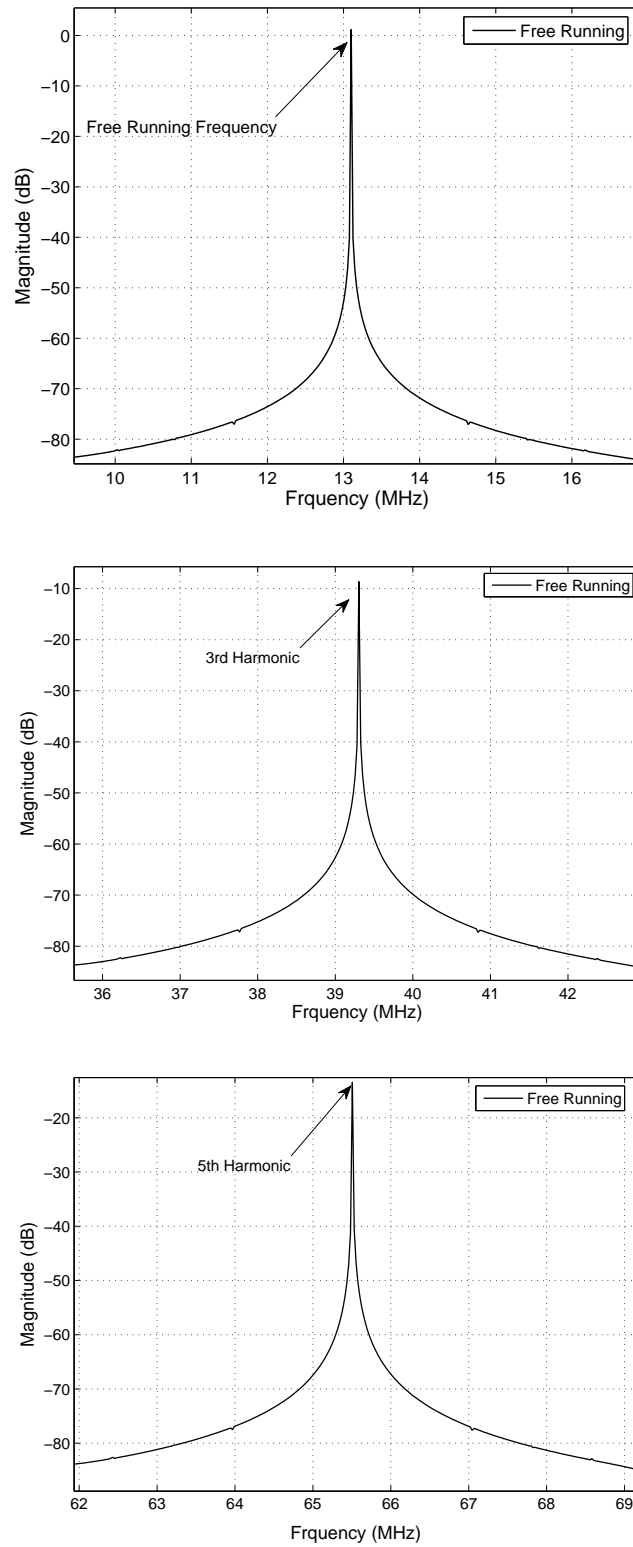


Figure 3.6: Simulated spectrum of relaxation oscillator without injection. Top - Fundamental. Middle : 3rd harmonic. Bottom : 5th harmonic.

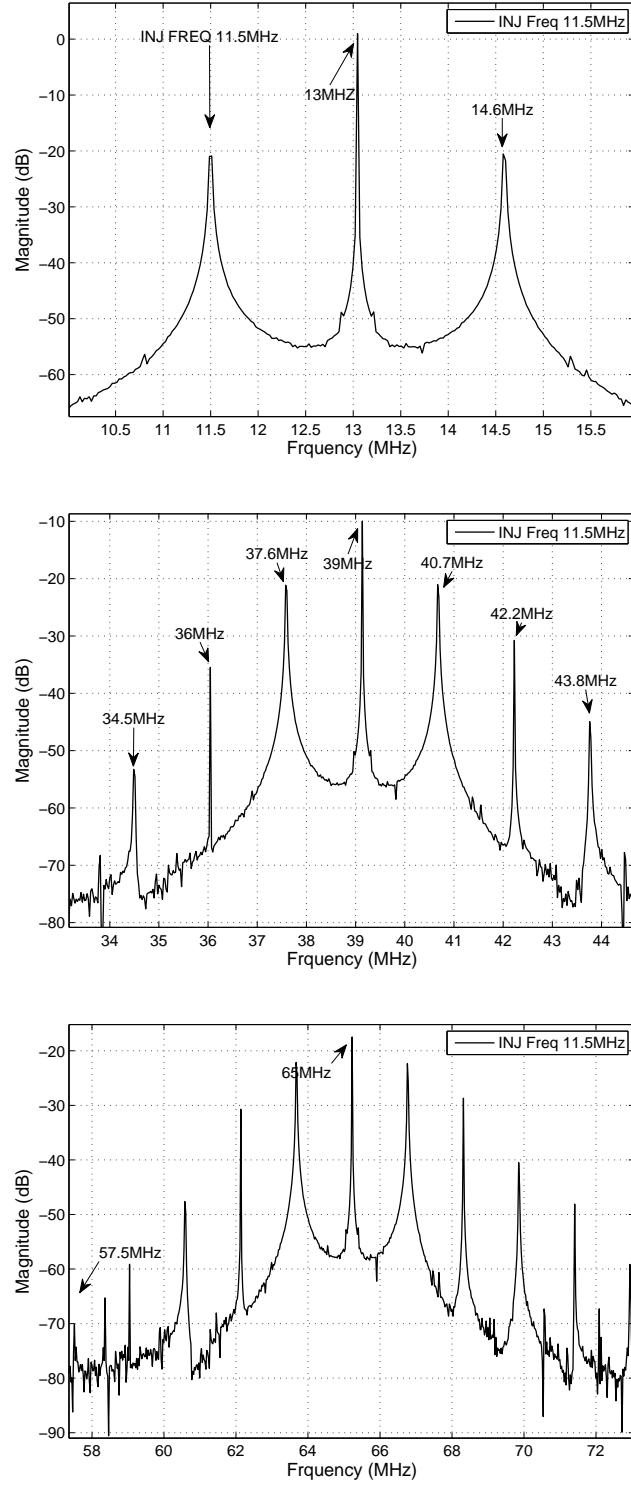


Figure 3.7: Simulated spectrum of relaxation oscillator in fast beat. Top - Fundamental. Middle : 3rd harmonic. Bottom : 5th harmonic.

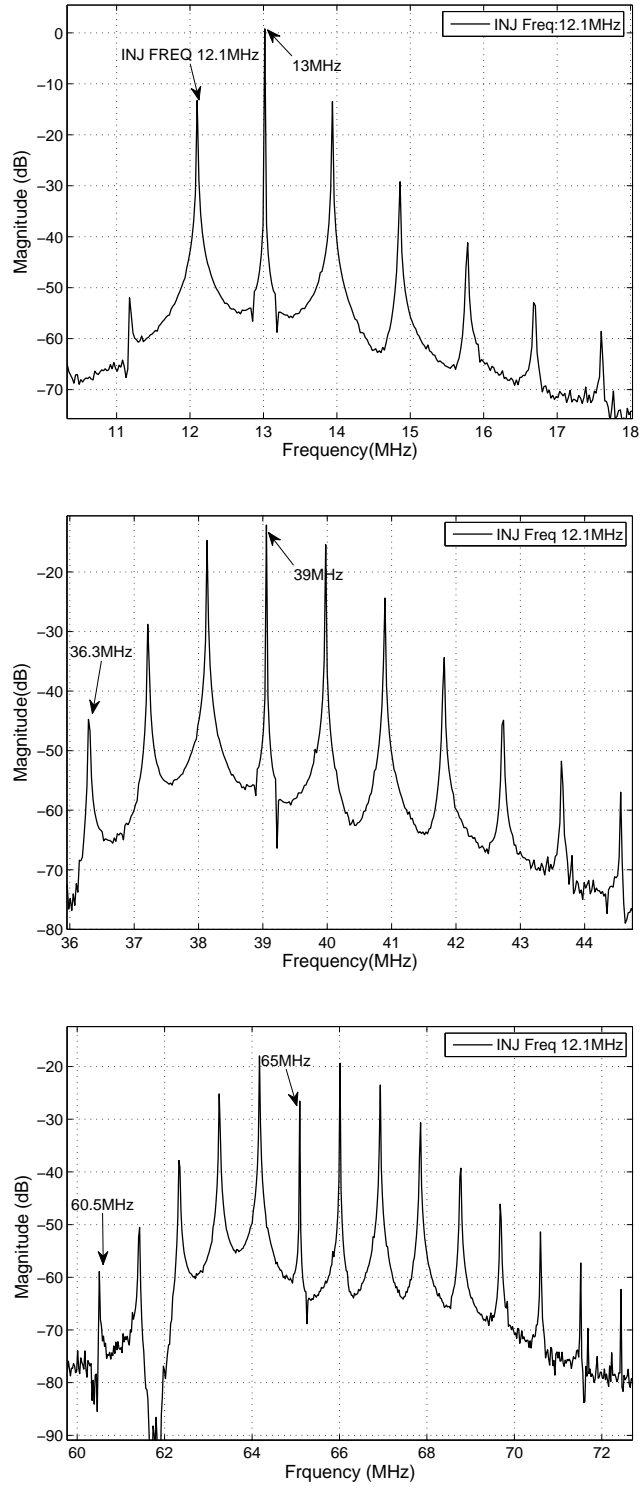


Figure 3.8: Simulated spectrum of relaxation oscillator in quasi-lock. Top - Fundamental. Middle : 3rd harmonic. Bottom : 5th harmonic.

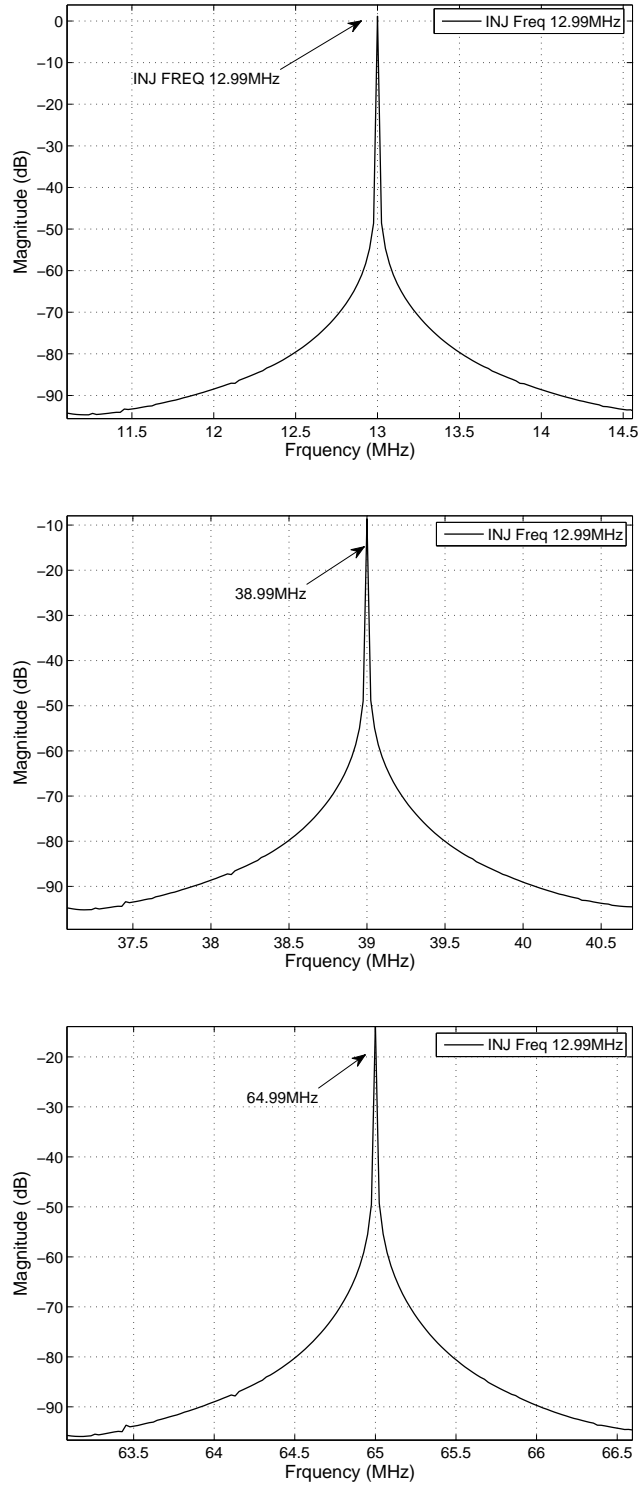


Figure 3.9: Simulated spectrum of relaxation oscillator in lock state. Top - Fundamental. Middle : 3rd harmonic. Bottom : 5th harmonic.

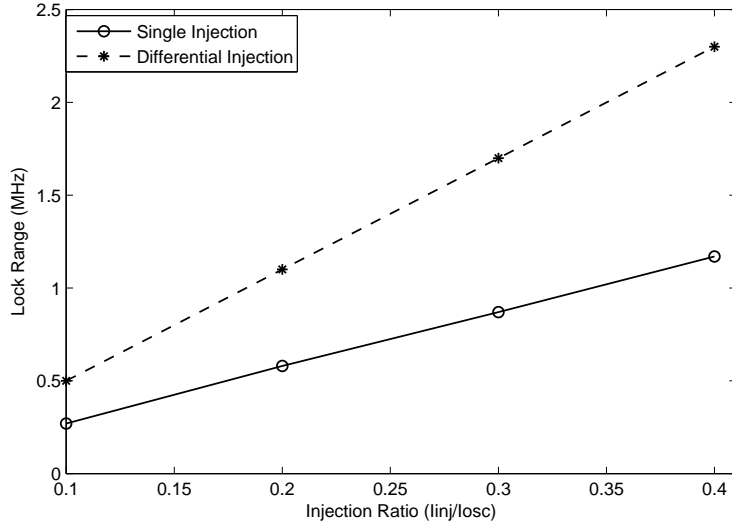


Figure 3.10: Simulated dependence of the lock range of relaxation oscillator with a sinusoidal injection and double sinusoidal injections whose phase difference is 180 degree on injection strength.

square waves. $I_{inj1}(t)$ contains single-tone frequency components $I_{inj1,1}$, $I_{inj1,3}$, ... $I_{inj1,n}$ at ω_{inj} , $3\omega_{inj}$, ..., $n\omega_{inj}$, respectively. The same for $I_{inj2}(t)$ as well. The effect of $I_{inj1,1}$ can be analyzed in a similar way as that for injection-locked non-harmonic oscillators with a single-tone injection presented earlier. Specifically, assume that the injection signals of first-order, 3rd-order, ..., n th-order harmonic oscillators due to $I_{inj1,1}$ are $I_{inj1,11}$, $I_{inj1,31}$, ..., $I_{inj1,n1}$, respectively. Similar notations are used for I_{inj2} , as shown graphically in Fig. 3.11.

The input of first-order harmonic oscillator due to $I_{inj1}(t)$ is obtained by summing up $I_{inj1,11}$, $I_{inj1,13}$, ..., and $I_{inj1,1n}$. It is evident that

$$\begin{aligned}
I_o \approx & \left[\frac{-(I_{inj1,11} + I_{inj1,13} + \dots)}{\left(\frac{\partial H_{o1}}{\partial \omega}\right)_{\omega_o} \Delta \omega} + \frac{1}{H_{o1,1}} \frac{-(I_{inj2,11} + I_{inj2,13} + \dots)}{\left(\frac{\partial H_{o1}}{\partial \omega}\right)_{\omega_o} \Delta \omega} \right] \delta(\omega - \omega_{inj}) \\
& + \left[\frac{-(I_{inj1,31} + I_{inj1,33} + \dots)}{\left(\frac{\partial H_{o3}}{\partial \omega}\right)_{3\omega_o} 3\Delta \omega} + \frac{1}{H_{o1,3}} \frac{-(I_{inj2,31} + I_{inj2,33} + \dots)}{\left(\frac{\partial H_{o3}}{\partial \omega}\right)_{3\omega_o} 3\Delta \omega} \right] \delta(\omega - 3\omega_{inj}) \quad (3.34) \\
& + \dots
\end{aligned}$$

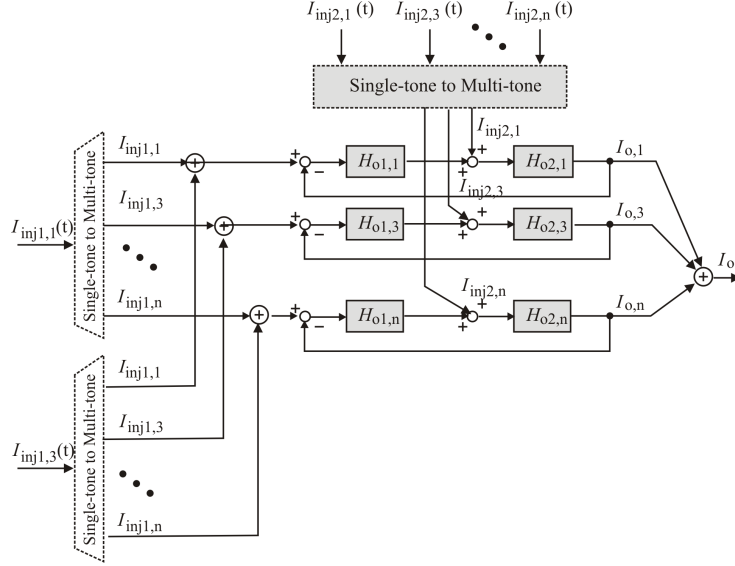


Figure 3.11: Representation of injection-locked non-harmonic oscillators with multiple multi-tone injections.

It follows from (3.34) that

$$\begin{aligned}
 I_o^* \approx & \left[\frac{-(I_{inj1,11}^* + I_{inj1,13}^* + \dots)}{\left(\frac{\partial H_{o1}^*}{\partial \omega}\right)_{\omega_o} \Delta \omega} + \frac{1}{H_{o1,1}^*} \frac{-(I_{inj2,11}^* + I_{inj2,13}^* + \dots)}{\left(\frac{\partial H_{o1}^*}{\partial \omega}\right)_{\omega_o} \Delta \omega} \right] \delta(\omega - \omega_{inj}) \\
 & + \left[\frac{-(I_{inj1,31}^* + I_{inj1,33}^* + \dots)}{\left(\frac{\partial H_{o3}^*}{\partial \omega}\right)_{3\omega_o} 3\Delta \omega} + \frac{1}{H_{o1,3}^*} \frac{-(I_{inj2,31}^* + I_{inj2,33}^* + \dots)}{\left(\frac{\partial H_{o3}^*}{\partial \omega}\right)_{3\omega_o} 3\Delta \omega} \right] \delta(\omega - 3\omega_{inj}) \quad (3.35) \\
 & + \dots
 \end{aligned}$$

As a result,

$$\begin{aligned}
I_o I_o^* \approx & \left[\frac{(I_{inj1,11} + I_{inj1,13} + \dots)(I_{inj1,11}^* + I_{inj1,13}^* + \dots)}{\left(\frac{\partial H_{o1}}{\partial \omega} \frac{\partial H_{o1}^*}{\partial \omega}\right)_{\omega_o} (\Delta\omega)^2} \right. \\
& + \frac{(I_{inj1,11} + I_{inj1,13} + \dots)(I_{inj2,11}^* + I_{inj2,13}^* + \dots)}{H_{o1,1}^* \left(\frac{\partial H_{o1}}{\partial \omega} \frac{\partial H_{o1}^*}{\partial \omega}\right)_{\omega_o} (\Delta\omega)^2} \\
& + \frac{(I_{inj1,11} + I_{inj1,13} + \dots)(I_{inj2,11}^* + I_{inj2,13}^* + \dots)}{H_{o1,1} \left(\frac{\partial H_{o1}}{\partial \omega} \frac{\partial H_{o1}^*}{\partial \omega}\right)_{\omega_o} (\Delta\omega)^2} \\
& \left. + \frac{(I_{inj2,11} + I_{inj2,13} + \dots)(I_{inj2,11}^* + I_{inj2,13}^* + \dots)}{|H_{o1,1}|^2 \left(\frac{\partial H_{o1}}{\partial \omega} \frac{\partial H_{o1}^*}{\partial \omega}\right)_{\omega_o} (\Delta\omega)^2} \right] \delta(\omega - w_{inj}) \\
& + \left[\frac{(I_{inj1,31} + I_{inj1,33} + \dots)(I_{inj1,31}^* + I_{inj1,33}^* + \dots)}{\left(\frac{\partial H_{o3}}{\partial \omega} \frac{\partial H_{o3}^*}{\partial \omega}\right)_{\omega_o} (3\Delta\omega)^2} \right. \\
& + \frac{(I_{inj1,31} + I_{inj1,33} + \dots)(I_{inj2,31}^* + I_{inj2,33}^* + \dots)}{H_{o3,1}^* \left(\frac{\partial H_{o3}}{\partial \omega} \frac{\partial H_{o3}^*}{\partial \omega}\right)_{\omega_o} (3\Delta\omega)^2} \\
& + \frac{(I_{inj1,31} + I_{inj1,33} + \dots)(I_{inj2,31}^* + I_{inj2,33}^* + \dots)}{H_{o3,1} \left(\frac{\partial H_{o3}}{\partial \omega} \frac{\partial H_{o3}^*}{\partial \omega}\right)_{\omega_o} (3\Delta\omega)^2} \\
& \left. + \frac{(I_{inj2,31} + I_{inj2,33} + \dots)(I_{inj2,31}^* + I_{inj2,33}^* + \dots)}{|H_{o3,1}|^2 \left(\frac{\partial H_{o3}}{\partial \omega} \frac{\partial H_{o3}^*}{\partial \omega}\right)_{\omega_o} (3\Delta\omega)^2} \right] \delta(\omega - 3w_{inj}) \\
& + \dots
\end{aligned} \tag{3.36}$$

Matching the components that have the same frequency in (3.36) yields

$$\begin{aligned}
I_{o1}^2 &= \left(\frac{\omega_o}{2Q_1} \right)^2 \frac{1}{(\Delta\omega)^2} \left[(I_{inj1,11} + I_{inj1,13} + \dots)(I_{inj1,11}^* + I_{inj1,13}^* + \dots) \right. \\
&\quad + \frac{(I_{inj1,11} + I_{inj1,13} + \dots)(I_{inj2,11}^* + I_{inj2,13}^* + \dots)}{H_{o1,1}^*} \\
&\quad + \frac{(I_{inj1,11} + I_{inj1,13} + \dots)(I_{inj2,11}^* + I_{inj2,13}^* + \dots)}{H_{o1,1}} \\
&\quad \left. + \frac{(I_{inj2,11} + I_{inj2,13} + \dots)(I_{inj2,11}^* + I_{inj2,13}^* + \dots)}{|H_{o1,1}|^2} \right] \\
&= \left(\frac{\omega_o}{2Q_1} \right)^2 \frac{1}{(\Delta\omega)^2} \hat{I}_{o1}^2,
\end{aligned} \tag{3.37}$$

where \hat{I}_{o1}^2 represents the sum of the terms in the bracket in (3.37). Similarly, we have

$$I_{on}^2 = \left(\frac{\omega_o}{2Q_n} \right)^2 \frac{1}{(\Delta\omega)^2} \hat{I}_{on}^2, \quad n = 1, 3, 5, \dots \tag{3.38}$$

The summation of the expressions in (3.38) with utilization of (3.25) yields

$$(\Delta\omega)^2 = \left(\frac{\omega_o}{2Q_1} \right)^2 \frac{\hat{I}_{o1}^2}{I_o^2} + \left(\frac{\omega_o}{2Q_3} \right)^2 \frac{\hat{I}_{o3}^2}{I_o^2} + \dots \tag{3.39}$$

Define

$$(\Delta\omega_n)^2 = \left(\frac{\omega_o}{2Q_1} \right)^2 \frac{\hat{I}_{on}^2}{I_o^2}, \tag{3.40}$$

we arrive at

$$|\Delta\omega| = \sqrt{\sum_{n=1,3,5,\dots}^{\infty} (\Delta\omega_n)^2} \tag{3.41}$$

Since the square-wave injections are represented by a set of harmonic single-tone injections, (3.20) will also hold. The lock range of non-harmonic oscillators with double square-wave injections is maximized if the phase difference between the injection signals is 180 degree. A direct comparison of (3.20) with (3.37) reveals that I_{on}^2 , $n = 1, 3, 5, \dots$ of the non-harmonic oscillator with multiple multi-tone injections is larger than that of the non-harmonic oscillator with multiple single-tone injections if the phases of these injections are properly chosen. The large lock range is due to the effect of the harmonic tones of the injection signals.

3.8 Simulations

Using same relaxation oscillator in Fig. 3.5 to validate the theoretical analysis. Three different injection signals, namely (i) sinusoidal currents (single-tone injection) $I_{inj} = A \sin(\omega_{inj}t)$, (ii) dual-sinusoidal currents (dual-tone injections) $I_{inj}(t) = I_1 \sin(\omega_{inj}t) + I_3 \sin(3\omega_{inj}t)$ with $I_3 = I_1/3$, and (iii) square-wave currents (multi-tone injections) are used to lock the oscillators. Both single injection and double injections are considered. Fig. 3.12 investigates the dependence of the lock range of the relaxation oscillator on the strength of the injection signal with a single square-wave injection and with double square-wave injections whose phase difference is 180 degree. It is seen that the lock range of the oscillator with double square-wave injections is twice that with a single square-wave injection. This observation also agrees well with the theoretical findings presented earlier.

To investigate whether the dependence of the lock of the relaxation oscillator on injection strength is linear or nonlinear over a large range of injection ratio, the lock range of the relaxation oscillator with a differential square-wave injection is obtained over the injection ratio 0.1~0.5 and the results are plotted in Fig. 3.13. It is observed that the dependence of the lock range on the injection ratio is approximately linear over the investigated injection ratio range. It is well known that LC-oscillators typically exhibit a nonlinear lock range characteristics when injection is strong [109, 64]. The nonlinear characteristics of the lock range of these oscillators is largely determined by the frequency selectivity or equivalently the

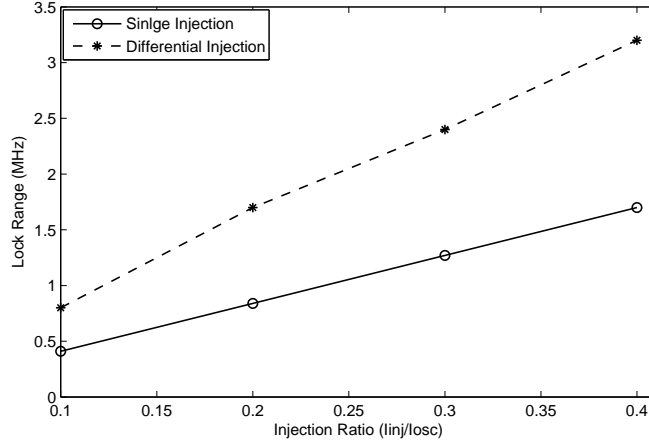


Figure 3.12: Simulated dependence of the lock range of relaxation oscillator with a single square-wave injection and with double square-wave injections whose phase difference is 180 degree on injection strength.

quality factor of the LC tank [110]. It is also known that non-harmonic oscillators typically exhibit a lower quality factor, reflected by their inferior phase noise performance as compared with harmonic oscillators. The low quality factor might contribute to the large lock range subsequently better lock range linearity. This is observed in injection-locked active-inductor LC oscillators, which have a larger lock range as compared with their spiral LC counterparts. The sub-threshold operation of the relaxation oscillator investigated might also contribute to the large lock range and better lock range linearity as the current of MOSFETs is an exponential rather than a second-order function of the over-drive voltage.

Fig. 3.14 compares the lock range of the oscillator with a single sinusoidal injection, a single square-wave injection, and a single dual-tone (two-sinusoids) injection. It is seen that the oscillator with a square-wave injection yields the largest lock range whereas that with a single sinusoidal injection has the smallest lock range. These results echo the theoretical findings given earlier well.

Fig. 3.15 plots the dependence of the lock range of the oscillator with double square-wave injections on the phase difference of the injection signals. It is evident that the lock range increases monotonically with the phase difference and reaches its maximum when the phase difference is 180 degree. This agrees well with the theoretical results derived earlier.

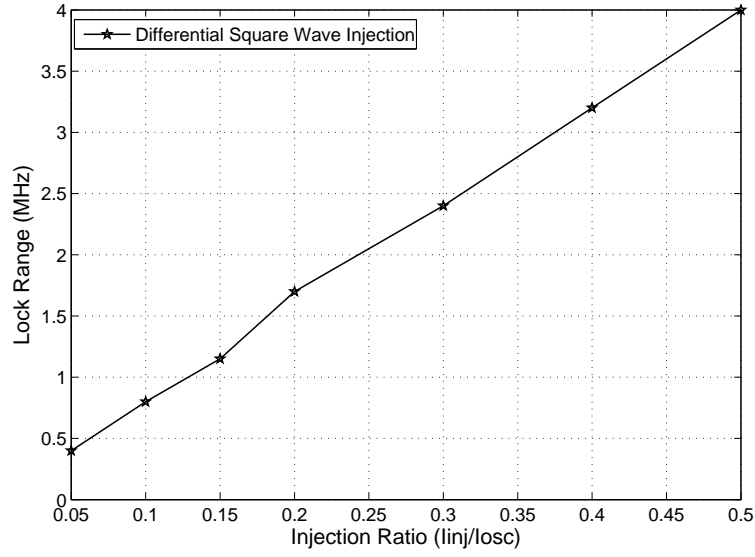


Figure 3.13: Simulated dependence of the lock range of relaxation oscillator with differential square-wave injection on injection strength.

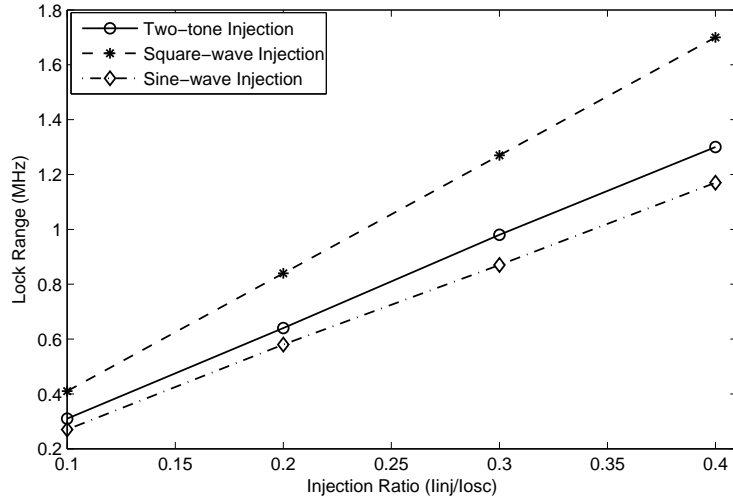


Figure 3.14: Simulated dependence of the lock range of relaxation oscillator with a single sinusoidal injection, a single square-wave injection, and a single dual-tone (two-sinusoids) injection on injection strength.

Fig. 3.16 compares the lock range of the relaxation oscillator with a two-tone sinusoidal injection and double two-tone injections whose phase difference is 180 degree. It is seen that for the same injection strength, the lock range of the oscillator with double two-

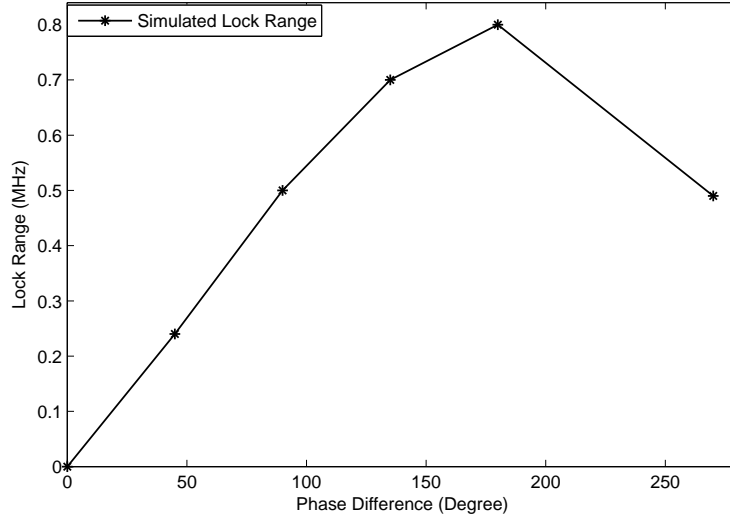


Figure 3.15: Simulated dependence of the lock range of relaxation oscillator with double square-wave injections on the phase difference of the injection signals. The injection ratio is 0.1.

tone injections is twice that with a single two-tone injection. This observation agrees with the theoretical findings presented earlier.

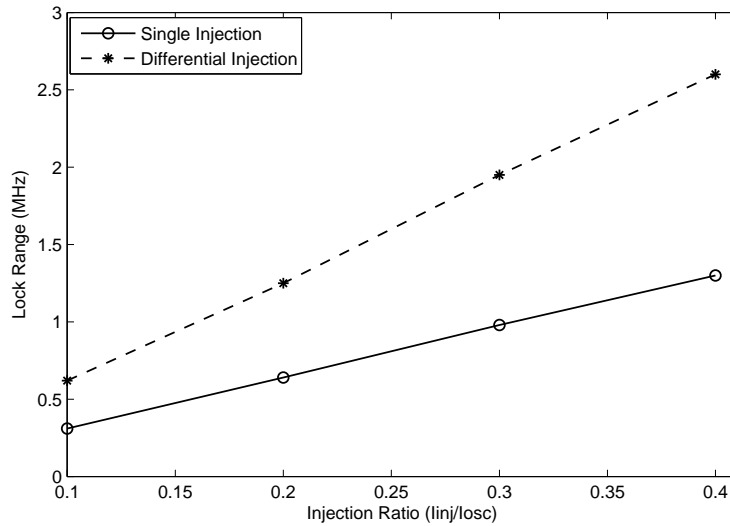


Figure 3.16: Simulated dependence of the lock range of relaxation oscillator with a two-tone sinusoidal injection and double two-tone injections on injection strength.

Fig. 3.17 compares the lock range of the relaxation oscillator with double single-tone injections, double two-tone injections, and double square-wave injections, all with a 180 degree phase difference. It is seen that the lock range of the oscillator with double square-wave injections is the largest while that with double single-tone injections is the lowest. These observations are in a good agreement with the theoretical results derived earlier.

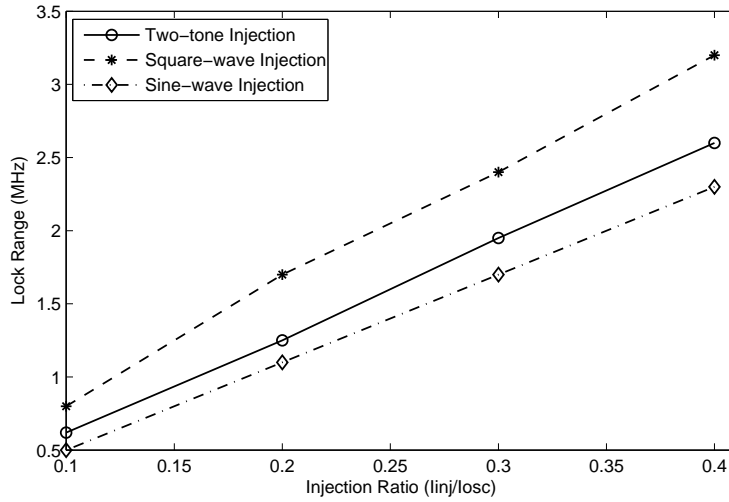


Figure 3.17: Simulated dependence of the lock range of relaxation oscillator with double single-tone injections, double two-tone injections, and double square-wave injections on injection strength.

3.9 Summary

By representing non-harmonic oscillators with a set of harmonic oscillators, and using similar approach presented in Chapter 2, the intrinsic relation between the lock range of harmonic oscillators and that of non-harmonic oscillators is obtained. Also, the resemblance of Volterra series analysis for nonlinear circuits is applied to show non-harmonic oscillators with a multi-tone injection exhibit a larger lock range as compared with that with a single-tone injection. Further demonstration shows that non-harmonic oscillators with multiple single-tone injections exhibit a larger lock range as compared with that with a single single-tone

injection. The condition upon which non-harmonic oscillators with multiple single-tone injections exhibits a larger lock range as compared with those with a single-tone injection was obtained. The condition upon which non-harmonic oscillators with multiple multi-tone injections exhibits a larger lock range as compared with those with a single multi-tone injection has also been derived. The above study is critical for some applications. In particular, when the non-harmonic oscillators are employed in passive wireless communications and wireless sensor transceivers, where the power supply is not stabilized, the calibration for local oscillators requires the lock range which has to be wide enough to overcome the frequency drifting. As the characteristics of the oscillating signals are exhibiting more harmonic components, the multiple multi-tones injections are essentially useful to enlarge the lock range.

Chapter 4

A Quadrature Charge-Domain Sampling Mixer with Embedded FIR, IIR, and N-Path Filters

In zero-IF or low-IF RF receivers, a quadrature mixer is commonly employed. The SAW band-pass filter with fixed centre frequency or with a narrow tuning range has to be eliminated for SDR applications. A switched-capacitor based network can be utilized to substitute the SAW filter while providing tunable centre frequency by sampling frequency. A RF receiver employing the windowed integration sampling provides improved attenuation for aliasing and stop-band frequency. In this chapter, a programmable quadrature charge-domain sampling mixer with embedded FIR, IIR, and 4-path band-pass filters is designed. The remainder of the chapter is organized as follows: Section 4.1 investigates the principles of periodic impulse sampling, periodic windowed sampling, and periodic N-path windowed sampling, and their characteristics are compared. Section 4.2 provides a detailed mathematical treatment of charge-domain windowed samplers. In Section 4.3, a quadrature charge-domain sampler with embedded FIR, IIR, and 4-path band-pass filters is proposed and its performance is investigated in detail. Section 4.4 presents the measurement results. A summary is provided in Section 4.5.

4.1 N-path Filters

4.1.1 Periodic Impulse Sampling

Consider the time-varying network shown in Fig. 4.1 where the output of the linear time-invariant (LTI) network with impulse response $h_{BB}(t)$ and bandwidth $\Delta\omega$ is sampled by periodic impulse function $\delta_T(t) = \sum_{n=-\infty}^{\infty} \delta(t - nT_s)$ where $\delta(t) = 1$ if $t = 0$ and 0 otherwise, and T_s is the period. Because $\mathcal{F}[\delta_T(t)] = \frac{2\pi}{T_s} \sum_{n=-\infty}^{\infty} \delta(\omega - n\omega_s)$ where $\mathcal{F}[\cdot]$ is Fourier transform operator and $\omega_s = 2\pi/T_s$.

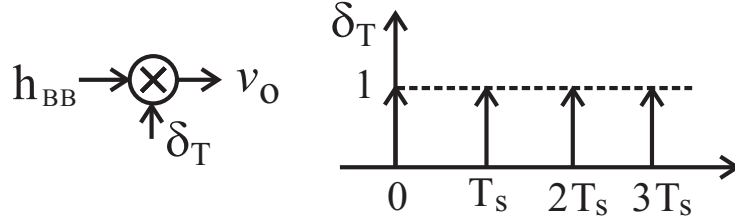


Figure 4.1: Periodic impulse sampling of band-limited signals.

The output is given by $V_o(\omega) = H_{BB}(\omega) \otimes \mathcal{F}[\delta_T(t)]$ where \otimes is convolution operator and $H_{BB}(\omega)$ is the Fourier transform of $h_{BB}(t)$. It follows that

$$V_o(\omega) = \frac{2\pi}{T_s} \sum_{n=-\infty}^{\infty} H_{BB}(\omega - n\omega_s). \quad (4.1)$$

If $\omega_s \geq 2\Delta\omega$, the frequency characteristic of the LTI network will repeat every ω_s with no spectrum overlap, as shown in Fig. 4.2(a). Periodic impulse sampling converts a low-pass filter to band-pass filters. The spectral profile of the band-pass filters (bandwidth, stop-band attenuation,...) is identical to that of the low-pass while the center frequency can be tuned by varying ω_s . The band-pass filter with its center frequency at ω_s will have quality factor $Q = \omega_s/(2\Delta\omega)$. For example, if $\Delta f = 1$ MHz and $f_s = 1$ GHz, we have $Q = 500$.

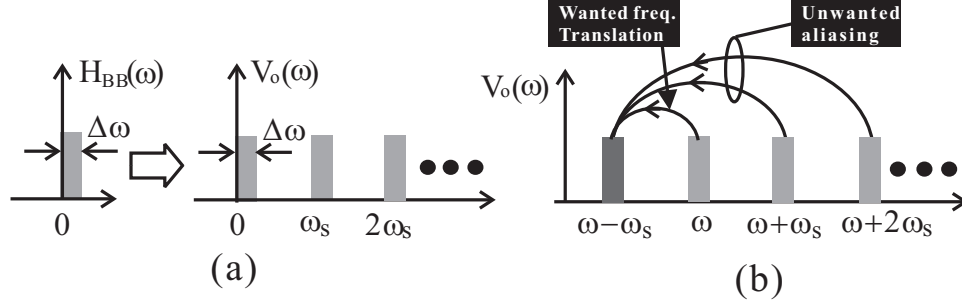


Figure 4.2: (a) Periodic impulse sampling of band-limited signals. Baseband signal at ω is replicated to sidebands at $\omega + n\omega_s$. (b) Periodic impulse sampling of broadband signals. The sideband components of input at $\omega + n\omega_s$ are aliased back to the baseband at ω .

Consider that the input at ω and with bandwidth $\Delta\omega \leq \omega_s/2$ and at the same time other unwanted tones exist at $\omega + n\omega_s$. Assume the desired output is at $\omega - \omega_s$ obtained via mixing. Tones at $\omega + n\omega_s$ will be aliased back to $\omega - \omega_s$, as shown in Fig. 4.2(b). Mechanisms that suppress the effect of the aliasing tones are needed.

4.1.2 Periodic Windowed Sampling

A time-varying network is shown in Fig. 4.3 where the output of the LTI network having a low-pass characteristic with bandwidth ω_B is sampled by periodic windowed function $s_T(t) = 1$ if $nT_s + \sigma_{k-1} \leq t < nT_s + \sigma_k$ and 0 otherwise. σ_k and σ_{k-1} are explicitly defined in Fig. 4.3. Since $s_T(t)$ is periodic with period T_s , it can be represented by Fourier series

$$s_T(t) = \sum_{n=-\infty}^{\infty} S_n e^{jn\omega_s t} \quad (4.2)$$

where

$$\begin{aligned} S_n &= \frac{1}{T_s} \int_0^{T_s} s_T(t) e^{-jn\omega_s t} dt \\ &= \frac{\tau}{T_s} e^{-jn\omega_s \sigma_{k-1}} e^{-jn\omega_s \tau/T_s} \text{sinc}\left(\frac{n\pi\tau}{T_s}\right). \end{aligned} \quad (4.3)$$

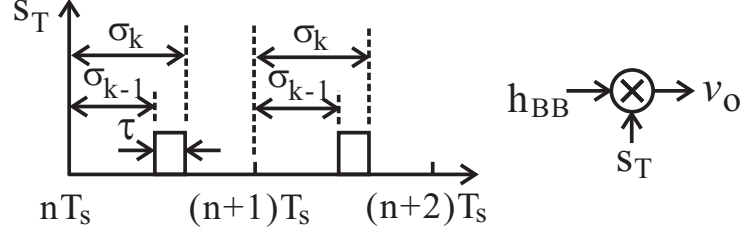


Figure 4.3: Periodic windowed sampling of band-limited signals.

Fourier transform of $s_T(t)$ can be obtained directly through (4.2) and (4.3)

$$S_T(\omega) = \frac{2\pi\tau}{T_s} \sum_{n=-\infty}^{\infty} e^{-jn\omega_s\sigma_{k-1}} e^{-jn\omega_s\tau/T_s} \text{sinc}\left(\frac{n\pi\tau}{T_s}\right) \delta(\omega - n\omega_s). \quad (4.4)$$

Fourier transform of $v_o(t) = h_{BB}(t)s_T(t)$ is obtained from

$$\begin{aligned} V_o(\omega) &= H_{BB}(\omega) \otimes S_T(\omega) \\ &= \frac{\tau}{T_s} \sum_{n=-\infty}^{\infty} e^{-jn\omega_s\sigma_{k-1}} e^{-jn\omega_s\tau/2} \text{sinc}\left(\frac{n\pi\tau}{T_s}\right) H_{BB}(\omega - n\omega_s). \end{aligned} \quad (4.5)$$

Consider $\omega_s \geq 2\Delta\omega$ without interferences. Periodic windowed sampling converts it to a set of band-pass filters. Unlike periodic impulse sampling that has a uniform scaling factor $2\pi/T_s$, periodic windowed sampling has a low-pass scaling factor $\text{sinc}(n\pi\tau/T_s)$, as shown in Fig. 4.4(a).

For the case of $\omega_s \geq 2\Delta\omega$ with interferences at $\omega + n\omega_s (n \neq 1)$, if the desired output is at $\omega + \omega_s$, the baseband tone at ω and the interferences at $\omega + n\omega_s$ will be converted to the desired output at $\omega + \omega_s$. Since $|e^{-jn\omega_s\sigma_{k-1}}| = |e^{-jn\omega_s\tau/2}| = 1$, the aliasing effect at $\omega + n\omega_s$ will be magnitude-shaped by the scaling factor $\text{sinc}(n\pi\tau/T_s)$.

Unlike periodic impulse sampling, periodic windowed sampling introduces nulls. For the interferences reside at the nulls, they will be completely suppressed (ideally). As usual, the desired channel occupies a frequency band $\Delta\omega$ rather than a single frequency, although

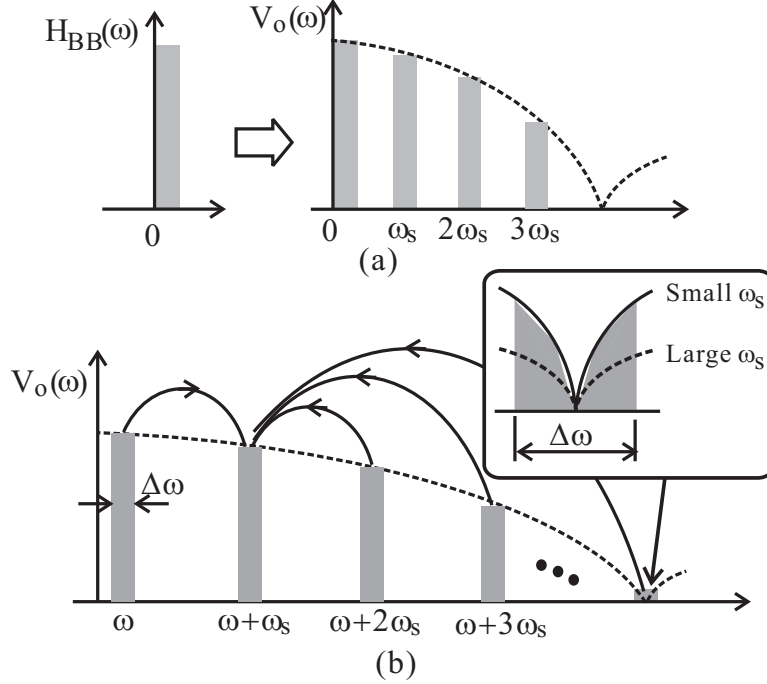


Figure 4.4: (a) Periodic windowed sampling of narrow-band signals without interferences. (b) Periodic windowed sampling of band-limited signals with interferences. Interferences at $\omega + n\omega_s$ are aliased back to the desired baseband.

nulls will be most effective in suppressing aliasing tones at $\omega + n\omega_s$, those in the vicinity of $\omega + n\omega_s$ will be suppressed but with less attenuation, as illustrated graphically in Fig. 4.4(b). Also, increasing ω_s will improve the attenuation of tones in the vicinity of the nulls. This, however, is at the cost of increased power consumption.

4.1.3 Periodic N-Path Windowed Sampling

N-path filters introduced in 1960s [111] offer the intrinsic advantages of a programmable center frequency, programmable bandwidth, low-cost, and an interleaved operation enabling low-speed circuits to process high-frequency inputs. An interleaved N-path filter is shown in Fig. 4.5 with a total of N identical networks sampled by window function $s_k(t)$ defined as $s_k(t) = 1$ if $nT_s + \sigma_{k-1} \leq t < nT_s + \sigma_k$ and 0 otherwise. Since $s_k(t)$ is periodic with period T_s , we have $s_k(t) = \sum_{n=-\infty}^{\infty} S_{k,n} e^{jn\omega_s t}$ where $S_{k,n} = \frac{1}{N} \text{sinc}\left(\frac{n\pi}{N}\right) e^{j\frac{n\pi}{N}} e^{-j\frac{2n\pi}{N}}$. Note that $\tau = T_s/N$

was utilized. Fourier transform of $s_k(t)$ is given by

$$S_k(\omega) = \frac{2\pi}{N} \sum_{n=-\infty}^{\infty} \text{sinc}\left(\frac{n\pi}{N}\right) e^{j\frac{n\pi}{N}} e^{-j\frac{2nk\pi}{N}} \delta(\omega - n\omega_s). \quad (4.6)$$

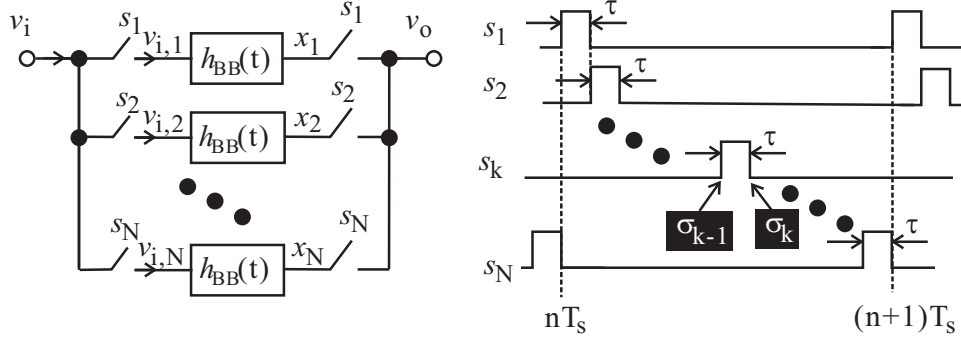


Figure 4.5: N-path filter. Sampling mixers are implemented using switches driven by a sampling clock with N non-overlapping phases. Non-overlapping uniform sampling pulse width: $\tau = T_s/N$. $\sigma_k = \sigma_{k-1} + \tau$ and $\sigma_{k-1} = nT_s + (k-1)\tau$.

Fourier transform of $v_{i,k} = v_i(t)s_k(t)$ is obtained from convolution

$$V_{i,k}(\omega) = \frac{1}{N} \sum_{n=-\infty}^{\infty} \text{sinc}\left(\frac{n\pi}{N}\right) e^{j\frac{n\pi}{N}} e^{-j\frac{2nk\pi}{N}} V_i(\omega - n\omega_s) \quad (4.7)$$

where $V_i(\omega)$ is the Fourier transform of $v_i(t)$. The output of k th LTI block before the second mixer $x_k(t)$ is given by $x_k(t) = v_{i,k}(t) \otimes h_{BB}(t)$ and its Fourier transform $X_k(\omega)$ is given by

$$X_k(\omega) = \frac{1}{N} \sum_{n=-\infty}^{\infty} \text{sinc}\left(\frac{n\pi}{N}\right) e^{j\frac{n\pi}{N}} e^{-j\frac{2nk\pi}{N}} V_i(\omega - n\omega_s) H_{BB}(\omega). \quad (4.8)$$

The output in k th phase is obtained from

$$\begin{aligned}
v_{o,k}(t) &= x_k(t)s_k(t) \\
&= \frac{1}{N} \sum_{m=-\infty}^{\infty} \text{sinc}\left(\frac{m\pi}{N}\right) e^{j\frac{m\pi}{N}} e^{-j\frac{2mk\pi}{N}} x_k(t) e^{jm\omega_s t}.
\end{aligned} \tag{4.9}$$

The index m associated with the second set of switches is used in (4.9). It is straightforward to show that

$$\begin{aligned}
V_o(\omega) &= \sum_{k=1}^N \mathcal{F}[v_{o,k}(t)] \\
&= \frac{1}{N} \sum_{k=1}^N \sum_{m=-\infty}^{\infty} \text{sinc}\left(\frac{m\pi}{N}\right) e^{j\frac{m\pi}{N}} e^{-j\frac{2mk\pi}{N}} X_k(\omega - m\omega_s) \\
&= \left(\frac{1}{N}\right)^2 \sum_{k=1}^N \sum_{m,n=-\infty}^{\infty} \text{sinc}\left(\frac{m\pi}{N}\right) \text{sinc}\left(\frac{n\pi}{N}\right) e^{j\frac{(m+n)\pi}{N}} \\
&\quad e^{-j\frac{2(m+n)k\pi}{N}} V_i[\omega - (m+n)\omega_s] H_{BB}(\omega - n\omega_s), (m+n = KN, K = 0, 1, 2, \dots). \tag{4.10}
\end{aligned}$$

Since $|e^{j(m+n)\pi/N}| = 1$ and $|e^{-j2(m+n)k\pi/N}| = 1$, we obtain the magnitude of $V_o(\omega)$ from (4.10)

$$\begin{aligned}
V_{o,m}(\omega) &= \frac{1}{N^2} \sum_{m,n=-\infty}^{\infty} \text{sinc}\left(\frac{m\pi}{N}\right) \text{sinc}\left(\frac{n\pi}{N}\right) \\
&\quad V_i[\omega - (m+n)\omega_s] H_{BB}(\omega - n\omega_s), (m+n = KN, K = 0, 1, 2, \dots). \tag{4.11}
\end{aligned}$$

The transfer function of the N-path filter at ω is obtained by letting $m+n=0$

$$H_{BP}(\omega) = \frac{V_o(\omega)}{V_i(\omega)} = \frac{1}{N^2} \sum_{n=-\infty}^{\infty} \text{sinc}^2\left(\frac{n\pi}{N}\right) H_{BB}(\omega - n\omega_s). \tag{4.12}$$

As compared with periodic windowed sampling,

1. Periodic N-path windowed sampling provides a sinc^2 low-pass characteristic with -40 dB/dec attenuation to suppress unwanted tones while periodically windowed sampling provides a sinc low-pass characteristic with -20 dB/dec attenuation.

2. Both periodically windowed sampling and periodic N-path windowed sampling provide nulls to suppress aliasing interferences at and in the vicinity of nulls.
3. For periodic N-path windowed sampling from (4.12), the N-path sampling can be applied to select frequency components near by ω_s in a manner analogous to employing a band-pass filter at the high frequency. Meanwhile the quality factor of the band-pass filter ideally is only determined by the base-band spectral profile, e.g. H_{BB} is a low-pass filter. The center of the band-pass filter is precisely controlled by the ω_s .
4. Apart from the band-pass filtering at the desired frequency, ω_s , there are also response peaks around all the other harmonics of the switching frequency. In other words, the unwanted signals will be accompanied with the wanted tones through the switching systems. The severe drawback, which can be observed from (4.11), is the folding of interferences at some harmonics of ω_s on the top of the desired signal at ω_s . For example, if N is 4 and the desired signal is located at $\omega_s + \omega$, the closest harmonic, which will introduce aliasing signals, is located at $3\omega_s$. And the next will be $5\omega_s$.
5. The location of the nulls in periodic N-path windowed sampling is heavily depending on the number of the paths. In other words, increasing the number of paths moves nulls to high frequencies, lowering the overall fold-over effect of aliasing interferences at and near the nulls due to the increasing attenuation of these unwanted tones at high frequencies. It is of interest to notice that the harmonic rejection at all the other harmonics is also decreased by increasing the number of paths. Take a 4-path and 8-path filter for example, the 3rd-harmonic of the 4-path filter is located at $0.75*4\omega_s$ with 20 dB insertion loss. The 3rd-harmonic of the 8-path filter, however, is located at $0.375*8\omega_s$ with only 4 dB attenuation.

The following example shown in Fig. 4.6(a) [90] illustrates a simplified single-ended N-path filter, where N is 4 and τ is $T_s/4$. The targeting signal is at in the vicinity of ω_s . The input voltage v_i is converted to current i_i first. i_i is then switched by $s_k(t)$ and integrated onto C_B . Fig. 4.6(b) shows the non-overlapping multi-phase clocking scheme for the switching system. In other words, for every periodic switching, only one capacitor is being charged or

discharged. The the output impedance of the transconductor and single-ended capacitors form a low-pass filter with time constant $\tau_B = R_{out}C_B$ where R_{out} is the output impedance of the transconductor, if the ON-resistance of the switches is sufficiently small. From 4.12, H_{BB} is denoted by a first-order integrator, $H_{BB} = \frac{R_{out}}{1 + j\omega R_{out}C_B}$.

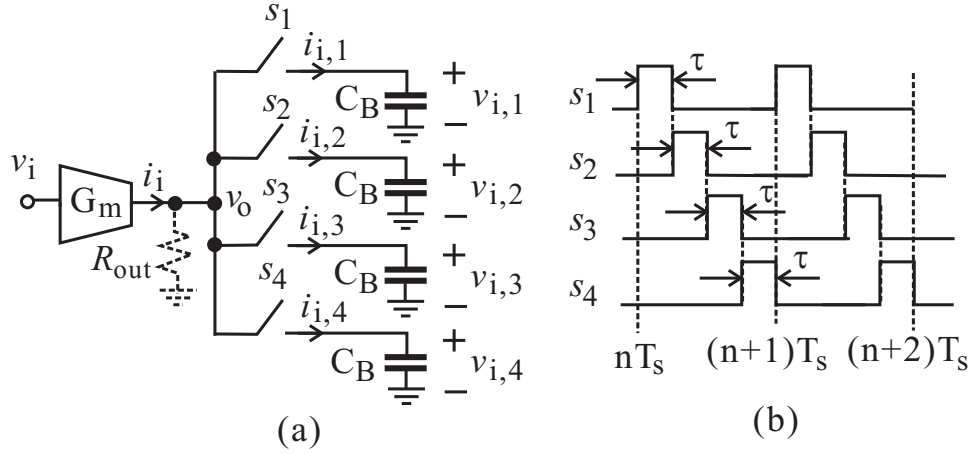


Figure 4.6: Single-ended 4-path filter.

A careful inspection of Fig. 4.6 reveals that it realizes the same function as Fig. 4.5 does. The sampled current $i_{i,k}(t) = i_i(t)s_k(t)$ produces voltage $v_{i,k}(t) = i_{i,k}(t) \otimes z_B(t)$ across the capacitor where $z_B(t)$ is the impulse response of the load. As the charge on each capacitor has nowhere to flow except for flowing back to the input port of the switch, which is same as x_k in Fig. 4.5 passing through second mixer. $v_{i,k}(t)$ is then sampled by the switches to produce $v_o(t)$: $v_o(t) = \sum_{k=1}^4 v_{i,k}(t)s_k(t)$. $v_o(t)$ can be obtained by the network shown in Fig. 4.7.

The whole concept of substituting the conventional band-pass filter can be understood in the form of impedance looking into the input the switching system. If the baseband impedance around DC presents a very large value, the impedance at ω_s will be very large due to the switching system. From Fig. 4.6, the baseband low-pass filter is then converted to a high-frequency band-pass filter. The out of band of the band-pass filter exhibits a low impedance path to those interferences residing at the frequency offsets from ω_s while the desired signal

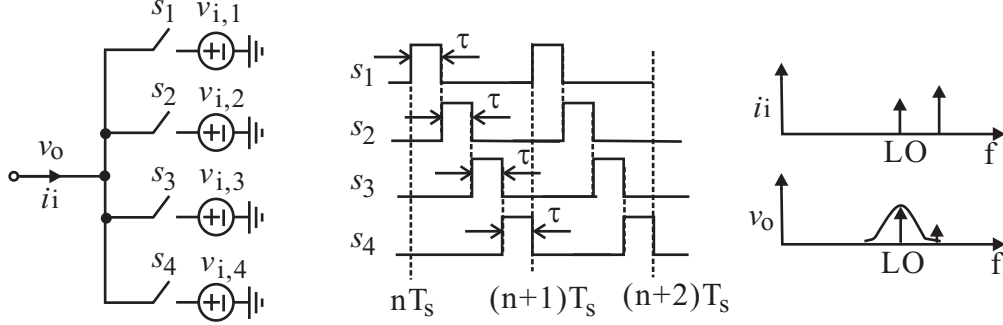


Figure 4.7: Single-ended 4-path filter.

will be picked up. The quality factor of this type filter is feasible to be designed over 1000 depending on the bandwidth and the center frequency. Fig. 4.8 plots the simulated PSS-PAC frequency response of the 4-path band-pass filter shown in Fig. 4.7 with $G_m=1$ mS, $f_s = 100$ MHz with 25% duty cycle, and $C_B=40$ pF. It is seen that the 4^{th} and 8^{th} harmonics vanish due to the frequency-shaping in (4.12). Also observed is the sinc envelope of the frequency response with notches at $4f_s, 8f_s, \dots$. The 4-path band-pass filter can also be implemented differentially. In this case, the differential form removes all even number harmonics components and DC.

4.2 Charge-Domain Windowed Sampling

4.2.1 Sinc Low-Pass Filter

This section examines the operation of the charge-domain sampler shown in Fig. 4.9. The input voltage signal is converted to a current through a G_m cell with the transconductance gain G_m , followed by a switched-capacitor(SC) circuit. It is worth to mention that the realization of integrator is possible to use OPAMP-based integrator. Each period of the sampling clock consists of three phases : the reset phase ($s_r = 1$) where sampling capacitor C_s is reset, the integration phase ($s_i = 1$) where the output current of the transconductor is integrated onto the sampling capacitor, C_s , over T_i period, and the readout phase ($s_o = 1$) at a rate $f_s = 1/T_s$, as shown in Fig. 4.9. The reset operation ensures that there is no relation between the output of the sampler at the end of adjacent sampling periods. Let

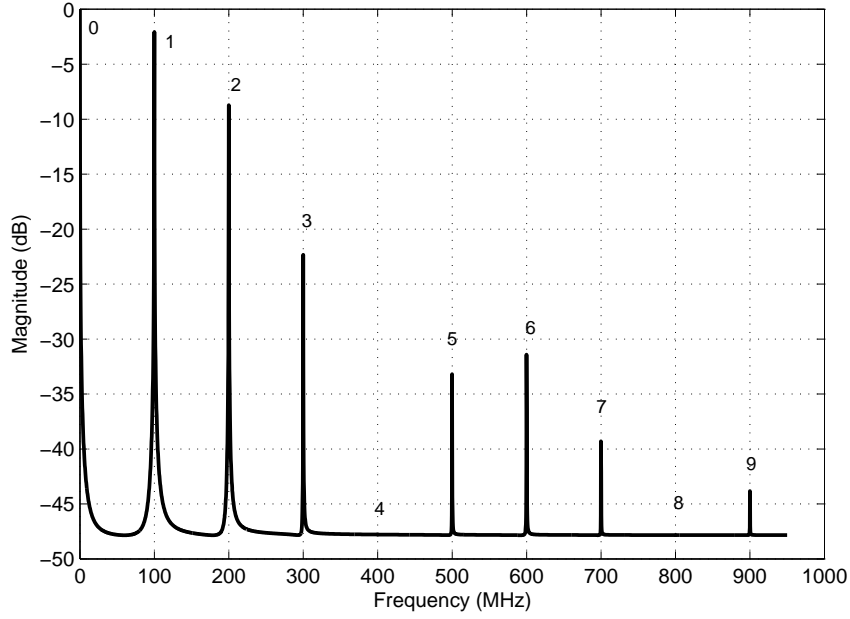


Figure 4.8: Frequency response of single-ended 4-path filter in Fig. 4.6.

$v_i(t) = e^{j\omega t}$. Because $v_i(t)$ is a single tone of unit amplitude, the corresponding output is the transfer function of the system. The output voltage at the end of the integration phase T_i is given by

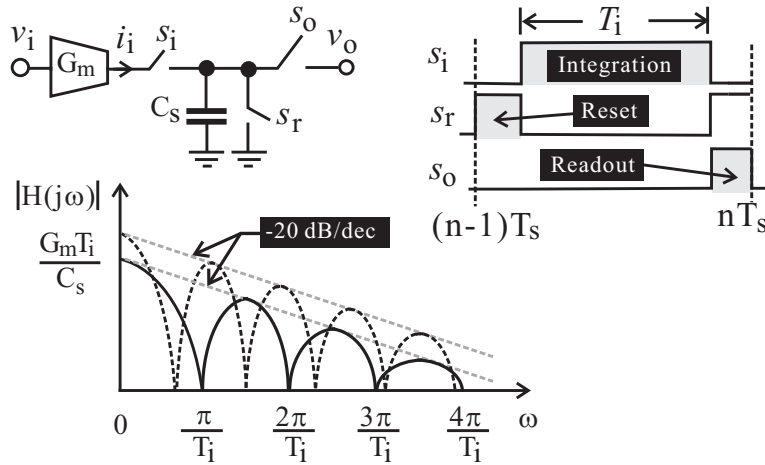


Figure 4.9: Charge-domain sampling. Solid line : Small T_i . Dashed line : Large T_i .

$$\begin{aligned}
v_o(nT_s) &= \frac{G_m}{C_s} \int_{nT_s-T_i}^{nT_s} e^{j\omega t} dt \\
&= \frac{G_m T_i}{C_s} e^{jn\omega T_s} e^{-j\omega T_i/2} \text{sinc}\left(\frac{\omega T_i}{2}\right).
\end{aligned} \tag{4.13}$$

The ideal frequency response of the output signal as a function of input signal from (4.13) can be expressed as

$$H_{\text{sinc}}(j\omega) = \frac{G_m T_i}{C_s} \left| \text{sinc}\left(\frac{\omega T_i}{2}\right) \right|. \tag{4.14}$$

$|H_{\text{sinc}}(j\omega)|$ is sketched in Fig. 4.9. It is of interest to notice that the charge-domain windowed sampling process can be represented by two independent signal processing operations, a continuous-time (CT) sinc filtering due to integration of the signal current within a windowed period and a sampling process at the rate, $f_s = 1/T_s$. The preceding results are commented as:

1. Charge-domain windowed sampling provides a sinc low-pass characteristic with nulls at $\omega = n\pi/T_i$ and a -20 dB/dec attenuation. The signal bandwidth is determined by T_i , and is approximately $0.44/T_i$, shown in Fig. 4.10.

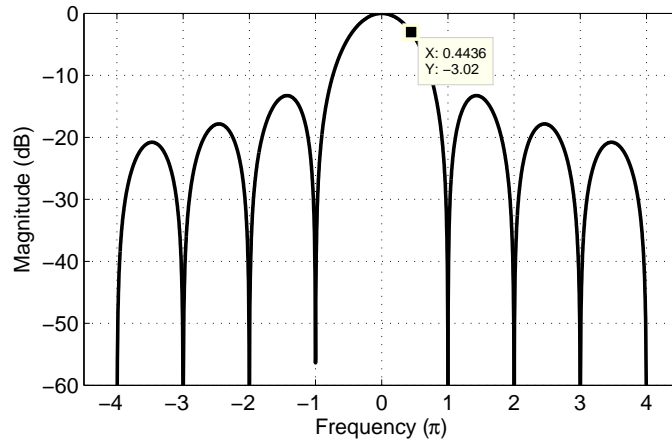


Figure 4.10: Gain-normalized transfer function of sinc.

2. The gain of the filter in the passband $0 \leq f \leq 0.44/T_i$ is not constant but rather drops with frequency in a sinc fashion. The low-pass obtained from charge-domain windowed sampling therefore does not have a flat passband.
3. The largest gain occurs at DC and is given by $G_m T_i / C_s$. Increasing T_i not only reduces the bandwidth of the charge-domain sampler, it also boosts the DC gain. Also the larger the sampling capacitor, the lower the gain. On the other hand, the larger the transconductance, the larger the gain. The latter, however, is accompanied with more power consumption.
4. Since nature of sinc function is low-pass and the attenuation in the main lobe is small, the desired output should be placed inside the main lobe, preferably close to DC. This requires that $\omega \ll \omega_i$ or equivalently $T_i \ll T$ where $\omega_i = \pi/T_i$ is the frequency of the first null.
5. For a given input at frequency ω , if the desired output is at DC, the sampling frequency $\omega_s = 2\pi/T_s$ is chosen such that $\omega - \omega_s = 0$. Since $T_s = T_r + T_i + T_o$ where T_r and T_o are the reset time and readout time, respectively, T_i will therefore vary with T_s . This will in turn affect the gain of the sampler given by $H_{sinc}(0) = G_m T_i / C_s$ unless G_m is also varied accordingly such that $G_m T_i$ remains unchanged. Since most receivers require an Automatic Gain Control (AGC), this gain variation can be tuned out as part of the AGC function. As a result, no additional hardware is needed. Alternatively, the gain of the transconductor can also be varied..
6. If the desired output is at DC, assume $T_i = T_s$, aliasing interferences at $n\omega_i$ will be fully attenuated. If the desired signal is close to DC, aliasing interferences are located near the nulls and will also be attenuated by the nulls, however, by a less amount.
7. As demonstrated in [86, 112], the depth of the nulls is greatly affected by the imperfection of the sampler, specifically, the finite output impedance of the transconductor as the finite output impedance of the transconductor reduces the effective current integrated onto the sampling capacitor. As a result, the effectiveness of the nulls in suppressing aliasing interferers is reduced.

The importance of the concept of the charge-domain sampler in Fig. 4.9 is that the current integration provides an elementary low-pass sinc response and the input signal bandwidth is primarily set by integrating time, T_i . On the contrary, in voltage sampler, the input signal bandwidth is limited by the time constant, $\tau = RC$, where R is the ON-resistance of the switches and C is the sampling capacitance. Given the same bandwidth for both two samplers, the performance of low-pass sinc filter ideally outperforms the simple low-pass RC filter as the unwanted signal at the notches can be suppressed significantly. The simple structure of charge-domain sampler in Fig. 4.9, however, does not take full advantage of anti-aliasing sinc filter since the T_i is directly related to T_s , i.e. T_s is not equal to T_i . In theory, T_i and T_s are two distinct parameters. T_s determines the spectral location and Nyquist bandwidth of the sampled signal while T_i sets the nulls. To minimize the fold-over signal on top of the desired signal, it is preferable to set $T_i = T_s$ when the sampler is utilized in the baseband sampling. The need of reset and read out period in sampling operations, however, cannot be avoided. This issue is resolved by using time interleaved charge-domain sampling circuits, illustrated in Fig. 4.11.

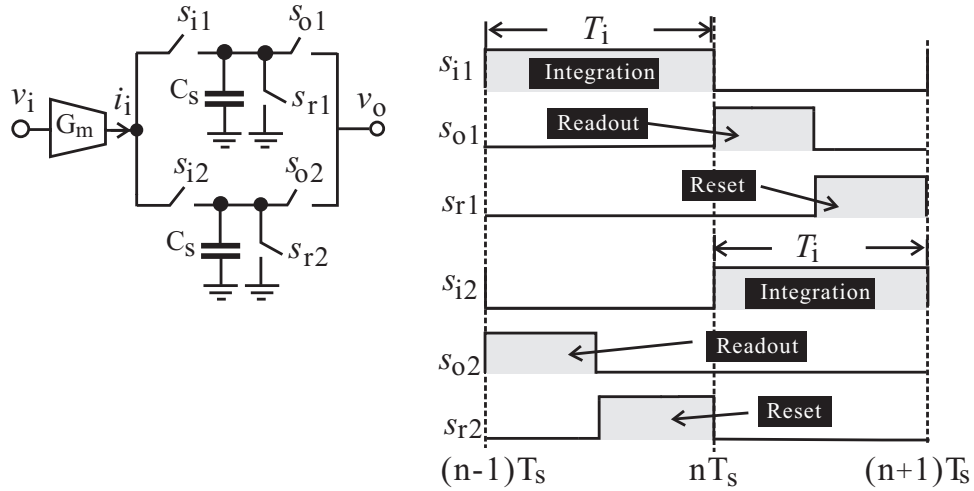


Figure 4.11: Time interleaved charge-domain sampling.

In this case, one integrator is involved in integrating the input current while the other one is in the phase of read out and reset and vice versa. Therefore, the charges in every integration

period is transferred to the subsequent stage. As a result, the sampling period of the sampler is $T_s = T_i$, leading to place the notches of the sinc response on top of the multiples of $1/T_s$, which ideally remove the aliasing effect near by DC. If longer time slots for read out and reset are required, more than two paths can be used to further relax the timing requirement.

4.2.2 FIR Filter

-20 dB/dec attenuation provided by elementary charge-domain windowed sampling is inadequate in suppressing unwanted channels. It was shown in [112] that sinc low-pass provided by the charge-domain windowed sampling can be greatly enhanced by partitioning the integrating phase into multiple sub-integration phases, as shown in Fig. 4.12. Further, for k th integration phase, a weighting factor h_k is assigned. The current to be integrated on the sampling capacitor C_s during k th sub-phase is given by $i_{i,k}(t) = G_m v_i h_k$. Let $v_i(t) = e^{j\omega t}$. The output voltage of the sampling capacitor at the end of n th sampling period is given by

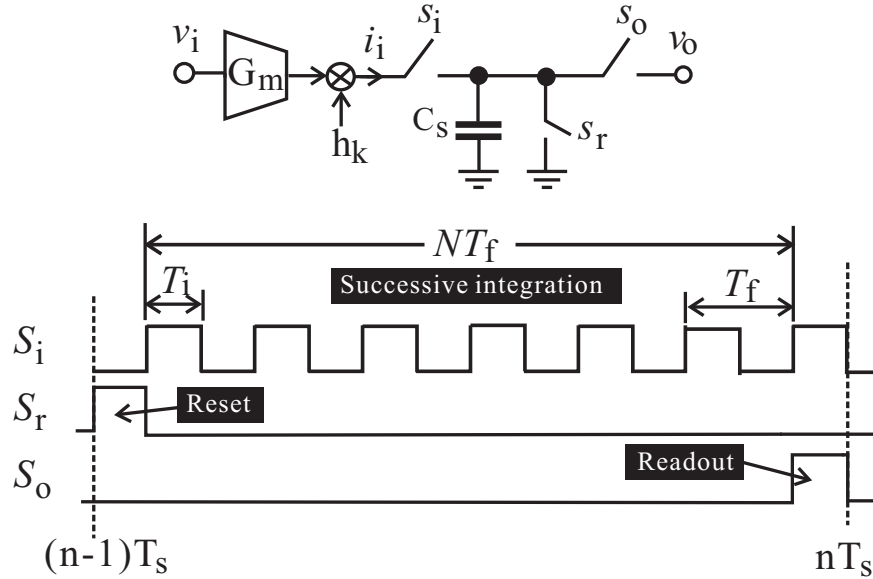


Figure 4.12: Charge-domain sampler with built-in FIR filter.

$$\begin{aligned}
v_o(nT_s) &= \frac{G_m}{C_s} \sum_{k=0}^{N-1} \left(h_k \int_{nT_s-kT_f-T_i}^{nT_s-kT_f} e^{j\omega t} dt \right) \\
&= \frac{G_m (1 - e^{-j\omega T_i})}{j\omega C_s} \sum_{k=0}^{N-1} h_k e^{jn\omega T_s} e^{-j\omega k T_f}.
\end{aligned} \tag{4.15}$$

Defining $z = e^{j\omega T_f}$ and noting $|e^{jn\omega T_s}| = 1$, we obtain magnitude transfer function

$$|H(j\omega)| = \frac{G_m T_i}{C_s} \left| \text{sinc} \left(\frac{\omega T_i}{2} \right) \sum_{k=0}^{N-1} h_k z^{-k} \right| = H_{sinc} H_{FIR} \tag{4.16}$$

where H_{sinc} was defined in (4.14) and $H_{FIR} = \sum_{k=0}^{N-1} h_k z^{-k}$. Eq.(4.16) shows that two distinct filtering functions, namely, a CT sinc low-pass and a DT FIR filter of order N , are realized simultaneously. The continuous-time sinc low-pass is due to the continuous integration of the input current over $[0, T_i]$ while the discrete time FIR is due to multiple integrations in one T_s . A special case is when $h_k = 1$, $k = 0, 1, 2, \dots$, the unity tap weight of the FIR filter gives rise to a temporal moving average characteristic. Assume $T_f/T \ll 1$. This is often true since T_s is chosen close to T in order to generate a near DC output while $T_s = NT_f$ with N typically large in order to increase the order of the FIR filter. It follows that $z^{-1} = e^{-j2\pi T_f/T} \approx 1 - j2\pi \frac{T_f}{T}$. As a result, Eq.(4.16) becomes

$$H_{FIR} = \frac{1 - z^{-N}}{1 - z^{-1}} = N e^{-jN\pi T_f/T} \text{sinc} \left(N\pi \frac{T_f}{T} \right). \tag{4.17}$$

Eq.(4.17) shows that the temporal moving average filter implements a sinc low-pass with nulls at $\omega = (n/N)\omega_f$ where $\omega_f = 2\pi/T_f$ and $n = 1, 2, 3, \dots$, which is often used in the decimation as anti-aliasing filter. There are total $N-1$ zeros evenly distributed in the frequency range from DC to $1/T_f$, resulting in multiple notches. The optimal output sampling rate is located at the multiple zeros. Therefore, the number of N limits the decimation ratio. Also, it is evident that the larger the value of N , the narrower the nulls and the less the suppression of unwanted channels in the vicinity of the nulls. Reducing N , though improving attenuation,

increases the readout rate. Also observed from (4.17) is that the larger the value of N , the larger the voltage gain provided by the temporal moving average filter. Fig. 4.13 and Fig. 4.14 show the comparison of $N=10$ and $N=5$. The overall magnitude transfer function of Fig. 4.12 is given by

$$|H(j\omega)| = \frac{NG_m T_i}{C_s} \left| \text{sinc}\left(\frac{\omega T_i}{2}\right) \text{sinc}\left(\frac{N\pi T_f}{T}\right) \right|. \quad (4.18)$$

and is plotted in Fig. 4.15. It can be expected that the joint effect of $\text{sinc}\left(\frac{\omega T_i}{2}\right)$ and $\text{sinc}\left(\frac{N\pi T_f}{T}\right)$ will not only increase the attenuation in the stop-band, thereby improving the suppression of unwanted channels, it will also increase the depth of the nulls, improving the suppression of aliasing interferers at and in the vicinity of the nulls.

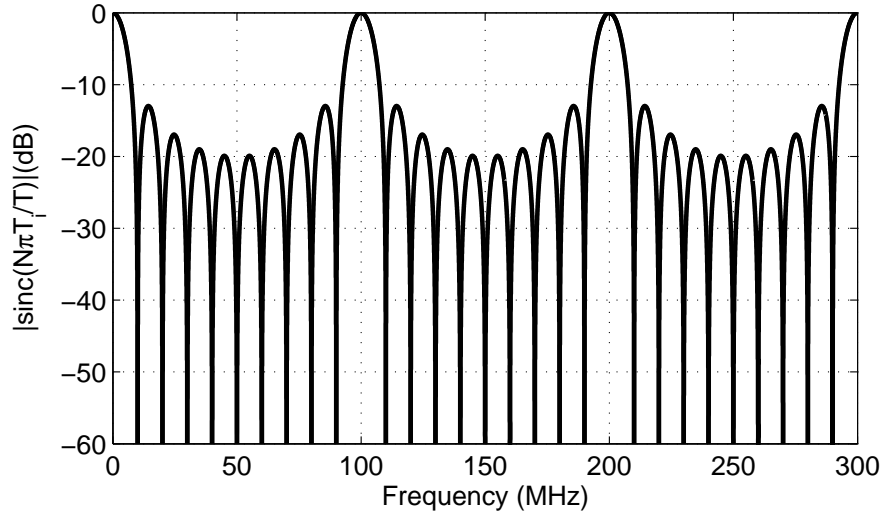


Figure 4.13: Spectrum of charge-domain windowed sampler with FIR filtering. Parameters: $f_s=10$ MHz, $N=10$ and $T_f = T_s/N$.

In conclusion, the CT sinc low-pass response from the current windowed integration nevertheless produces zeros at the multiples of the frequency $1/T_i$. The first sidelobe provides maximal 13 dB attenuation on unwanted signal. Like conventional DT filters, the pass-band of the embedded FIR filter from multiple windowed integration of the current signal in charge-domain sampling circuits is repeated at intervals of its sampling frequency, $1/T_f$.

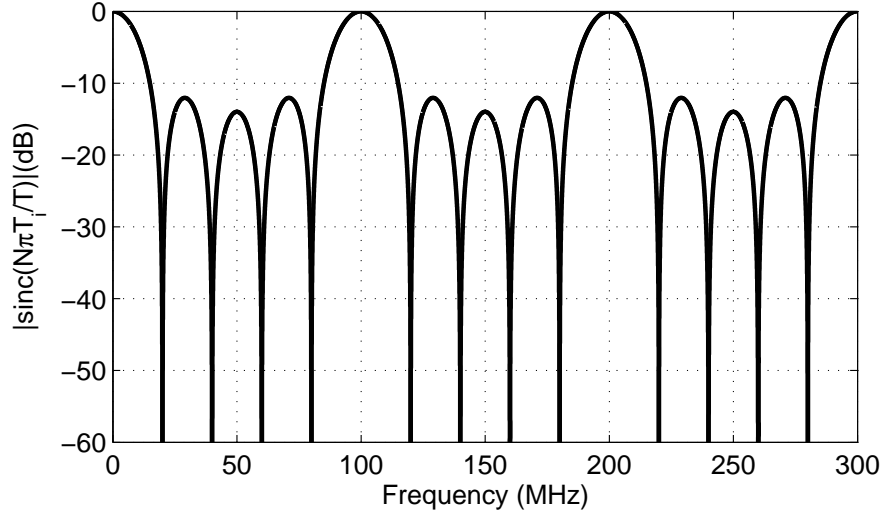


Figure 4.14: Spectrum of charge-domain windowed sampler with FIR filtering. Parameters: $f_s=20$ MHz, $N=5$ and $T_f = T_s/N$.

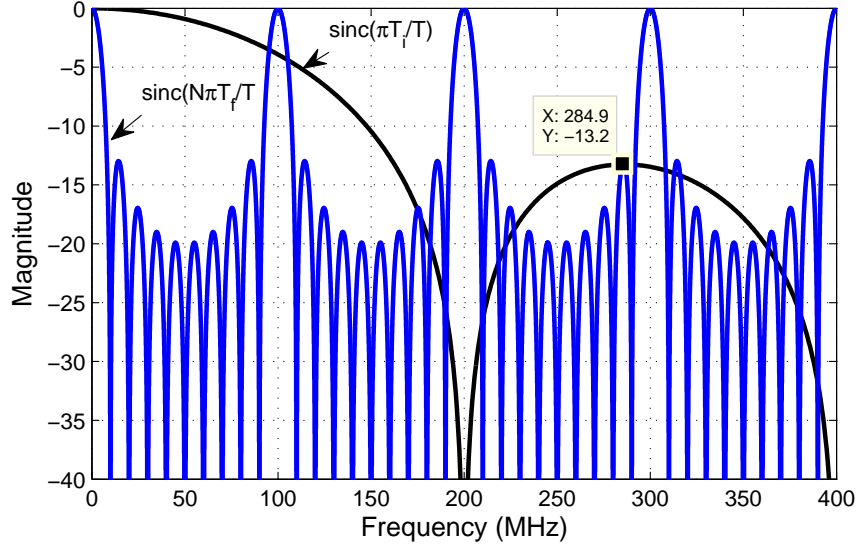


Figure 4.15: Spectrum of charge-domain windowed sampler with CT sinc low-pass filter. $f_i=200$ MHz, $f_s=10$ MHz, $N=10$ and $T_f = T_s/N$.

The final readout rate of the sampler is set at $T_s = NT_f$. In addition, the phase response of CT and DT sinc filters are ideally linear and can be denoted by group delay in time-domain response.

4.2.3 IIR Filter

The build-in CT sinc and DT sinc low-pass filter of the charge-domain sampler developed in above limit the input bandwidth of the sampler and suppress the aliasing signal at the integer multiples of $1/T_i$ and N/T_f , which effectively provide anti-aliasing filtering function for the sampler. It is worth to note that the selectivity for channel selection, however, is merely elementary and limited. High order or more advanced FIR filter can be implemented to improve the filtering functions, e.g. sharper frequency transition band, and larger attenuation in sidelobs. The cost is increased complexity of the circuit and power consumption. In comparison with FIR filter, a infinite impulse response (IIR) filter is efficient to provide same frequency response while consuming less arithmetic resources. It was shown in [80] a IIR low-pass characteristic can be obtained by employing the recursive operation of a history capacitor and rotating capacitors, as shown in Fig. 4.16. The time interleaved structure is shown in Fig. 4.17.

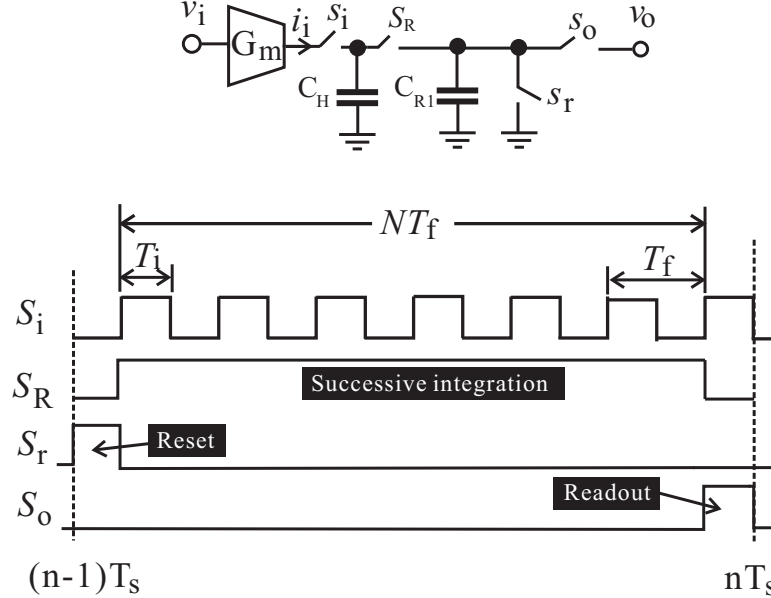


Figure 4.16: Charge-domain sampler with a build-in FIR and IIR filter and its timing scheme.

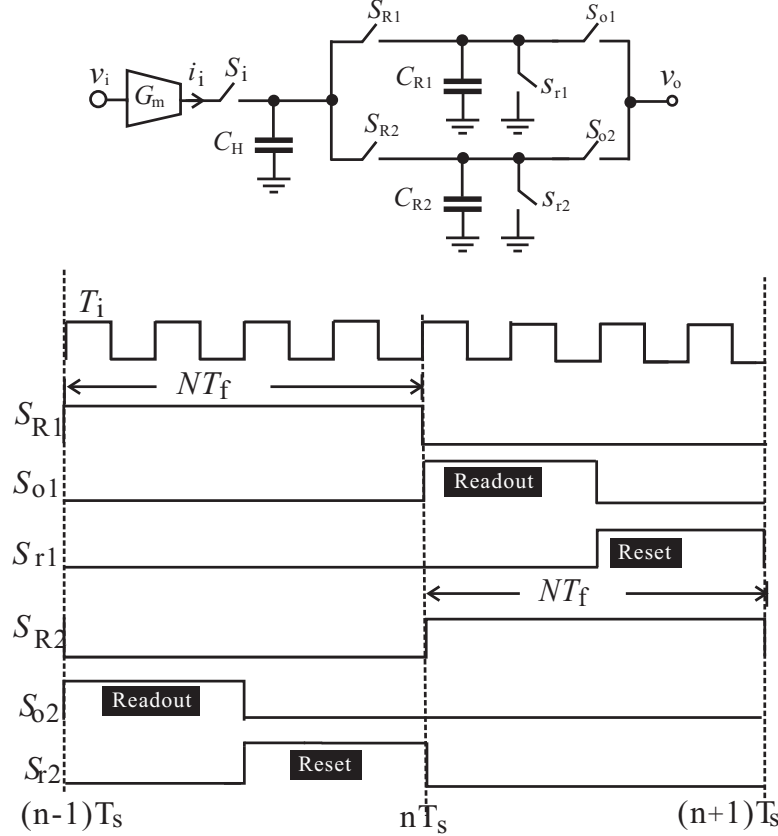


Figure 4.17: Time interleaved charge-domain sampler with a build-in FIR and IIR filter and its timing scheme.

From Fig. 4.17, the integration capacitor is partitioned into history capacitor C_H and rotation capacitors C_{R1} and C_{R2} . C_H is always charged by the windowed current from the transconductor, and it is never discharged to entirely. While the rotation capacitors are sharing the charges with C_H and discharging entirely. $C_{R1,2}$ are switched between reset/integration and read-out operation. Assume $C_H = aC_s$ and $C_{R1,R2} = (1 - a)C_s$, the total integration capacitance seen by $i_i(t)$ is always $C_s = C_H + C_{R1,R2}$. Consider $(n - 1)$ th phase and assume $S_{R1}=1$ and $S_{R2}=0$. The current is integrated onto $C_H + C_{R1} = C_s$ while the charge of C_{R2} is transferred to the load. Let the total charge stored in the integration capacitors C_H and C_{R1} in $(n - 1)$ th phase be $Q(n - 1)$. In the following n th phase where $S_{R1}=0$ and $S_{R2}=1$, the charge stored in C_{R1} is transferred to the load. Since C_{R1} and C_{R2} are always reset before they are connected to C_H , the loss of the charge of the integration capacitors will be the charge of C_{R1} . If the total charge stored in the integration capacitors

C_H and C_{R2} at the end of n th phase is $Q(n)$, the amount of the charge provided by the transconductor during n th phase, denoted by $Q_{in}(n)$, is equal to the charge of C_{R1} and is therefore given by $Q(n) - aQ(n-1)$, i.e.

$$Q(n) = aQ(n-1) + Q_{in}(n). \quad (4.19)$$

Or equivalently, it can be expressed in the z-domain as:

$$\frac{Q_z}{Q_{in}} = \frac{1}{1 - az^{-1}}. \quad (4.20)$$

where $a = \frac{C_H}{C_H + C_{R1,R2}}$, a value which is always smaller than unity. Since $Q(n) = C_s V_{o,IIR}(n)$, $Q(n-1) = C_s V_{o,IIR}(n-1)$, and $Q_{in}(n) = C_s V_{o,FIR}(n)$, note that the output of the FIR filter is the input of the IIR filter as

$$V_{o,IIR}(n) = aV_{o,IIR}(n-1) + V_{o,FIR}(n). \quad (4.21)$$

Eq.(4.21) is a first-order IIR filter. It can be shown from $z^{-1} = e^{sT_s} \approx 1 - sT_s$ that

$$H_{IIR}(s) \approx \frac{1}{1 - a} \frac{1}{s \left(\frac{aT_s}{1-a} \right) - 1}. \quad (4.22)$$

The pole of the first-order IIR filter is given by $\omega_{p,IIR} = \frac{1}{T_s} \left(\frac{1}{a} - 1 \right)$ and the gain of the IIR filter is maximized at DC and is given by $1/(1-a)$. It is seen that the larger a is, the larger the gain of the IIR filter and the smaller the pole frequency subsequently the more the attenuation. In other words, a plays a key role in input bandwidth and attenuation.

This agrees well with the simulated results in Fig. 4.18, showing a frequency response of first-order IIR low-pass filter for different capacitance ratio values .

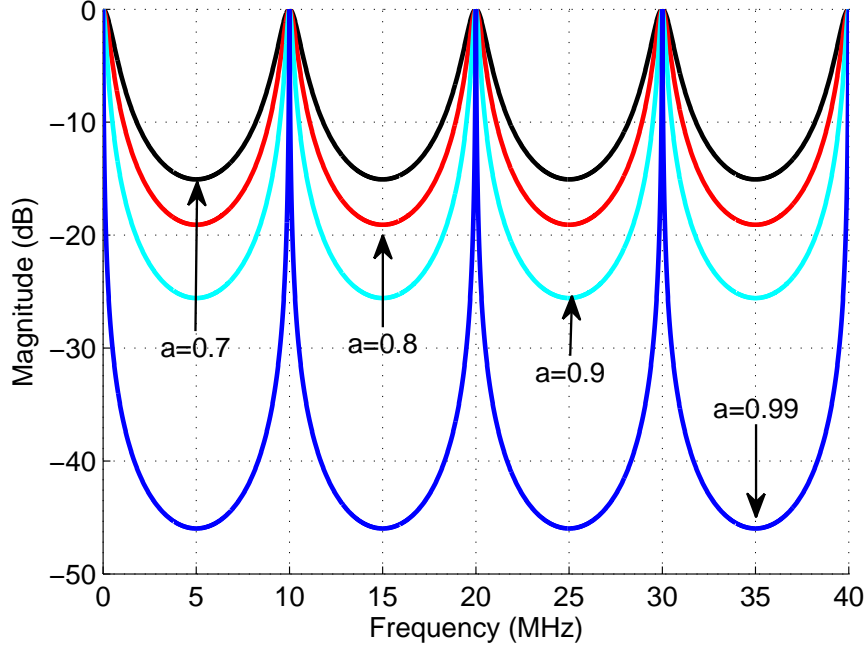


Figure 4.18: Spectrum of charge-domain windowed sampler with first-order IIR filter. $f_s=10$ MHz.

In conclusion, a partial channel select filter is carried out by using first-order DT IIR low-pass filter in the charge-domain sampler with acceptable modification. The IIR filtering operation is taking place at the output sampling rate, $f_s = 1/T_s$. The pole location of the IIR filter is merely determined by the capacitor value ratio, $a = \frac{C_H}{C_H + C_{R1,R2}}$, which can be precisely controlled by layout, and f_s . The passbands of the IIR filter are repeated at intervals of $k f_s$. It is noticed that in Fig. 4.17, there are a total number of three filters taking place in the signal path, i.e. the first-order CT sinc filter, the first-order DT sinc filter, and the first-order DT integrator.

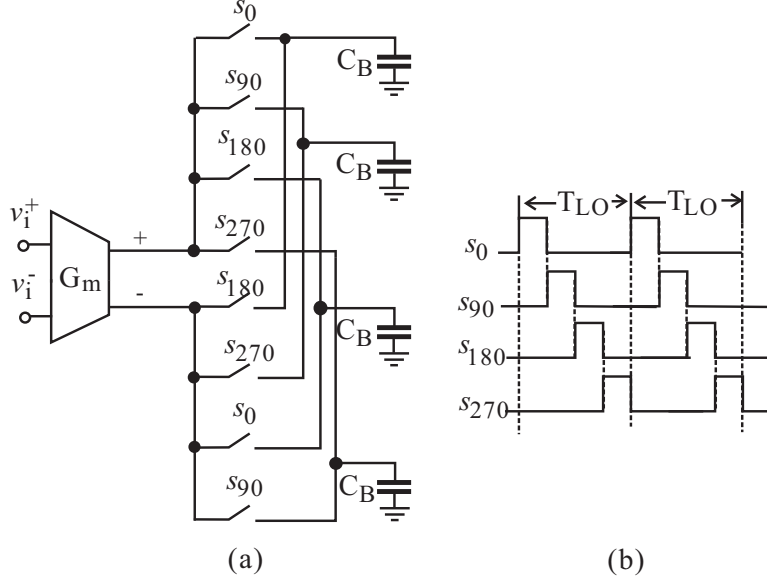


Figure 4.20: (a) Differential 4-path band-pass filter, (b) Clocking scheme.

other hand, the large parasitic capacitors because of the large TG can be merged into the capacitance of base-band capacitors, C_B . The PSS-PAC simulated result is shown in Fig. 4.21.

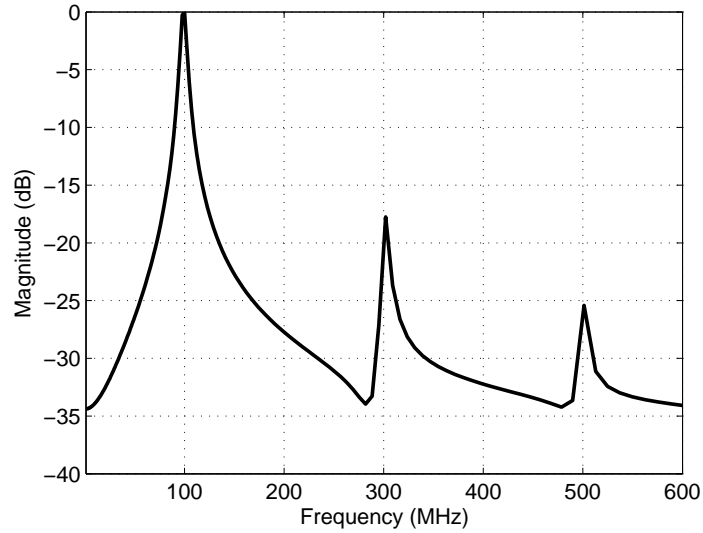


Figure 4.21: Simulated differential 4-path band-pass filter with $T_s = T_{LO} = 100$ MHz.

A complete circuit schematic of I channel of quadrature charge-domain sampler (QCDS) is shown in Fig. 4.22. The schematic for Q channel is identical except that FLO90 and FLO270 are used in Q channel. The QCDS is fully differential, and for each of I and Q channels, the signal path is further split into two paths as time interleaved configuration. Since both the 4-path band-pass filter and quadrature charge-domain sampler contain only capacitors and switches, and the currents of the transconductor M1/M2 are re-used by the quadrature charge-domain sampler, minimizing power consumption.

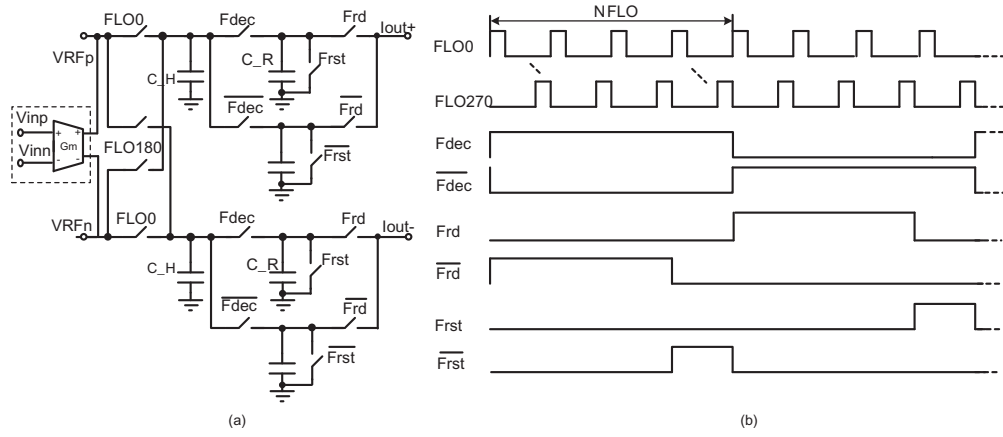


Figure 4.22: (a) Differential charge-domain sampler (only half of the circuit is shown), (b) Clocking scheme.

4.3.1 Performance

The entire system consists of four distinct functional blocks, namely, a 4-path band-pass filter, a continuous-time sinc low-pass filter, a FIR filter, and an IIR low-pass filter with transfer function H_{BP} , H_{sinc} , H_{FIR} , and H_{IIR} , respectively. The overall transfer function is given by $H = H_{BP}H_{sinc}H_{FIR}H_{IIR}$. The 4-path bandpass H_{BP} provides a maximum of -40/dec dB attenuation. The continuous-time sinc low-pass obtained from the continuous integration of the input over T_i provides -20/dec dB attenuation. The IIR filter provides another -20/dec dB attenuation. Finally, the attenuation provided by the FIR filter is determined by the number of integration phases and the weight factors. Although the overall

attenuation is large, since -3dB frequency of these filters differ and it is likely not possible to have all the filters to have the same -3 dB frequency, the attenuation in the desired stop-band is rather small. The nonidealities of devices further reduces the attenuation. Fig. 4.23 shows the output of the quadrature charge-domain sampler with different history capacitor. It can be seen that increasing the capacitance of the history capacitor improves the attenuation in the stop band and the depth of the nulls. Attenuation is further increased when the 4-path bandpass filter is added. Also, the depth of the nulls of the sampler with the 4-path bandpass filter are much deeper as compared with that without the 4-path bandpass filter. This observation reveals that the 4-path bandpass filter not only attenuates the tones in the stop-band, qualifying it as a band select filter to suppress blockers, it also improves the suppression of aliasing interferences.

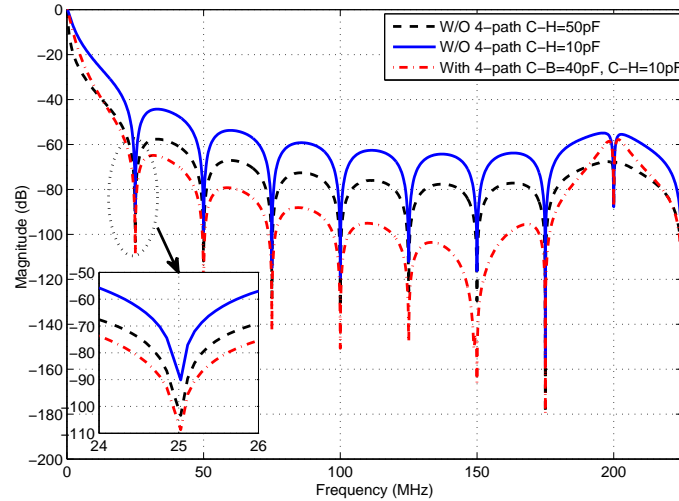


Figure 4.23: Simulated transfer function (normalized) of quadrature charge-domain sampler. Ideal transconductor with $g_m = 0.5$ mS and ideal switches with $R_{on} = 1\Omega$ and $R_{off} = 1T\Omega$ are used. The input is a 100 MHz sinusoid. The sampling frequency is 100 MHz with 25% duty cycle. Voltage gain provided by the sampler is 15 dB.

4.3.2 Noise

An explicit noise analysis of the quadrature charge-domain sampling circuit is crucial as the noise contribution to the total system Noise Figure can be significant due to the limited gain of the preceding LNA. In order to evaluate the noise performance of the circuit, follow the approach in [113]. Let the power of the input-referred noise-voltage generator of the sampling mixer be $\overline{v}_{n, in}^2$. The power of input-referred noise-current generator of the sampling mixer is negligible. The total input noise is obtained from $\overline{v}_{n, in}^2 = \overline{v}_{n, R_s}^2 + \overline{v}_n^2$ where \overline{v}_{n, R_s}^2 is the noise power of the source resistor.

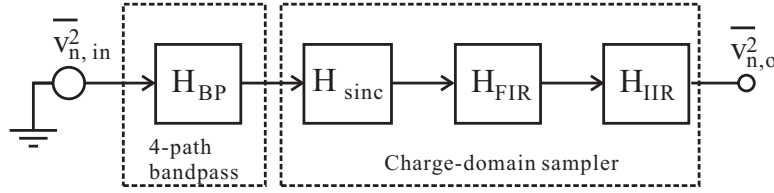


Figure 4.24: Noise analysis of proposed charge-domain sampling mixer.

From the schematic of the sampling mixer, except for the noise voltage from source, there are two noise sources existing, e.g. modelled thermal noise of output impedance of the transconductor and the thermal noise of switch resistors. Compared with output impedance of transconductor, R_{on} is typically small. For example, in Fig. 4.20, $R_{out} \approx 10 \text{ k}\Omega$ and $R_{on}=15$. Since $R_{out} \gg R_{on}$, the noise voltage of switch resistors is significantly smaller than that of R_{out} . Therefore, the noise voltage of switch resistors can be ignored and only modelled noise voltage of output impedance is related to \overline{v}_n^2 . As shown in Fig. 4.24, the input noise is first shaped by the 4-path bandpass filter. It then passes through the charge-domain sampler that provides a continuous-time first-order sinc low-pass $H_{sinc}(j\omega)$, a discrete-time FIR filter $H_{FIR}(j\omega)$ from the multiple sub-integration phases, and the first-order IIR filter $H_{IIR}(j\omega)$ from the history and rotation capacitors. The total power of the output noise is obtained from

$$\overline{v_o^2} = \int_0^\infty |H_{BP}H_{sinc}H_{FIR}H_{IIR}|^2 \overline{v_{n,in}^2} d\omega. \quad (4.23)$$

To quantify the effect of H_{BP} , H_{sinc} , H_{FIR} , and H_{IIR} , the noise bandwidth of the sampling mixer with H_{BP} , H_{sinc} , H_{FIR} , and H_{IIR} are considered individually. To simplify analysis, assume $\overline{v_{n,in}^2}$ is white, and the noise of interferences is not taken into consider.

Noise Bandwidth With H_{BP} Considered

Consider the effect of the N-path bandpass only. For the 4-path filter shown in Fig. 4.20, the baseband block is a first-order low-pass with transfer function $H_{BB} = 1/(s/\omega_B + 1)$ where $\omega_B = 1/(R_{out}C_B)$ is -3 dB frequency and R_{out} is the output impedance of the transconductor. The transfer function of the N-path band-pass filter was derived earlier in (4.12), where the thermal noise, attenuated by the periodical band-pass filtering at the multiple ω_s and is folded back to the desired signal. In the design, $R_{out} \approx 10k\Omega$ and $C_B = 40$ pF, -3 dB frequency is 398 KHz while the sampling frequency is 100 MHz and the first notch is located 400 MHz. As a result, the input noise voltage is folded at 300 MHz with 20 dB attenuation, 30 dB attenuation at 500 MHz and etc. This is evident in (4.24) where output noise power of the 4-path filter at $\omega - \omega_s$ is computed and illustrated graphically in Fig. 4.25.

$$\begin{aligned} \overline{v_{n,o}^2}(\omega - \omega_s) &= 0.0625 \left[|H_{BB}(\omega - \omega_s)|^2 + \text{sinc}^4\left(\frac{\pi}{4}\right) |H_{BB}(\omega)|^2 \right. \\ &\quad \left. + \text{sinc}^4\left(\frac{2\pi}{4}\right) |H_{BB}(\omega + \omega_s)|^2 + \dots \right] \overline{v_{n,in}^2}. \end{aligned} \quad (4.24)$$

Since $\text{sinc}^4\left(\frac{\pi}{4}\right) \approx 0.656$, $\text{sinc}^4\left(\frac{\pi}{2}\right) \approx 0.16$, $\text{sinc}^4\left(\frac{3\pi}{4}\right) \approx 0.009$, $\text{sinc}^4\left(\frac{5\pi}{4}\right) \approx 0.001$, $\text{sinc}^4\left(\frac{6\pi}{4}\right) \approx 0.002$, $\text{sinc}^4\left(\frac{7\pi}{4}\right) \approx 0.0003$,..., the folding effect can be approximated by only considering the first two terms of (4.24). As a result, the output noise power at $\omega - \omega_s$ is given by $\overline{v_{n,o}^2}(\omega - \omega_s) = 0.074\overline{v_{n,in}^2}$.

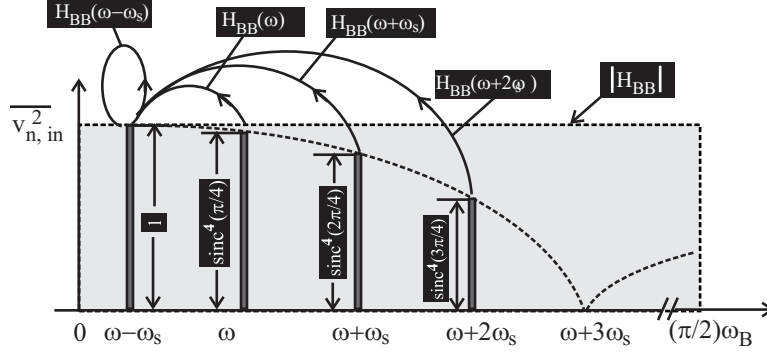


Figure 4.25: Noise analysis of N-path filter.

The noise bandwidth of the baseband block is given by $\frac{\pi}{2}\omega_B$. To find out the noise bandwidth of the sampling mixer with only H_{BP} considered, the calculated total output noise power of the sampling mixer is given by

$$\begin{aligned}
 \overline{v_{no}^2} &= \int_0^\infty |H_{BP}|^2 \overline{v_{n,in}^2} d\omega \\
 &= \left(\frac{1}{N^2}\right)^2 \sum_{n=-\infty}^\infty \text{sinc}^4\left(\frac{n\pi}{N}\right) \left(\frac{\pi}{2}\omega_B\right) \overline{v_{n,in}^2} \\
 &\approx 0.074 \left(\frac{\pi}{2}\omega_B\right) \overline{v_{n,in}^2}.
 \end{aligned} \tag{4.25}$$

Note $N = 4$ was utilized in (4.25).

Noise Bandwidth With H_{sinc} Considered

Consider the effect of H_{sinc} only. Utilizing (4.14), we obtain from (4.23)

$$\overline{v_o^2} = \frac{1}{2\pi} \left(\frac{G_m T_i}{C_s}\right)^2 \int_0^\infty \text{sinc}^2\left(\frac{\omega T_i}{2}\right) \overline{v_{n,in}^2} d\omega \tag{4.26}$$

Since $\int_0^\infty \text{sinc}^2(x) dx = \frac{\pi}{2}$, Eq.(4.26) becomes $\overline{v_o^2} = \frac{G_m^2 T_i}{C_s^2} \frac{T_i}{2} \overline{v_{n,in}^2}$. Since $\overline{v_o^2} = \frac{G_m^2 T_i^2}{C_s^2} \overline{v_{n,in}^2} \omega_{N,sinc}$ where $\omega_{N,sinc}$ is the noise bandwidth when only H_{sinc} is considered, we have $\omega_{N,sinc} = \frac{\omega_i}{2} = \omega_f$ where $\omega_i = 2\pi/T_i$.

Noise Bandwidth With H_{FIR} Considered

Consider the effect of H_{FIR} only. Utilizing (4.17), we have from (4.23)

$$\overline{v_o^2} = \int_0^\infty \text{sinc}^2(N\pi T_f f) \overline{v_{n,in}^2} df = \frac{N}{2T_f} \overline{v_{n,in}^2}. \quad (4.27)$$

Since

$$\overline{v_o^2} = N \overline{v_{n,in}^2} \omega_{N,FIR} \quad (4.28)$$

where $\omega_{N,FIR}$ is the noise bandwidth when only H_{FIR} is considered, we have $\omega_{N,FIR} = \frac{\omega_f}{2}$ where $\omega_f = 2\pi/T_f$.

Noise Bandwidth With H_{IIR} Considered

Consider the effect of H_{IIR} only. Since H_{IIR} is a first-order low-pass with pole frequency $\omega_{IIR} = \frac{1}{T_s} \left(\frac{1}{a} - 1 \right)$, the noise bandwidth due to H_{IIR} is given by $\omega_{N,IIR} = \frac{\pi}{2} \omega_{IIR}$. Since $T_s = T_r + T_o + NT_f$, if $NT_f \gg T_r, T_o$, we have $T_s \approx NT_f$. As a result, $\omega_{N,IIR} \approx \frac{1}{4N} \left(\frac{1}{a} - 1 \right) \omega_f$.

Table 4.1: Noise Bandwidth of Sampling Mixer with 4-path Bandpass, sinc, FIR, and IIR Filters Considered Individually.

Filter	Noise bandwidth
N-path bandpass	$\omega_{N,BP} = \pi/2 \omega_B$
sinc low-pass	$\omega_{N,sinc} = \omega_f, \omega_f = \omega_i/2$
FIR filter	$\omega_{N,FIR} = \omega_f/2, \omega_f = \omega_i/N$
IIR filter	$\omega_{N,IIR} = 1/4N (1/a - 1) \omega_f$

Table 4.1 tabulates the noise bandwidth of the sampling mixer with the 4-path bandpass, sinc, FIR, and IIR filters considered individually. In the design, $N=4$, $C_H=10$ pF, $C_R=1$ pF. Thus, $a = 0.9$ and $\omega_{IIR} = \omega_f/(16 \times 9) \ll \omega_{N,FIR}, \omega_{N,sinc}$. Compared the noise bandwidth of four, $\omega_{N,BP}$ and $\omega_{N,IIR}$ is much smaller than the other two. The total output noise of

the sampling mixer can therefore be obtained from $\overline{v_{no}^2} \approx \omega_{N,IIR} \overline{v_{n,in}^2}$ and $\overline{v_{no}^2} \approx \omega_{N,BP} \overline{v_{n,in}^2}$.

4.3.3 Effect of Nonidealities

Fig. 4.26 investigates the effect of the ON-resistance of the switches on the performance of the 4th-path band-pass filter. It is seen that the larger the resistance of the switches, the less the attenuation in the stop band, revealing that minimizing the channel resistance of the switches is essential.

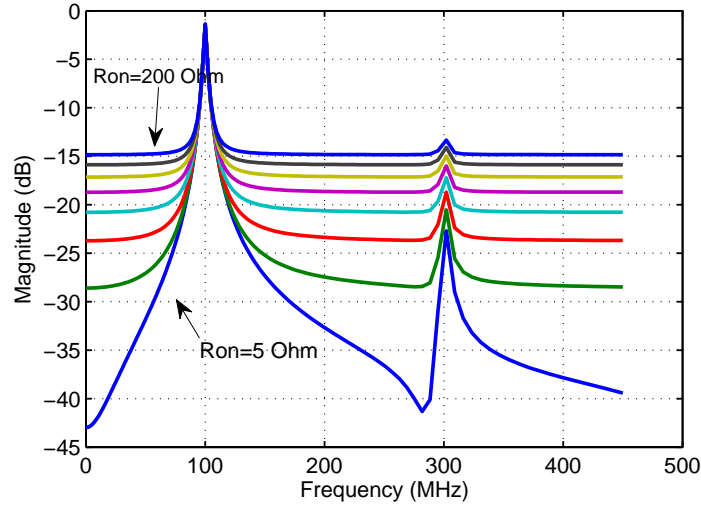


Figure 4.26: Simulated effect of ON-resistance of switches on 4-path bandpass filter. R_{on} is varied from 5 Ω to 200 Ω .

Since the parasitic capacitances of switches are absorbed into the large sampling capacitors (40 pF) of the 4-path bandpass filter, their effect on the performance of the filter is rather small. The parasitic capacitances of the switches, however, lower the gain of the charge-domain sampler. Unlike the 4-path bandpass filter, the ON-resistance of switches has a less detrimental effect on the charge-domain sampler [86]. To maximize the gain, small switches are used in QCDS. Fig. 4.27 shows the normalized transfer function of the quadrature charge-domain sampling receiver with embedded FIR, IIR, and 4-path bandpass

filters at process corners. It is observed that the variation of attenuation due to process spread is within 10 dB. The voltage gain is 6.9 dB for slow nMOS/slow pMOS (SS) and 14.4 dB for fast nMOS/fast pMOS (FF).

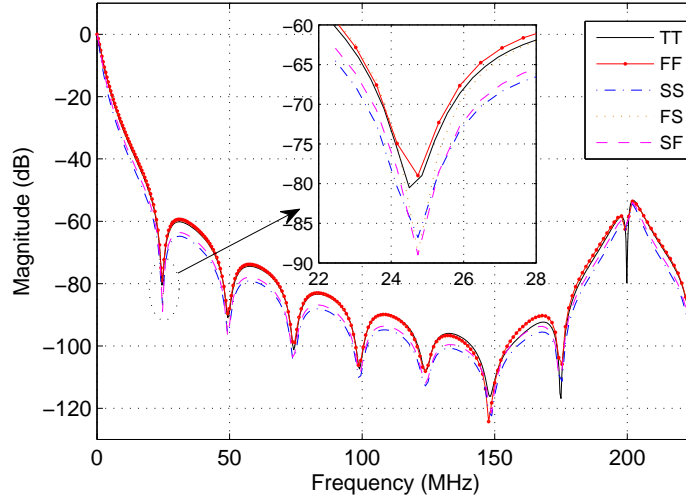


Figure 4.27: Simulated frequency response (normalized) of quadrature charge-domain sampler with embedded 4-path bandpass filter at process corners. The input frequency is 100 MHz, the output baseband sampling frequency is 25 MHz (Two 12.5 MHz interleaved clocks with 50% duty-cycle). Legends: TT (typical nMOS/typical pMOS), SS (slow nMOS/slow pMOS), FS (fast nMOS/slow pMOS), SF (slow nMOS/fast pMOS), and FF (fast nMOS/fast pMOS).

Not like simple sampling systems, the effect of the non-ideal clock is more clear. Since the design is a multiple sampling system, the impacts from sampling clocks are complex but critical.

clock phase noise - To simply analysis, let us only consider the desired signal frequency, f_{in} . For 4-path filter, if ideal sampling clocks, f_s , are applied to each of paths, only frequency component located at f_{in} will be first translated into the baseband and integrated on the capacitor. The capacitor is acting as a low-pass filter to short any unwanted signal out of filter bandwidth to the ground. On the contrary, the signal nearby DC will be held on the capacitor and then be translated back to the original frequency because of the second time ON-OFF of the switches. However, if the sampling clock is non-ideal, a skirt profile in spectrum, all the frequency components inside the skirt will be down-converted to baseband

except for the desired signal. The baseband signal then will be up-converted to the desired frequency again where the unwanted components are added on top of the desired signal, deteriorating SNR. The worse case is there is large blocker signal falling in the skirt. This blocker will lower the SNR significantly as it will be added into the desired signal and the low-pass filter in the baseband fails to filter it out. As a result, the phase noise results in increasing noise figure. Similarly, in the charge-domain sampling circuit, phase noise of sampling clock has a detriment on the overall SNR. However, since the frequency translation is accompanied by a continuous-time and a discrete-time since low-pass anti-aliasing filter, which create notches at the sampling frequency, these notches will greatly suppress the effects from the clock phase noise. Meanwhile, the noise on the clock in time domain is denoted by jitter. The clock jitter will change the integration time for a charge-domain sampler, causing error in the final output voltage. While, the clock jitter will has less detrimental to the SNR in a certain frequency range in comparison with voltage sampler. The range is heavily depending on the integration time, T_i .

clock phase imbalance - There are two cases for N-path filter. Consider the variation of the duty cycle, if duty cycle is less than 25%(4-path) for each of path, as we can expect the attenuation on the harmonics will be less. The notches associated with the number of the path will be shifted to higher frequency. Therefore, the harmonics, which are still at the same location, will get less attenuation. As a result, higher fold-over components will be added on the desired signal, deteriorating SNR. For the case of duty cycle is more than 25%, charge sharing between each of the baseband capacitor is occurred. This charge sharing will significantly degrade the filtering function. Take the extreme case for example, duty cycle is 100%, at the same moment, all the capacitors in the 4-path filter are sharing the same incoming charges. The characteristics of the N-path network will be entirely disappeared. The more overlapping, the more filtering function will be lost. In a conclusion, the case of more than 25% duty cycle is even worse than the case of less than 25%. In addition, the imbalanced phase between each of the paths could lead to less image rejection and harmonic folding. For the charge-domain sampler, the clock phase imbalance could result in mismatch in the time-interleaved configuration and subsequently introduce pattern noise located at $f_s/4, f_s/2, \dots$ which are highly undesirable.

The frequency tuning of the sampling mixer is shown in Fig. 4.28. For each input frequency ω_i , the sampling frequency ω_s is adjusted such that the output frequency of the sampling mixer remains unchanged. Since $T_s = T_r + T_o + NT_i$, T_i will also change. Thus, when ω_i increases, ω_s will increase, resulting in a reduction in T_i . Since the gain of the charge-domain sampler at DC is given by $G_m T_i / C_s$, the gain will drop when ω_i increases. This agrees well with the simulation results in Fig. 4.28.

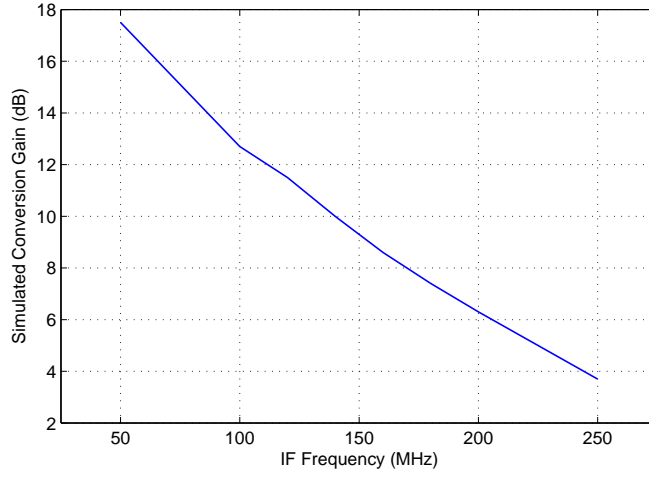


Figure 4.28: Simulated frequency tuning range. The input frequency is varied from 50 MHz to 250 MHz. The sampling frequency is also varied accordingly such that the output frequency remains unchanged.

4.4 Measurement Results

The quadrature charge-domain sampler with embedded FIR, IIR, and 4-path band-pass filters was implemented in IBM cmrf8sf 130 nm 1.2 V CMOS technology. Fig. 4.31 shows the layout of the circuit. The entire chip is $1 \times 2 \text{ mm}^2$. The capacitors in the 4-path filter are two-layer MIM capacitors that provide a higher capacitance density as compared with normal MIM capacitors. Capacitors in the charge-domain sampler are normal MIM capacitors that use only one mask between two metal layers. In addition, to provide an enough driving capability for the switches in the filter blocks, the clock output buffers were

designed to drive a 200 fF load capacitance using D flip-flops (DFFs) implemented using TSPC (True-Single-Phase Clocked) logic. The single-ended input signal from the RF signal generator is fed to the active balun shown in Fig. 4.30 where the single-ended input is converted to a differential input (v_{in} to v_o^+ via a non-inverting common-gate amplifier and v_{in} to v_o^- via an inverting common-source amplifier). The balance of the gain of the two halves of the active balun can be obtained by adjusting V_b of the common-gate. The differential signal is then fed to the transconductor of the 4-path filter. The output of the sampling mixer is fed to a source-follower buffer in order to drive an off-chip RF spectrum analyzer with a 50Ω input impedance.

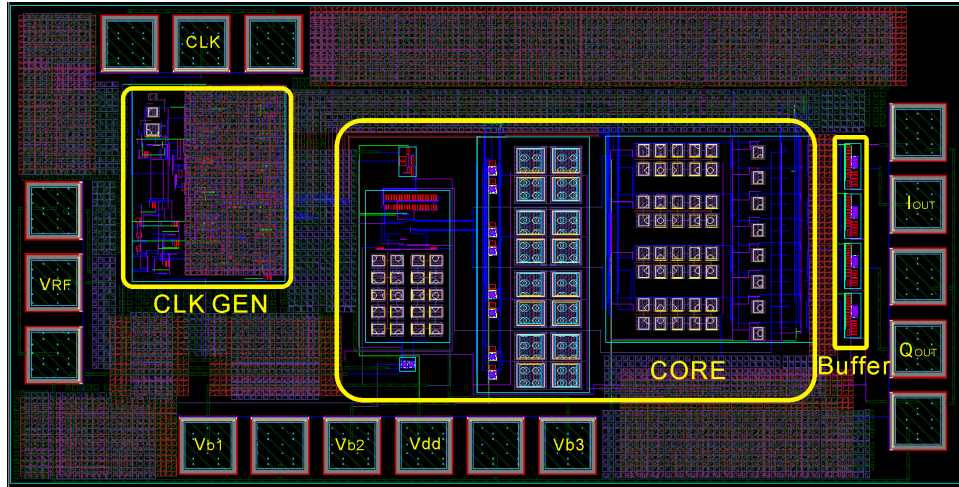


Figure 4.29: Die microphotograph of quadrature charge-domain sampler($1 \times 2 \text{ mm}^2$).

Fig. 4.31 shows the photo-micrograph of the fabricated chip, with probes in place for on-wafer measurement. On-wafer probing was conducted using a Microtech RF-1 microwave probe station (with a Faraday cage) to minimize the effect of package parasitics and external electromagnetic interferers. The pads were arranged based on the configuration of the probes and available silicon area. A Microtech DCQ-06 dc probe, with six ceramic bladed needles configured as SGSSGS (S=signal and G=ground), was used to supply the required dc bias voltages to the chip. Two, single-ended, Microtech ACP-40-D-GSG-150 RF probes were used for the clock and input. One differential Microtech ACP-40-D-GSGSG-150 RF probe

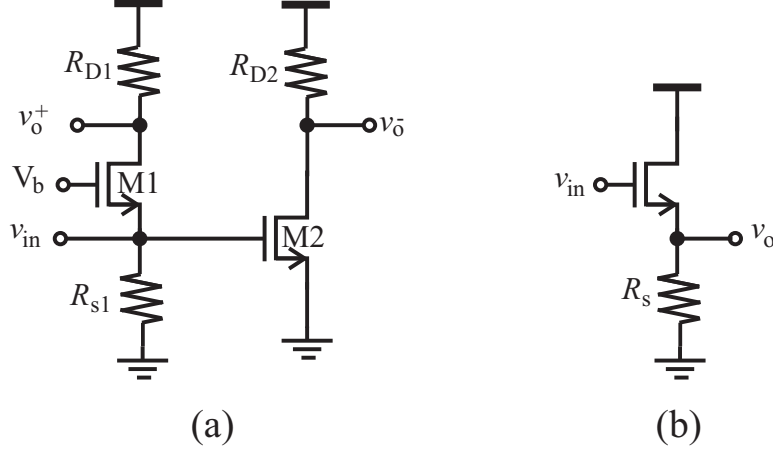


Figure 4.30: (a) Active balun. (b) Output buffer. Circuit parameters of active balun: $W_{1,2} = 300\mu\text{m}$, $R_{s1}, R_{D1}, R_{D2} = 200\Omega$. Circuit parameters of source follower : $W = 300\mu\text{m}$, $R_s = 1\text{k}\Omega$. Length of all transistors is $0.13\mu\text{m}$.

was used to probe the I and Q outputs. Because the center-to-center pitch of the tips of all probes is $150\mu\text{m}$, the dimensions of all bonding pads are $100\mu\text{m} \times 100\mu\text{m}$. This leaves a $50\mu\text{m}$ space between neighboring pads. Flexible RF cables were used to connect the probes including dc probes and test equipment in order to minimize cable loss. The cable loss, including connectors and adapters, was measured and found to be approximately 0.5 dB at 100 MHz.

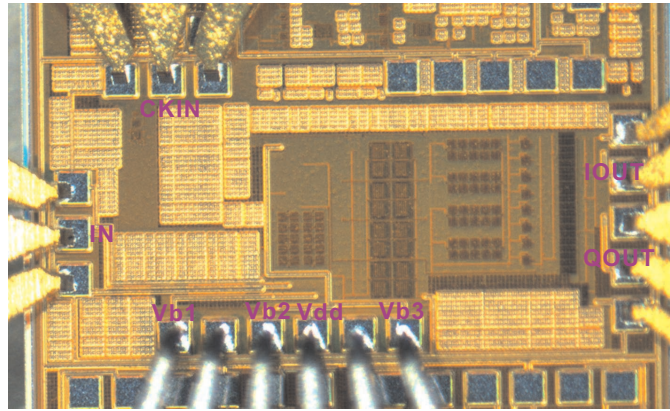


Figure 4.31: Die photo-micrograph of charge-domain sampler with embedded 4-path band-pass filter with probes in place for on-wafer measurement.

The test set-up is shown in Fig. 4.32. Two BK precision 9124 programmable DC power supplies were used in the test set up. One for V_{DD} , dc biasing of the 4-path bandpass filter and common-mode voltage of charge-domain sampler, and the other one is for biasing the on-chip active balun. The ground terminals of all dc power supplies were wired to a common ground plane, in a star configuration, to avoid forming ground loops. All ground pads are connected together, on chip, to avoid any on-chip ground loops. The 100 MHz input signal was generated using an Agilent E4420B 250 kHz \sim 2.0 GHz RF signal generator. The master clock was generated from an Agilent 81130A pattern generator. The clocks used in the 4-path bandpass filter and charge domain sampler were generated from the master clock using an on-chip clock generator. The output waveforms of the quadrature charge-domain sampler were captured using an Agilent MOS-X 3024A 200 MHz oscilloscope. The spectrum of the output of the quadrature charge-domain sampler was measured using an Agilent N9320B 9 kHz \sim 3.0 GHz spectrum analyzer.

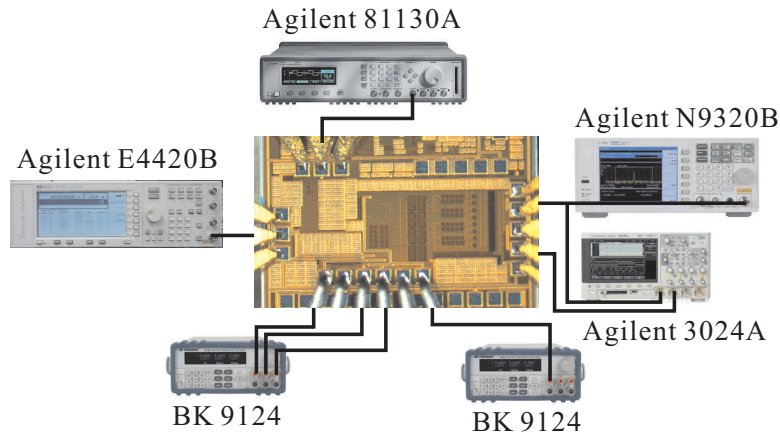


Figure 4.32: Measurement set-up.

The quadrature output signals were captured and are shown in Fig. 4.33. The measured stop-band attenuation and aliasing-band attenuation is around 40 dB, as shown in Fig. 4.34. This was measured by sweeping the input frequency from 100 MHz to 150 MHz. The simulated transfer function and measured transfer function are both plotted in this figure and normalized for comparison. It can be seen that, the measured frequency

response matches simulation results closely, up to about 10 MHz. After this, the measured transfer function starts to deviate from the simulation. There are two reasons for this. The loss of the gain and the clock crosstalk. The measured gain is about -9 dB rather than typical case, +14.4 dB or the worst case, +6.9 dB obtained in corner simulation. Given the input is -35 dBm and the limitation of the dynamic range of the spectrum analyzer, without noiseless pre-amplifier providing sufficient gain, it is hard to evaluate the characteristic of the filters, which are designed to provide maximum 80 dB attenuation for aliasing, and 60 dB attenuation for stop-band interferences. The reasons for the low gain is largely due to the improper on-chip biasing. The shifted operating points of the transistors break the impedance matching network. Therefore loss can be from the active balun providing input termination and the source follower output buffer that is connected to the spectrum analyzer whose input impedance is only 50 Ω . In addition, the degraded transconductor contributes the other part of the gain loss. The clock crosstalk also increases the difficulty of getting accurate profile of the filters. Since the limited silicon space, the improper shielding clock induces the coupled clock into the main signal path. The switching noise from the clock generator can eventually affect the V_{TH} thereby changing the bias condition of the transistors. As the design is a multi-sampling system, the pattern noises located at $f_s/4$, $f_s/2$... from gain and phase mismatch may degrade the filter performance. The large spikes were observed at the multiple of 12.5 MHz from measurements. The measured tuning range of 25 MHz to 250 MHz is shown in Fig. 4.35.

For a 100 MHz input signal, the simulated and measured stop band attenuation is 60 dB and 40 dB, respectively. The simulated and measured aliasing rejection is 70 dB and 42 dB, respectively. A simplified IIP3 measurement was done without using extrapolation approach. For a given sufficient small desired signal at 100.2 MHz with -40 dBm, the two tones, 100.4 MHz and 100.5 MHz with -30 dBm amplitude, was used to calculate IIP3. The post-layout simulation is illustrated in Fig. 4.36.

The 1 dB compression point is where the output of the amplifier is deviated from the ideal gain by 1 dB. The simulated 1 dB compression point is -27 dB, shown in Fig. 4.37.

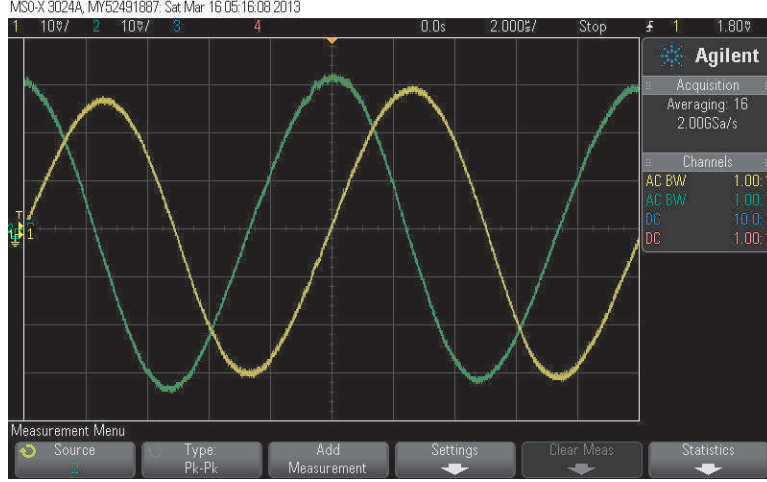


Figure 4.33: Measured quadrature output voltage of mixing sampler with input at 100.1 MHz.

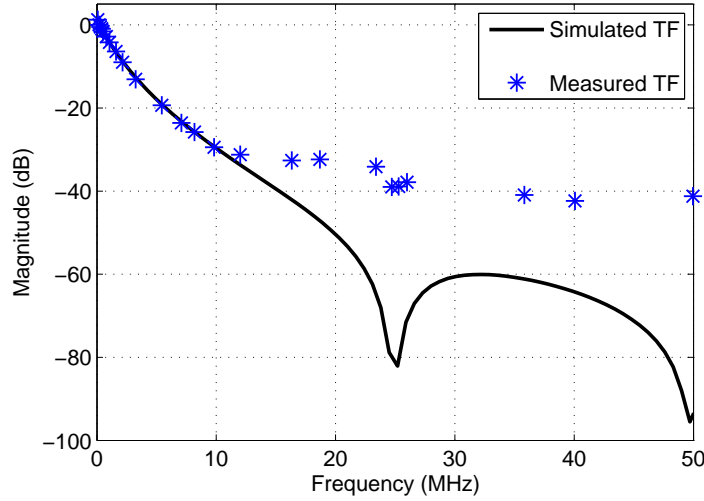


Figure 4.34: Measured and simulated normalized transfer function of mixing sampler.

From $P_{IIP3} = \frac{\Delta P}{2} + P_{fund}$ where ΔP is the difference between input and intermodulate signal and P_{fund} is the fundamental signal [2], IIP3 is obtained as -17 dBm. The image rejection was simulated by applying the input frequencies $100 \text{ MHz} \pm 0.2 \text{ MHz}$. The 90 degree phase shift was done in Matlab. By combining the I and Q path output, the quadrature down-conversion results in an image rejection of 43 dB. The post-layout simulation of IMR is shown in Fig. 4.38

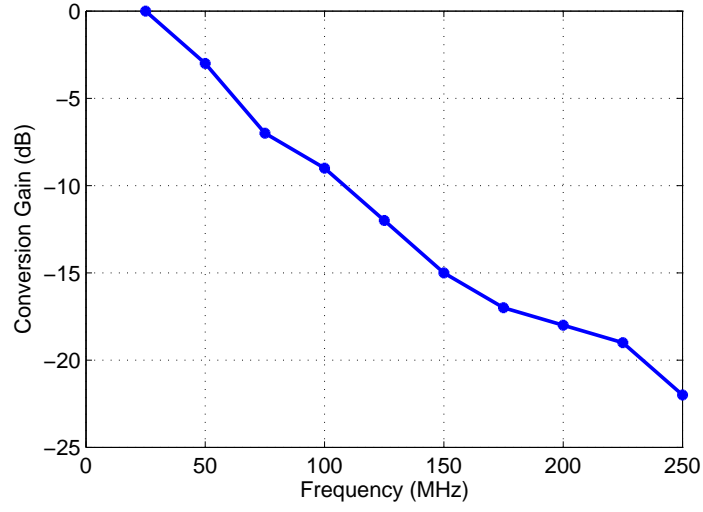


Figure 4.35: Measured tuning range of mixing sampler.

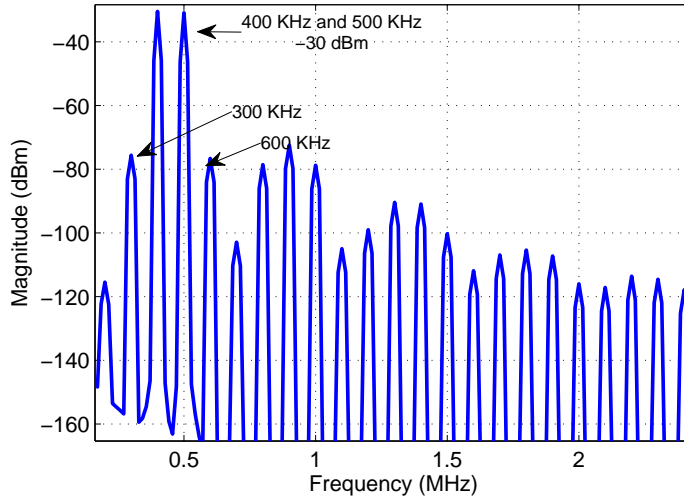


Figure 4.36: Post-layout simulated IIP3.

The chip consumes $180 \mu\text{W}$ from a 1.2 V power supply excluding active balun and output buffer. Table 4.2 compares the performance of the design presented in this chapter to that of other published works.

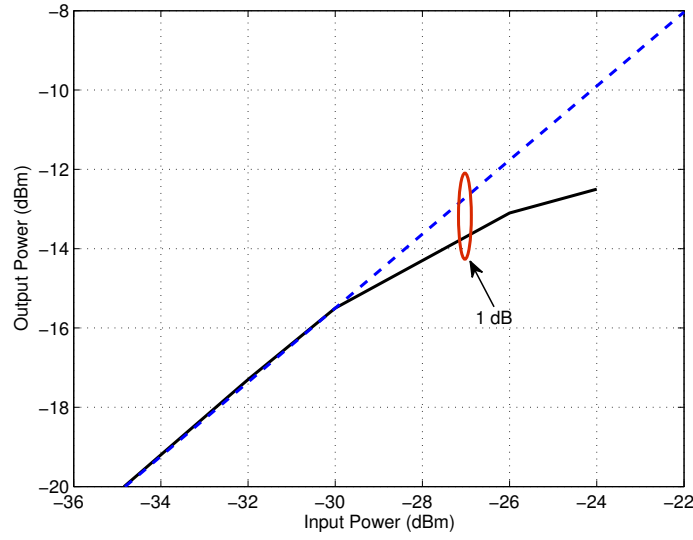


Figure 4.37: Simulated P_{1dB} .

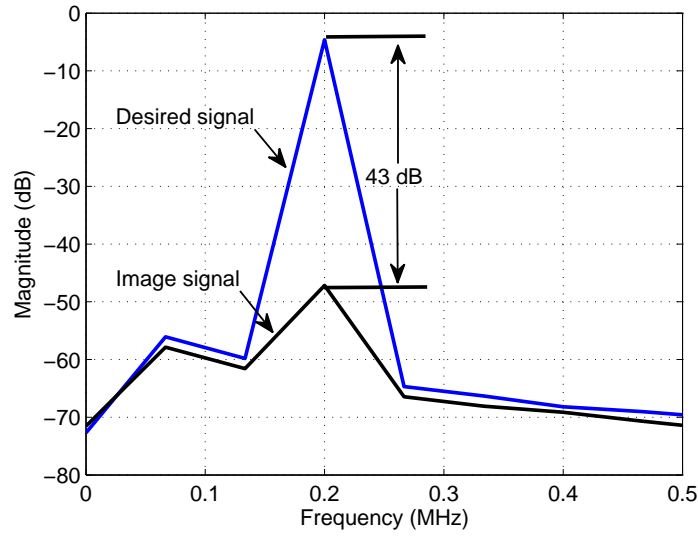


Figure 4.38: Post-layout simulated IMR.

4.5 Summary

The analysis and design of a low-power charge-domain quadrature down-conversion sampling mixer with embedded FIR, IIR, and 4-path bandpass filters suitable for band selection, frequency down conversion, and channel selection, are presented. Detailed inves-

Table 4.2: Performance Summary of Sampling Mixer

Parameters	This Work	[112]	[87]	[114]
Technology	0.13 μm	0.35 μm	90 nm	90 nm
IF Frequency	100 MHz	100 MHz	Base band	268 MHz
Output Rate f_{sout}	25 MHz	1.85 MHz	30 MHz	120 MHz
Signal Bandwidth	800 KHz	923 KHz	250 MHz	20 MHz
IIP3	-17 dBm (simulation)	-2 dBm	-22 dBm	0 dBm
P_{1dB}	-27 dBm (simulation)	NA	-32 dBm	NA
NF	19.5 dB (simulation)	NA	19 dB	21.8 dB
Aliasing Rejection	70 dB (simulation)			
	40 dB (measurement)	18 dB	NA	32.5 dB
Stop Band Att.	60 dB (simulation)			
	42 dB (measurement)	13 dB	42 dB	53 dB

tigations of the principles of periodic impulse sampling, periodic windowed sampling, and periodic N-path windowed sampling are presented. Their characteristics, with respect to the suppression of aliasing interferers and attenuation of unwanted channels, are compared. A detailed mathematical treatment of charge-domain windowed samplers with built-in sinc, FIR and IIR filters is provided. A quadrature charge-domain sampler with embedded FIR, IIR, and 4-path bandpass filters is proposed and designed. It is shown that the 4-path bandpass filter preceding the quadrature charge-domain sampling mixer provides sufficient attenuation of unwanted channels and nulls out aliasing interferers. The intrinsic sinc characteristics, FIR filtering from multi-phase integration, and IIR filtering (from the recursive operation of the history and rotating capacitors of the charge-domain sampler) provide further suppression of unwanted channels and aliasing interferers. The reused current configuration, of the 4-path bandpass filter and quadrature charge-domain sampling mixer, helps minimizing overall power consumption.

The design is applicable to zero-IF or low-IF receivers and suppresses aliasing signals, out-of-band blockers and IF image signals. Although the presented design implemented a first-order sinc and first-order FIR and IIR filters, high-order FIR filters can be implemented to provide better performance.

Chapter 5

A Cascaded Charge-domain Sampling Mixer with Embedded sinc³ FIR and N-Path Filters

In general, a sampling mixer along with an anti-aliasing filter demands large attenuations on aliasing signal and out-of-band signal for RF receivers operating on zero-IF or low-IF topology. In Chapter 4, a charge-domain sampler embedded with CT sinc, elementary DT sinc, first-order DT IIR low-pass and band-pass filters is introduced. An evolution of previous design is implemented in this chapter. A high-order sinc FIR and 4-path band-pass filters embedded charge-domain sampling mixer is presented. The chapter is organized as following: Section 5.1 investigates the advantages of the high-order FIR filter in terms of attenuation at the notches. Section 5.2 exams the proposed sampling circuit. Simulation results are shown in the Section 5.3. A summary is provided in Section 5.4..

5.1 Hight-Order FIR Filter

The FIR filter which is described in Chapter 4 is to provide elementary low-pass sinc filtering function since the coefficients of the filter are all one. The first sidelob of this type filter is merely 13 dB attenuation. In other words, out-of-band interferences that are within the first sidelobe, are lowered by 13 dB, which is not sufficient for most of the wireless applications. the null depth is heavily depending on the sampling frequency f_s . The sampling rate f_s must be large enough to get the desired attenuation around f_s . On the other hand, high order filter, which use low f_s , achieve same performance. [115], [83] and

[116] incorporated programmed coefficients of FIR filters to obtain advanced filter function in the sampler. However, the easiest approach is to utilize high-order sinc. For example, a second-order sinc in time domain is the convolution of two first-order sinc. A comparison of sinc, sinc^2 and sinc^3 is shown in Fig. 5.1.

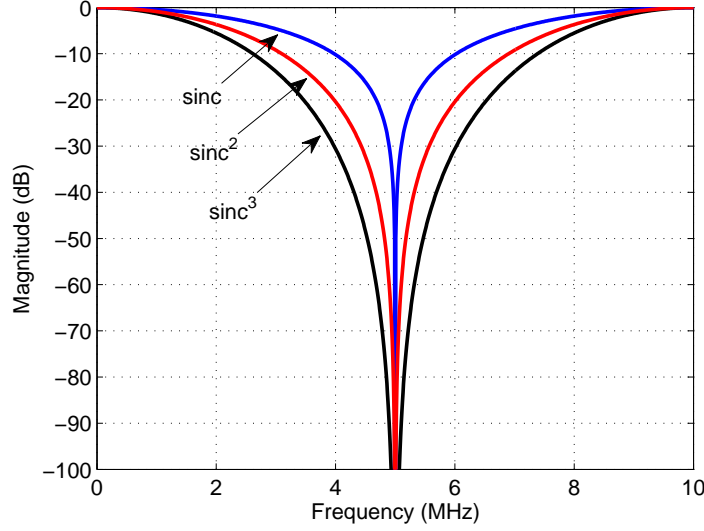


Figure 5.1: Frequency response of sinc, sinc^2 and sinc^3 . $f_{s,fir}=10$ MHz, decimation ratio is 2.

The corresponding s-domain transfer function is as follows:

$$H(s) = \left(\frac{1 - e^{-sT_s}}{sT_s} \right)^N. \quad (5.1)$$

where N is the order of the filter and T_s is the sampling frequency. It can be seen that the higher-order of the sinc, the wider of the notch. Therefore more attenuation is added on the aliasing signals around f_s .

5.2 Circuit Design and Analysis

The architecture of the charge-domain sampling mixer is shown in Fig. 5.2. Similar to the quadrature charge-domain sampler in Chapter 4, the input voltage is processed by the 4-path band-pass filter formed by M1 and a switched capacitor network that performs band selection. The band-selected output voltage obtained by diode-connected M2 is then fed to a pair of trans-conductors formed by M4 and M6 with $g_{m6} = 3g_{m3}$. The output currents of the trans-conductors are fed to a windowed charge-domain sampler (CDS) that functions as a low-pass filter to perform channel selection. Although a single-ended configuration is presented here, the proposed architecture is readily expendable to differential configurations to cancel out the even harmonic components and reject the common-mode signal ideally.

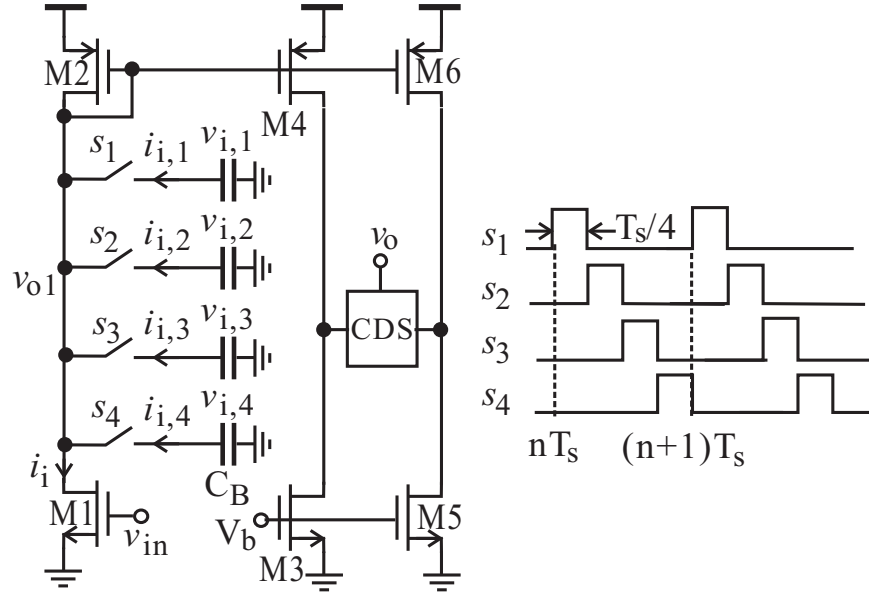


Figure 5.2: Advanced charge-domain sampler with embedded N-path band-pass filter. Circuit Parameters: $g_{m1} = 2\text{mS}$, $g_{m4} = 1.5\text{mS}$, $g_{m6} = 4.5\text{mS}$, $I_{b1} = 150\mu\text{A}$, $I_{b3} = 235\mu\text{A}$, $I_{b5} = 700\mu\text{A}$, $V_b = 335\text{mV}$.

5.2.1 Performance

Fig. 5.2 shows the 4-path bandpass filter, which is the single-ended version of Fig. 4.20. v_{in} is converted to i_i by M1. i_i is then routed to capacitors C_B by $s_k(t)$ and integrated onto C_B . The switched current $i_{i,k}(t) = i_i(t)s_k(t)$ produces voltage $v_{i,k}(t) = i_{i,k}(t) \otimes z_B(t)$ across the capacitors where $z_B(t)$ is the impulse response of the load and \otimes denotes convolution. $v_{i,k}(t)$ is then sampled by $s_k(t)$ to produce $v_o(t)$. For the sake of convenience, simulated frequency response of the single-ended 4-path filter is re-plotted in Fig. 5.3. It is seen that the absence of 4th and 8th harmonics and the sinc-envelope are due to the frequency-shaping. It should be mentioned again that the larger the number of paths, the less attenuation on interferences located at harmonic frequencies.

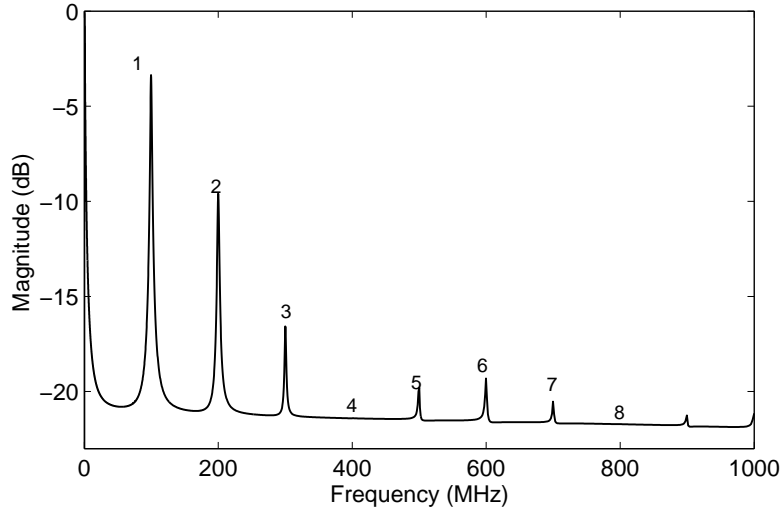


Figure 5.3: Response of 4-path band-pass filter in Fig. 5.2 (v_{o1} excluding M3-M6 and CDS).

Fig. 5.4 shows the simplified schematic of the proposed high-order windowed charge-domain sampler. The CDS implements three distinct filters : a continuous-time (CT) sinc low-pass, a discrete-time (DT) sinc³ low-pass, and a DT sinc low-pass. The CT low-pass filtering is obtained by current integration on sampling capacitors C_{S1} with its notches determined by the integration period. To widen the nulls so as to provide a better suppression of interferences in the neighborhood of the notches, a 3rd-order sinc with the coefficients(1

3 3 1) that are the results of the convolution of (1 1),(1 1) and (1 1) is implemented by weighted input currents. The simple coefficients limit the decimation ratio to 2 to avoid aliasing, which is achieved by time-interleaved operation Fig. 5.4(b). The second stage performs another decimation of 2. As a result, the sampling frequency is decreased by 4 times. Using a similar approach described in Chapter 4, we obtain the transfer function of the CT low-pass filter and DT filter

$$H(j\omega) = \frac{G_m T_i}{C_{S1}} \text{sinc}\left(\frac{\omega T_i}{2}\right) \sum_{k=0}^{N-1} h_{k1} z^{-k} \sum_{k=0}^{N-1} h_{k2} z^{-k} = H_{\text{sinc}} H_{FIR1} H_{FIR2} \quad (5.2)$$

where T_i is the pulse width of a_i or b_i , $i = 1, 2, 3$, h_{k1} and h_{k2} are (1 3 3 1) and (1 1) respectively.

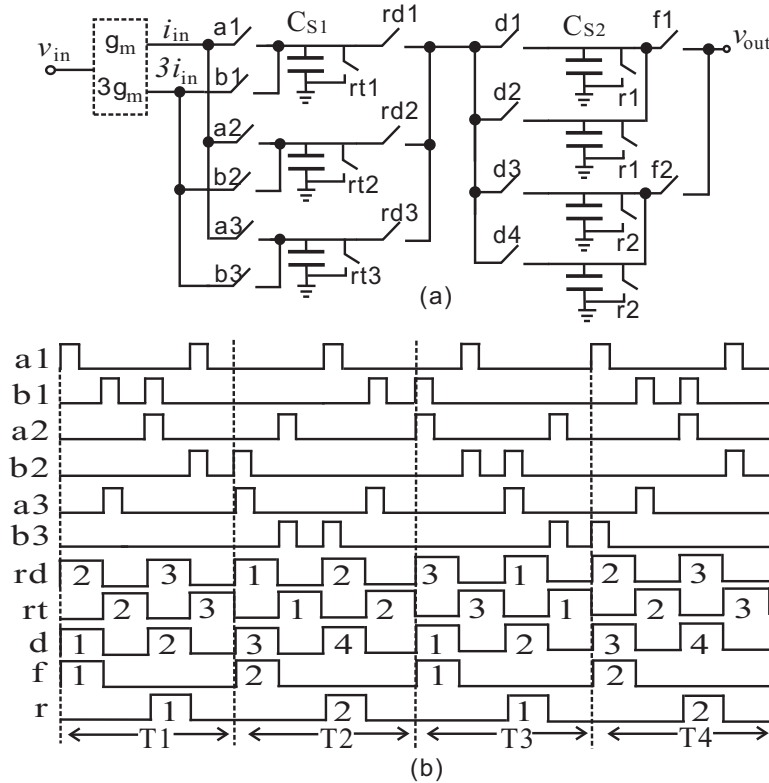


Figure 5.4: High-order windowed charge-domain sampler. Circuit Parameters: $g_m=1.5$ mS, $C_{S1}=10$ pF, $C_{S2}=1$ pF.

It is observed that the entire circuit provides the joint effect of band-pass and high-order sinc low-pass. Not only can a steep stop-band attenuation be obtained, the depth of notches will also be increased, yielding a better suppression of aliasing interferences and those in the vicinity of the notches.

5.3 Simulation Results

The proposed sampling mixer was designed in an IBM 130 nm 1.2V CMOS and analyzed using Spectre from Cadence. Fig. 5.5 shows the normalized frequency response of the sampling mixer with a zoom-in view of the first and second notches. It is seen that the suppression of aliasing interferences at the closest notch is 80 dB at 920 KHz -3 dB frequency band. Moreover, the wider aliasing band rejection at the second notch caused by sinc³ filter further improves the rejection close to 90 dB. The minimum stop-band attenuation is 57 dB. The gain is 9.2 dB compared to the calculated value of 12 dB. The loss of the gain is mainly due to the finite output impedance of the transconductors and the non-zero ON-resistance of the switches. Fig. 5.6 shows the time response of the sampler with the 100.2 MHz IF input.

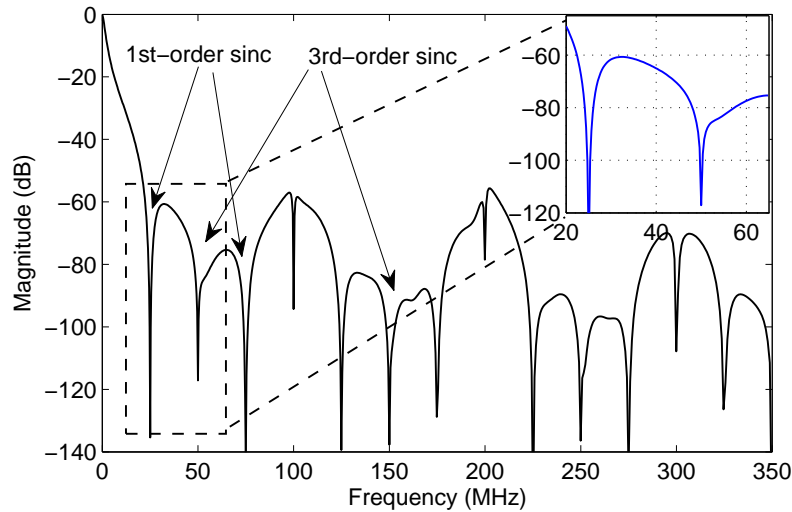


Figure 5.5: Simulated gain-normalized transfer function of proposed charge-domain windowed sampler with 100 MHz input.

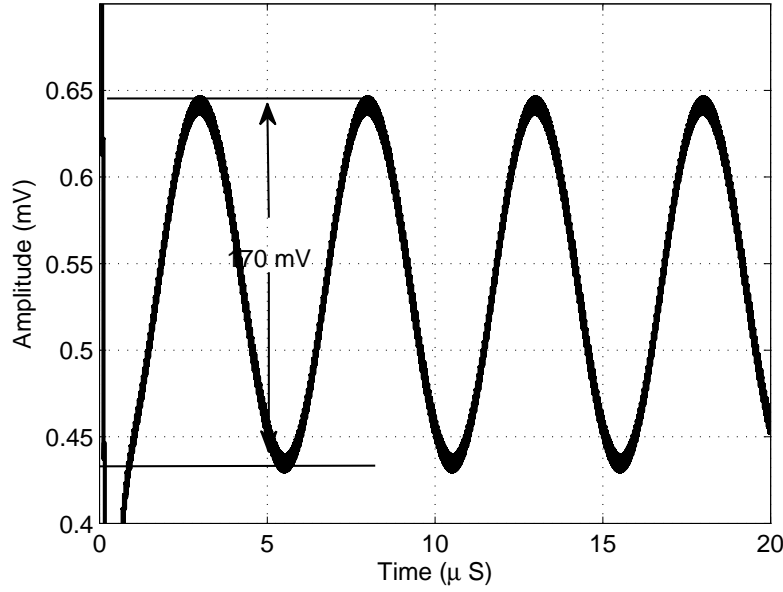


Figure 5.6: Simulated time response of the output signal with $V_{in} = 50\text{mV}$, $f_{in} = 100.2\text{ MHz}$, $V_{out} = 170\text{ mV}$, $f_{out} = 200\text{ KHz}$, $f_{s,out} = 25\text{ MHz}$.

Fig. 5.7 shows the layout of the circuit. The entire chip is $1 \times 2\text{ mm}^2$. The output of the sampling mixer is fed to a common-source buffer in order to drive an off-chip RF spectrum analyzer with a $50\ \Omega$ input impedance. Fig. 5.8 is the post simulation result. It can be observed that the amplitude of the output signal from post-layout simulation is smaller than that of the schematic simulation. It is mainly due to the voltage drop through the signal path in the layout.

The chip consumes 1.3 mW from a 1.2 V power supply excluding output buffer. Table 5.1 summarizes the performance of the proposed sampler and compares with that of some reported designs.

5.4 Summary

A charge-domain down-conversion sampling mixer with an embedded 4-path bandpass filter for band selection, a sinc^3 FIR and a 1^{st} -order sinc FIR with decimation of 4 for channel selection is presented. The sinc^3 low-pass is obtained via signal weighting and time-

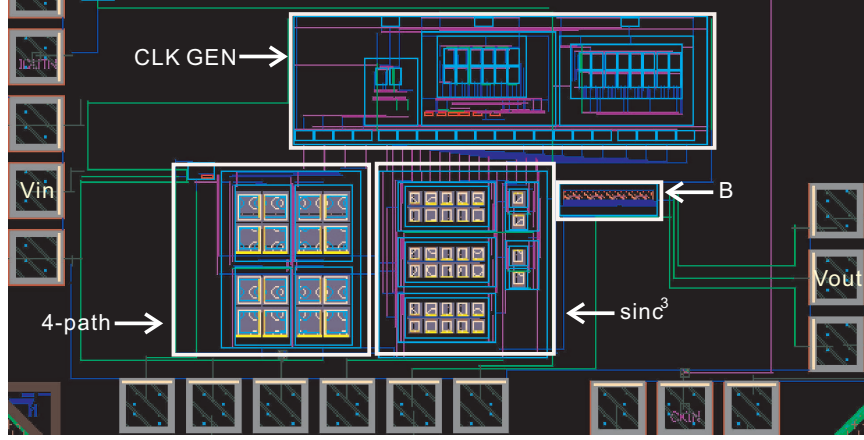


Figure 5.7: Simulated time response of the output signal with $V_{in}=50$ mV, $f_{in} = 100.2$ MHz, $V_{out} = 170$ mV, $f_{out} = 200$ KHz, $f_{s,out}= 25$ MHz.

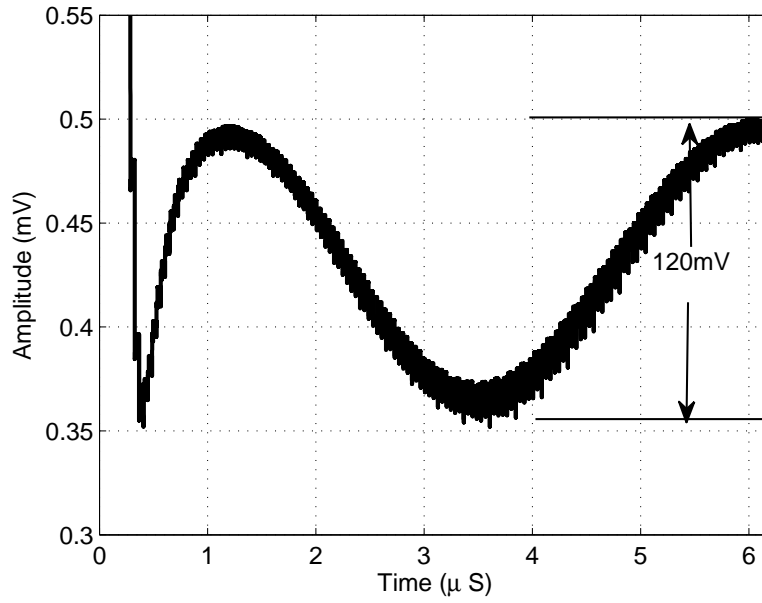


Figure 5.8: Post-simulated time response of the output signal with $V_{in}=40$ mV, $f_{in} = 100.2$ MHz, $V_{out} = 140$ mV, $f_{out} = 200$ KHz, $f_{s,out}= 25$ MHz.

interleaving operation. It is shown that the larger attenuation on the aliasing frequency and stop-band frequency is obtained by the combination of multiple filtering functions. The sampler performs decimation by 2 with wider notches and a steeper side-lobe attenuation. The total decimation by 4 is obtained by an another sinc filter following sinc^3 stage. The

Table 5.1: Performance Comparison

	This Work	[112]	[116]
Tech.	0.13 μm	0.35 μm	90 nm
Input Freq. (MHz)	100	50	200
Bandwidth (KHz)	920	12900	850
Output Sampling Freq. (MHz)	25	25	100
P _{1dB} (dBm)	-16	NA	NA
IIP3 (dBm)	-5	NA	-25
Aliasing Reject (dB)	-80	-55	-50
Stop Band Att. (dB)	-57	-35	NA

sampling mixer designed in an IBM 130 nm 1.2V CMOS with 100 MHz input exhibits 80 dB suppression of aliasing interferences and 57 dB stop band attenuation.

Chapter 6

Conclusions and Future Work

6.1 Conclusions

A new theoretical approach, clearly elaborating the phenomena of injection lock for harmonic oscillators, is presented. By applying it to analyze injection-lock process, the expression of lock range of the injection-locked harmonic oscillators is derived and validated in Cadence SpectreRF based on IBM 130 nm technology. In addition, the work that explores the intrinsic relation between large impedance variations of active inductors and the lock range of injection-locked active inductor oscillators is completed. The theoretical findings and the demonstrated example result in good understanding of improving the lock range of injection-locked oscillators in terms of design parameters [117, 118, 119].

The multiple multi-tone injection-locked oscillators are also explored. The in-depth investigation of injection-locked non-harmonic oscillators is carried out by utilizing an approach similar to Volterra series. The larger lock range of non-harmonic oscillators with a multi-tone injection can be expected as compared with that with a single-tone injection. For the case of multiple injections, the lock range is studied analytically. And also the proper phase assigned for each of the multiple injections is given. The theoretical analysis is validated using simulation [120, 121, 122, 123].

Two novel receivers for the application of software defined radio (SDR) are presented. The digital signal processing is performed in the analog form, resulting in reconfigurable RF

analog front-end. The receivers resolve the issue of using discrete components, e.g. SAW filter, which is commonly employed in the conventional radio frequency receivers to select the desired frequency band. The centre frequency of this filter in designs is controlled by on-chip clocks. In comparison with the traditional design, the needed anti-aliasing filter before analog-to-digital converter is integrated in the receiver and the cut-off frequency of the filter can also be tuned by changing the sampling clocks. As a result, the entire receiver becomes fully digital controlled. The quadrature sampler has the combination of CT sinc, DT sinc, DT IIR and 4-path bandpass filter. The other one has CT sinc, DT sinc³, DT sinc and 4-path bandpass filter included. The expecting functions of the fabricated chip have been validated on the wafer station in the lab [124, 125, 126]. Although the chips are targeting IF frequency, the conceptional design can be applied to the high frequency range.

6.2 Future Work

With regard to injection-locked oscillators, the extension could be further increasing the lock range of the relaxation oscillators through feedback signal, representing the frequency offset from the injection signal, to adjust the tail current of the relaxation oscillators. Since the sensitivity of the frequency of the relaxation oscillator is primarily determined by the charging and discharging current, e.g. $f = I_{tail}/2(CV_{ref})$, given the fixed capacitor value and threshold voltage of the comparator, changing current gives rise to frequency variation. The only issue is how to detect the injection signal to determine whether it is high-injection or low-injection as they give the same frequency difference. If this difficulty can be resolved, much wider lock range can be expected. In addition, implementing the exemplified circuits on chip and testing them in the lab could be the future work as well. Extensive simulations for the theoretical analysis have been carried out. However, the measurement results will provide more solid support for the findings. Also, the example is originally intended for low-power passive wireless communications. The relaxation oscillator is designed in subthreshold region, resulting in relatively low frequency, 13 MHz. Since the analysis is not limited to low frequency, a regular oscillator with RF band frequency can be developed to further prove the study in this thesis. The other important performance of injection-locked oscillators,

which is not discussed, is the lock time. For multiple injections, the impacts of the phases difference between the injection signals and the oscillating signals should be clearly observed from simulations. The multiple injections leads to faster lock time in comparison with the single injection can be expected. However, these are only surmise, which need to be further investigated.

There are also more possible extensions for the programmable receivers. Future design could be focusing on the linearity and noise performance of the transconductor, which dominants the linearity and noise for the entire design. Multiple gates, source degeneration and feedback configuration can be used to improve linearity. Furthermore, one more direction is to incorporate $\Sigma\Delta$ ADC, which offers exceptional performance for high resolution applications. For the 4-path, instead of bandpass filtering function, itself is a quadrature mixer. In other words, the output of DAC in the $\Sigma\Delta$ ADC can be applied to 4-path network to translate baseband signal back to RF. The whole loop includes bandpass filter, quadrature mixer for feedback signal, and charge domain sampling mixer with anti-aliasing and channel selection filter. The highly integrated and better linearity can be expected. In addition, the on-wafer measurement is not able to show the entire filtering functions due to some faulty layouts for some critical signal paths, e.g. biasing voltage, receiving signal paths and etc. Since the multiple signal paths are adopted, the matching for each of path becomes essential. The leakage clock signal is observed in the post-layout simulation because of the mismatches of signal paths and improper shielding. It is worth paying close attention on the layout techniques to get better performance.

Bibliography

- [1] A. Goldsmith, *Wireless communications*. Cambridge: Cambridge University Press, 2005.
- [2] B. Razavi, *RF microelectronics*. New York: Pearson education, 2012.
- [3] R. Miller, “Fractional-frequency generators utilizing regenerative modulation,” *Proc. IRE*, pp. 446–457, Jul. 1939.
- [4] R. Harrison, “Theory of regenerative frequency dividers using double-balanced mixers,” *Proc. IEEE Int’l Microwave Symp.*, pp. 459–462, 1989.
- [5] —, “A broad-band frequency divider using microwave varactors,” *IEEE Trans. Microwave Theory Tech.*, vol. 25, no. 12, pp. 1055–1059, Dec. 1977.
- [6] H. Rategh and T. H. Lee, “Superharmonic injection-locked frequency dividers,” *IEEE J. Solid-State Circuits*, vol. 34, no. 6, pp. 813–821, Jun. 1999.
- [7] H. Rategh, H. Samavati, and T. H. Lee, “A CMOS frequency synthesizer with an injection-locked frequency divider for a 5 GHz wireless LAN receiver,” *IEEE J. Solid-State Circuits*, vol. 35, no. 5, pp. 780–787, May. 2000.
- [8] A. Mazzanti, P. Uggetti, and F. Svelto, “Analysis and design of injection-locked LC dividers for quadrature generation,” *IEEE J. Solid-State Circuits*, vol. 39, no. 9, pp. 1425–1433, Sept. 2004.
- [9] C. Cao and Y. Ding, “A 50-GHz phase-locked loop in 0.13- μm CMOS,” *IEEE J. Solid-State Circuits*, vol. 42, no. 8, pp. 1649–1656, Aug. 2007.
- [10] H. Wu and L. Zhang, “A 16 to 18 GHz 0.18 μm EPI-CMOS divid-by-3 injection-locked frequency divider,” *IEEE Int’l Solid-State Circuits Conf., Digest Tech. Papers*, pp. 602–603, 2006.
- [11] C. Wang, C. Chen, M. Lei, M. Chuang, and H. Wang, “A 66-72 GHz divide-by-3 injection-locked frequency divider in 0.13 μm CMOS technology,” *Proc. IEEE Asian Solid-State Circuits Conference*, pp. 344–347, Nov. 2007.
- [12] C. L. S. Jang and W. Yeh, “A divide-by-3 injection locked frequency divider with single-ended input,” *IEEE Microwave and Wireless Lett.*, vol. 18, no. 2, pp. 142–144, Feb. 2008.

- [13] C. Zhou, L. Zhang, L. Zhang, Y. Wang, and Q. H. Z. Yu, "A 50% duty cycle wide-locking range divide-by-3 divider up to 6GHz," *Proc. IEEE Radio Frequency Integrated Circuits Symp.*, pp. 1–4, 2011.
- [14] I. T. Lee, C. H. Wang, and S. I. Liu, "Current-reused divide-by-3 injection-locked frequency divider in 65 nm cmos," *IET Electronics Letters*, vol. 47, no. 18, pp. 1029–1030, Sept. 2011.
- [15] I. Lee, C. Wang, J. Sha, Y. Juang, and S. Liu, "D-band divide-by-3 injection-locked frequency divider in 65 nm CMOS," *IET Electronics Letters*, vol. 48, no. 17, pp. 1041–1042, Aug. 2012.
- [16] Z. Huang, C. Wu, and B. Huang, "Design of 24-GHz 0.8-V 1.51-mW coupling current-mode injection-locked frequency divider with wide locking range," *IEEE Trans. Microwave Theory Tech.*, vol. 57, no. 8, pp. 1948–1958, Aug. 2009.
- [17] A. Mirzaei, M. Heidari, R. Bagheriand, S. Chehrai, and A. Abidi, "The quadrature LC oscillator: A complete portrait based on injection locking," *IEEE J. Solid-State Circuits*, vol. 42, no. 9, pp. 1916–1932, Sept. 2007.
- [18] J. Lee and H. Wang, "Study of subharmonically injection-locked PLLs," *IEEE J. Solid-State Circuits*, vol. 44, no. 5, pp. 1539–1553, May. 2009.
- [19] A. Musa, R. Murakami, T. Sato, W. Chaivipas, K. Okada, and A. Matsuzawa, "A low phase noise quadrature injection locked frequency synthesizer for mm-wave applications," *IEEE J. Solid-State Circuits*, vol. 46, no. 11, pp. 2635–2649, Nov. 2011.
- [20] J. Lu, N. Wang, and M. Chang, "A compact and low power 5 -10 GHz quadrature local oscillator for cognitive radio applications," *IEEE J. Solid-State Circuits*, vol. 47, no. 5, pp. 1131–1140, May 2012.
- [21] G. Mangraviti, B. Parvais, V. Vidojkovic, K. Vaesen, V. Szortyka, K. Khalaf, C. Soens, G. Vandersteen, and P. Wambacq, "A 52-66 GHz subharmonically injection-locked quadrature oscillator with 10 GHz locking range in 40nm LP CMOS," *Proc. IEEE Radio Frequency Integrated Circuits Symp. (RFIC)*, pp. 309–312, Jun. 2012.
- [22] T. Siriburanon, T. Ueno, K. Kimura, S. Kondo, D. Wei, K. Okada, and A. Matsuzawa, "A 60-GHz sub-sampling frequency synthesizer using sub-harmonic injection-locked quadrature oscillators," *Proc. IEEE Radio Frequency Integrated Circuits Symposium*, pp. 105–108, Jun. 2014.
- [23] F. Mahony, C. Yue, M. Horowitz, and S. Wong, "A 10-GHz global clock distribution using coupled standing-wave oscillators," *IEEE J. Solid-State Circuits*, vol. 38, no. 11, pp. 1813–1820, Nov. 2003.
- [24] L. Zhang, B. Ciftcioglu, M. Huang, and H. Wu, "Injection-locked clocking: A new GHz clock distribution scheme," pp. 785–788, Sept. 2006.

- [25] L. Z. and A. Carpenter, B. Ciftcioglu, A. Garg, M. Huang, and H. Wu, "Injection-locked clocking: A low-power clock distribution scheme for high-performance microprocessors," *IEEE Trans. Very Large Scale Integration (VLSI) Systems*, vol. 16, no. 9, pp. 1251–1256, Sept. 2008.
- [26] L. Zhang, B. Ciftcioglu, and H. Wu, "Active deskew in injection-locked clocking," in *proc. IEEE Custom Integrated Circuits Conf.*, Sept. 2008, pp. 567–570.
- [27] M. Hossain and A. Carusone, "CMOS oscillators for clock distribution and injection-locked deskew," *IEEE J. Solid-State Circuits*, vol. 44, no. 8, pp. 2138–2153, Aug. 2009.
- [28] Z. Bai, X. Zhou, R. Mason, and G. Allan, "Low phase noise clock distribution network using rotary traveling wave oscillators and built-in self-test phase tuning technique," *IEEE Trans. Circuits and Systems II: Express Briefs(early access)*, vol. PP, no. 99, pp. 1–1, Oct. 2014.
- [29] "EPC radio-frequency identity protocols class-1 generation-2 UHF RFID protocol for communications at 860 MHz - 960 MHz, version 1.0.9," *EPCglobal Inc.*, 2005.
- [30] C. Chan, K. Pun, K. Leung, J. Guo, L. Lincoln, and C. Choy, "A low-power continuously-calibrated clock recovery circuit for UHF RFID IC class-1 generation-2 transponders," *IEEE J. Solid-State Circuits*, vol. 45, no. 3, pp. 587–599, March 2010.
- [31] F. Marraccini, G. D. Vita, S. Pascoli, and G. Iannaccone, "Low-voltage nanopower clock generator for RFID applications," *Microelectronics J.*, vol. 39, pp. 1736–1739, 2008.
- [32] H. Lee and S. Mohammadi, "A subthreshold low phase noise cmos lc vco for ultra low power applications," *IEEE Microwave and Wireless Components Letters*, vol. 17, no. 11, pp. 796–798, Nov. 2007.
- [33] N. Tran, B. Lee, and J. Lee, "Development of long-range UHF-band RFID tag chip using Schottky diodes in standard CMOS technology," *Proc. IEEE Radio Frequency Integrated Circuits Symp.*, pp. 281–284, Sept. 2007.
- [34] B. Fan, Y. Dai, X. Zhang, and Y. Lu, "Low power clock recovery circuit for passive HF RFID tag," *Analog Integrated Circuits and Signal Processing*, vol. 59, pp. 207–214, 2009.
- [35] F. Kocer and M. Flynn, "A new transponder architecture with on-chip ADC for long-range telemetry applications," *IEEE J. Solid-State Circuits*, vol. 41, no. 5, pp. 1142–1148, May. 2006.
- [36] N. Soltani and F. Yuan, "Analysis and design of non-harmonic injection-locked phase-locked loops with applications in remote frequency calibration of passive wireless transponders," *IEEE Trans. Circuits and Systems-I: Redular papers*, vol. 57, no. 12, pp. 2381–2393, Sept. 2010.

- [37] Q. Ma, M. Haider, and Y. Massoud, "Robust power oscillator design for inductive-power link applications," in *Proc. IEEE Int'l Conf. Electronics, Circuits and Systems*, 2011, pp. 109–112.
- [38] A. Visweswaran, R. Staszewski, J. Long, and A. Akhnoukh, "Fine frequency tuning using injection-control in a 1.2v 65nm CMOS quadrature oscillator," in *Proc. IEEE Radio Frequency Integrated Circuits Symp.*, 2012, pp. 293–296.
- [39] M. Haider, S. Islam, and M. Mahfouz, "Power-efficient injection-locked oscillator for biomedical telemetry applications," *IET Electronics Letters*, vol. 46, no. 18, pp. 1252–1254, Sept. 2010.
- [40] H. Cho, J. Bae, and H. Yoo, "A 37.5 μ W body channel communication wake-up receiver with injection-locking ring oscillator for wireless body area network," *IEEE Trans. Circuits Syst. I*, vol. 60, no. 5, pp. 1200–1208, May 2013.
- [41] J. Bae, L. Yan, and H. Yoo, "A low energy injection-locked FSK transceiver with frequency-to-amplitude conversion for body sensor applications," *IEEE J. Solid-State Circuits*, vol. 46, no. 4, pp. 928–937, April 2011.
- [42] T. H. Lee, *The design of CMOS Radio-Frequency integrated circuits*. Cambridge: Cambridge University Press, 2004.
- [43] M. McDonald, "A 2.5 GHz BiCMOS image-reject front end," *IEEE Int'l Solid-State Circuits Conf., Digest Tech. Papers*, pp. 144–145, 1993.
- [44] A. Hairapetian, "An 81 MHz IF receiver in CMOS," *Solid-State Circuits, IEEE Journal of*, vol. 31, no. 12, pp. 1981–1986, Dec. 1996.
- [45] L. Longo, R. Halim, B. Horng, K. Hsu, and D. Shamlou, "A cellular analog front end with a 98 db IF receiver," *IEEE Int'l Solid-State Circuits Conf., Digest Tech. Papers*, pp. 36–37, 1994.
- [46] A. Mirzaei, H. Darabi, and D. Murphy, "A low-power process-scalable super-heterodyne receiver with integrated high-Q filters," *IEEE J. Solid-State Circuits*, vol. 46, no. 12, pp. 2920–2932, Dec. 2011.
- [47] A. Rofougaran, J. Chang, M. Rofougaran, and A. A. Abidi, "A 1 GHz CMOS RF front-end IC for a direct-conversion wireless receiver," *IEEE J. Solid-State Circuits*, vol. 31, no. 7, pp. 880–889, Jul. 1996.
- [48] B. Razavi, "A 5.2-GHz CMOS receiver with 62-dB image rejection," *IEEE J. Solid-State Circuits*, vol. 36, no. 5, pp. 810–815, May. 2001.
- [49] A. Garcia, C. Mishra, F. Bahmani, J. Silva-Martinez, and E. Sanchez-Sinencio, "An 11-band 3–10 GHz receiver in SiGe BiCMOS for multiband OFDM UWB communication," *IEEE J. Solid-State Circuits*, vol. 42, no. 4, pp. 935–948, Apr. 2007.

- [50] A. Abidi, "Rf CMOS comes of age," *IEEE J. Solid-State Circuits*, vol. 39, no. 4, pp. 549–561, Apr. 2004.
- [51] J. Mitola, "The software radio architecture," *IEEE Communications Mag.*, vol. 33, no. 5, pp. 26–38, May 1995.
- [52] A. Abidi, "The path to the software-defined radio receiver," *IEEE J. Solid-State Circuits*, vol. 42, no. 5, pp. 954 – 966, May 2007.
- [53] B. Razavi, "A study of injection locking and pulling in oscillators," *IEEE J. Solid-State Circuits*, vol. 39, no. 9, pp. 1415–1424, Sept. 2004.
- [54] S. Jang, C. Lin, C. Liu, and M. Juang, "An active-inductor injection locked frequency divider with variable division ratio," *IEEE Microwave and Wireless Lett.*, vol. 19, no. 1, pp. 39–41, Jan. 2009.
- [55] S. Jang, C. Liu, and C. Chuang, "A tail-injected divide-by-4 siGe HBT injection-locked frequency divider," *IEEE Microwave and Wireless Lett.*, vol. 19, no. 4, pp. 236–238, Apr. 2009.
- [56] C. Zhou, L. Zhang, L. Zhang, Y. Wang, and Q. H. Z. Yu, "Injection-locking-based power and speed optimization of CML dividers," *IEEE Trans. on Circuits and Systems II - Express Briefs.*, vol. 58, no. 9, pp. 565–569, Sept. 2011.
- [57] S. Jang, C. Chang, C. Cheng, C. Hsue, and C. Hsu, "A wide-locking range sige bicmos divide-by-3 injection locked oscillators," pp. 1–4, Apr. 2011.
- [58] J. Kang, X. Yu, and J. Zhou, "Optimization of injection locked frequency divider with tunable active inductor," *proc. IEEE Symp. Radio-Frequency Integration Technology (RFIT)*, pp. 74–76, Nov. 2012.
- [59] M. Tsai and H. Wang, "A 0.3-2.5 GHz ultra-wideband mixer using commercial 0.18 μ m CMOS technology," *IEEE Microwave and Wireless Component Lett.*, vol. 14, no. 11, pp. 522–524, Nov. 2004.
- [60] E. Sackinger and W. Fischer, "A 3-GHz 32-dB CMOS limiting amplifier for SONET OC-48 receivers," *IEEE J. Solid-State Circuits*, vol. 35, no. 12, pp. 1884–1888, Dec. 2000.
- [61] R. Adler, "A study of locking phenomena in oscillators," *Proc. of IEEE (reproduced from 1946 version)*.
- [62] L. N. S. Patnaik, and R. Harjani, "Understanding the transient behavior of injection locked LC oscillators," *Proc. IEEE Custom Integrated Circuits Conf.*, pp. 667–670, 2007.
- [63] P. Maffezzoni, D. Amore, S. Daneshgar, and M. Kennedy, "Analysis and design of injection locked frequency dividers by means of a phase domain macromodel," *IEEE Trans. Circuits and Systems-I: Regular papers*, vol. 57, no. 11, pp. 2956–2966, Nov. 2010.

- [64] I. Ali, A. Banerjee, A. Mukherjee, and B. Biswas, "Study of injection locking with amplitude perturbation and its effect on pulling of oscillator," *IEEE Trans. Circuits and Systems-I: Regular papers*, vol. 59, no. 1, pp. 137–147, Jan. 2012.
- [65] H. Chang, A. Borgioli, P. Yeh, and R. York, "Analysis of oscillators with external feedback loop for improved locking range and noise reduction," *IEEE J. Solid-State Circuits*, vol. 47, no. 8, pp. 1535–1543, Aug. 1999.
- [66] H. Chen, D. Chang, Y. Juang, and S. Lu, "A 30-GHz wideband low-power CMOS injection-locked frequency divider for 60-GHz wireless-LAN," *IEEE Microwave and Wireless Components Letters*, vol. 18, no. 2, pp. 145–147, Feb. 2008.
- [67] X. Yu, H. Cheema, R. Mahmoudi, A. van Roermund, and X. Yan, "A 3 mW 54.6 GHz divide-by-3 injection locked frequency divider with resistive harmonic enhancement," *IEEE Microwave and Wireless Components Letters*, vol. 19, no. 9, pp. 575–577, Sept. 2009.
- [68] H. Wu and A. Hajimiri, "A 19 GHz, 0.5mW, 0.35 μm CMOS frequency divider with shunt-peaking locking range enhancement," *IEEE Int'l Solid-State Circuits Conf., Digest Tech. Papers*, pp. 412–413, 2001.
- [69] J. Chien and L. Lu, "Analysis and design of wideband injection-locked ring oscillators with multiple-input injection," *IEEE J. Solid-State Circuits*, vol. 42, no. 9, pp. 1906–1915, Mar. 2007.
- [70] K. Yamamoto and M. Fujishima, "70 GHz CMOS harmonic injection-locked divider," 2006, pp. 2472–2481.
- [71] G. G. and P. Kinget, "Time-domain model for injection locking in nonharmonic oscillators," *IEEE Trans. Circuits Syst. I*, vol. 55, no. 6, pp. 1648–1658, July 2008.
- [72] H. Tong, S. Cheng, A. Karsilayan, and J. Martinez, "An injection-locked frequency divider with multiple highly nonlinear injection stages and large division ratios," *IEEE Trans. Circuits Syst. II*, vol. 54, no. 4, pp. 313–317, April 2007.
- [73] P. Deng and J. Kiang, "A 5-GHz CMOS frequency synthesizer with an injection-locked frequency divider and differential switched capacitors," *IEEE Trans. Circuits Syst. I*, vol. 56, no. 2, pp. 320–326, Feb. 2009.
- [74] A. Mirzaei, S. Chehraz, R. Bagheri, and A. Abidi, "Analysis of first-order anti-aliasing integration sampler," *IEEE Trans. on Circuits and Systems I*, vol. 55, no. 10, pp. 2994 – 3005, 2008.
- [75] J. Jin, X. Yu, J. Zhou, and T. Yan, "Gigahertz range injection locked frequency dividers with band-width enhancement and supply rejection," *IEE Electronics Letters*, vol. 44, no. 17, pp. 999–1000, Aug. 2008.
- [76] C. Bos and C. Verhoeven, "Frequency division using an injection-locked relaxation oscillator," in *Proc. IEEE Int'l Symp. Circuits Syst.*, vol. 5, 2002, pp. 517–580.

- [77] K. Zhu, S. Islam, J. Holleman, and S. Yuan, "A low-power dual-modulus injection-locked frequency divider for medical implants," in *Proc. IEEE Radio and Wireless Symp.*, 2011, pp. 414–417.
- [78] K. Zhu, S. Islam, M. Roksharifi, M. Hasan, and I. Mahbub, "A divide-by-3 0.4-1.4 GHz injection-locked frequency divider based on relaxation oscillator," *IEEE Microwave and Wireless Components Letters*, vol. 23, no. 7, pp. 368–370, July 2013.
- [79] J. Yuan, "A charge sampling mixer with embedded filter function for wireless applications," *Proc. ICMMT*, pp. 315–318, 2000.
- [80] R. Staszewski, K. Muhammad, D. Leipold, C. Hung, Y. Ho, J. Wallberg, C. Fernando, K. Maggio, R. Staszewski, T. Jung, J. Koh, S. John, I. Deng, V. Sarda, O. Moreira-Tamayo, V. Mayega, R. Katz, O. Friedman, O. Eliezer, E. De-Obaldia, and P. Balsara, "All-digital TX frequency synthesizer and discrete-time receiver for Bluetooth radio in 130 nm CMOS," *IEEE J. Solid-State Circuits*, vol. 39, no. 12, pp. 2278 – 2291, December 2004.
- [81] K. Muhammad, R. Staszewski, and D. Leipold, "Digital RF processing: toward low-cost reconfigurable radios," *IEEE Communication Mag.*, vol. 43, no. 8, pp. 105 – 113, August 2006.
- [82] S. Karvonen, T. Riley, and J. Kostamovaara, "Charge-domain FIR sampler with programmable filtering coefficients," *IEEE Trans. on Circuits and Systems II.*, vol. 53, no. 3, pp. 192 – 196, March 2006.
- [83] S. Karvonen, T. Riley, S. Kurtti, and J. Kostamovaara, "A quadrature charge-domain sampler with embedded FIR and IIR filtering functions," *IEEE J. Solid-State Circuits*, vol. 41, no. 2, pp. 507 – 515, Feb. 2006.
- [84] R. Bagheri, A. Mirzaei, S. Chehrazi, M. Heidari, M. Lee, M. Mikhemar, W. Tang, and A. Abidi, "An 800 MHz - 6 GHz software-defined wireless receiver in 90-nm CMOS," *IEEE J. Solid-State Circuits*, vol. 41, no. 12, pp. 2860–2876, Dec. 2006.
- [85] R. Bagheri, A. Mirzaei, M. Heidari, S. Chehrazi, M. Lee, M. Mikhemar, W. Tang, and A. Abidi, "Software-defined radio receivers: dream to reality," *IEEE Communications Mag.*, vol. 44, no. 8, pp. 111 – 118, August 2006.
- [86] A. Mirzaei, S. Chehrazi, R. Bagheri, and A. Abidi, "A second-order anti-aliasing pre-filter for a software-defined radio receiver," *IEEE Trans. on Circuits and Systems I.*, vol. 56, no. 7, pp. 1513 – 1524, 2009.
- [87] A. Yoshizawa and S. Iida, "A 250-MHz cutoff charge-domain baseband filter with improved stop-band attenuations," *IEEE Radio Frequency Integrated Circuits Symp., Dig. Papers*, pp. 491–494, 2009.

- [88] M. Darvishi, R. V. D. Zee, E. Klumperink, and B. Nauta, "A 0.3-to-1.2 GHz tunable 4th-order switched g_m -C bandpass filter with 55 dB ultimate rejection and out-of-band IIP3 of +29 dBm," *IEEE Int'l Solid-State Circuits Conf., Dig. Tech. Papers*, pp. 358–361, 2011.
- [89] A. Ghaffari, E. Klumperink, M. Soer, and B. Nauta, "Tunable high-Q N-path band-pass filters: modeling and verification," *IEEE J. Solid-State Circuits*, vol. 46, no. 5, pp. 998–1011, May 2011.
- [90] A. Mirzaei, H. Darabi, and D. Murph, "Architectural evolution of integrated M-phase high-Q bandpass filters," *IEEE Trans. on Circuits and Systems I.*, vol. 59, no. 1, pp. 52–65, Jan. 2012.
- [91] B. Razavi, *Design of Analog CMOS Integrated Circuits*. New York: McGraw-Hill, 2001.
- [92] F. Yuan, *CMOS active inductors and transformers - principle, implementation, and applications*. New York: Springer, 2008.
- [93] Y. Wu, X. Ding, M. Ismail, and H. Olsson, "RF bandpass filter design based on cmos active inductors," *IEEE Trans. Circuits and Systems-II: Express briefs*, vol. 50, no. 12, pp. 942–949, Dec. 2003.
- [94] T. Lin and A. Payne, "Design of a low-voltage, low-power, wide-tuning integrated oscillator," *Proc. IEEE Int'l Symp. Circuits and Systems*, vol. 5, pp. 629–632, 2000.
- [95] S. Hara, T. Tokumitsu, T. Tanaka, and M. Aikawa, "Lossless broad-band monolithic microwave active inductors," *IEEE Trans. Microwave theory and applications*, vol. 37, no. 12, pp. 1979–1984, Dec. 1989.
- [96] B. Razavi, "A study of phase noise in CMOS oscillators," *IEEE J. Solid-State Circuits*, vol. 31, no. 3, pp. 331–343, Mar. 1996.
- [97] S. Shekhar, M. Mansuri, F. O'Mahony, G. Balamurugan, J. Jaussi, J. Kennedy, D. J. Allstot, R. Mooney, and B. Casper, "Strong injection locking in low-Q LC oscillators: Modeling and application in a forwarded-clock I/O receiver," *IEEE Trans. Circuits and Systems-I: Regular papers*, vol. 56, no. 8, pp. 1818–1829, Aug. 2009.
- [98] S. Mitra, *Digital Signal Processing : A Computer-Based Approach*. Boston: McGraw-Hill, 2006.
- [99] M. Schetzen, *The Volterra and Wiener Theory of Nonlinear Systems*. New York: John Wiley and Sons, 1981.
- [100] P. Wampacq and W. Sansen, *Distortion Analysis of Analog Integrated Circuits*. Boston: Kluwer Academic Publishers, 1998.
- [101] F. Yuan and A. Opal, "Distortion analysis of periodically switched nonlinear circuits using time-varying volterra series," *IEEE Trans. on Circuits and Systems I - Fundamental Theory and Applications*, vol. 48, no. 6, pp. 726–738, Jun. 2001.

- [102] —, “An efficient transient analysis algorithm for mildly nonlinear circuits,” *IEEE Trans. on Computer-Aided Design of Integrated Circuits Syst.*, vol. 21, no. 6, pp. 662–673, Jun. 2002.
- [103] Q. Li and F. Yuan, “Time domain response and sensitivity of periodically switched nonlinear circuits,” *IEEE Trans. on Circuits and Systems I - Fundamental Theory and Applications*, vol. 50, no. 11, pp. 1436–1446, Nov. 2003.
- [104] R. Thomas and A. Rosa, *The Analysis and Design of Linear Circuits*. New York: John Wileys and Sons, 2001.
- [105] A. Foyt and T. Quist, “Phase-locked gaas cw microwave oscillators,” *IEEE Trans. on Electron Devices*, vol. 13, pp. 662–673, Jan. 1966.
- [106] H. Stover, “Theoretical explanation for the output spectra of unlocked driven oscillators,” *Proceedings of the IEEE*, vol. 54, pp. 310–311, Feb. 1966.
- [107] C. Stancampiano and S. Shapiro, “Power spectrum of an injection-locked josephson oscillator,” *IEEE Trans. on Magnetics*, vol. MAG-11, pp. 800–803, Mar. 1975.
- [108] C. Campbell, “Beat frequency spectra in a driven unlocked multimode saw cmob oscillator,” *Proc. Ultrasonic Symp.*, pp. 69–71, 1987.
- [109] K. Tsai, J. Wu, and S. Liu, “Frequency dividers with enhanced locking range,” *Proc. IEEE Radio Frequency Integrated Circuits Symp.*, pp. 661–664, 2008.
- [110] Y. Wan, X. Lai, and J. Roychowdhury, “Understanding injection locking in negative-resistance lc oscillators intuitively using nonlinear feedback analysis,” *Proc. IEEE Custom Integrated Circuits Conf.*, pp. 729–732, 2005.
- [111] L. Franks and I. Sandberg, “An alternative approach to the realization of network transfer functions: The N-path filters,” *Bell Systems Tech. J.*, vol. 39, pp. 1321–1350, Sept. 1960.
- [112] S. Karvonen, T. Riley, and J. Kostamovarra, “A CMOS quadrature charge-domain sampling circuit with 66-dB SFDR up to 100 MHz,” *IEEE Trans. on Circuits and Systems I*, vol. 52, no. 2, pp. 292 – 304, Feb. 2005.
- [113] S. Karvonen, T. Riley, and J. Kostamovaara, “A low noise quadrature subsampling mixer,” *Proc. IEEE Int’l Symp. on Circuits and Systems*, vol. 3, pp. 790–793, 2001.
- [114] M. Huang and T. Chiu, “A quadrature charge-domain filter with frequency downconversion for RF receivers,” *IEEE Trans. on Microwave Theory and Techniques*, vol. 58, no. 5, pp. 1323–1332, May. 2010.
- [115] D. Jakonis, K. Folkesson, J. Dabrowski, P. Eriksson, and C. Svensson, “A 2.4 GHz RF sampling receiver front-end in 0.18 μm CMOS,” *IEEE J. Solid-State Circuits*, vol. 40, no. 6, pp. 1265–1277, Jun. 2005.

- [116] N. Nguten, H. Jung, H. Min, J. Lee, G. Lee, S. Eo, and K. Yu, "A low power discrete-time receiver for triple-band FM/T-DMB/DAB system-on-chip," *Proc. IEEE CICC*, pp. 311–314, 2011.
- [117] Y. Zhou and F. Yuan, "Subthreshold CMOS active inductors with applications to low-power injection-locked oscillators for passive wireless microsystems," *Proc. IEEE Mid-West Symp. Circuits Syst*, pp. 885–888, Aug. 2010.
- [118] —, "A comparative study of lock range of injection-locked active inductor oscillators," *Proc. IEEE Mid-West Symp. Circuits Syst*, pp. 793–796, Aug. 2010.
- [119] —, "A study of lock range of injection-locked CMOS active-inductor oscillators using a linear control system approach," *IEEE Trans. on Circuits and Systems II - Express Briefs.*, vol. 58, no. 10, pp. 627–631, Oct. 2011.
- [120] —, "A frequency-domain study of lock range of harmonic oscillators with multiple injections," *Proc. IEEE North-East Workshop. Circuits Syst*, pp. 29–32, Apr. 2012.
- [121] F. Yuan and Y. Zhou, "A phasor-domain study of lock range of harmonic oscillators with multiple injections," *IEEE Trans. on Circuits and Systems II - Express Briefs.*, vol. 59, no. 8, pp. 466–470, Oct. 2012.
- [122] —, "Frequency-domain study of lock range of non-harmonic oscillators with multiple multi-tone injections," *IEEE Trans. on Circuits and Systems I - Regular Papers*, vol. 60, no. 6, pp. 1395–1406, Jun. 2013.
- [123] Y. Zhou and F. Yuan, "A study of injection-locked non-harmonic oscillators using Volterra series," *IET Circuits Devices and Systems(accepted for publication)*, 2014.
- [124] Y. Zhou, N. Filiol, and F. Yuan, "Low-power programmable charge-domain sampling mixer with embedded N-path bandpass filter for software-defined radio," *Proc. IEEE Int'l Symp. Circuits Syst*, pp. 1934–1937, May. 2013.
- [125] Y. Zhou and F. Yuan, "Cascaded charge-domain sampling mixer with embedded 3rd-order sinc FIR and 4-path filters for software-defined radio," *IET Electronics Letters*, pp. 216–218, Jan. 2014.
- [126] —, "Current reuse quadrature charge-domain sampling mixer with embedded FIR, IIR, and N-path filters," *IEEE Trans. on Circuits and Systems I - Regular Papers (under revision)*, 2014.